Spring 5-2018

# Surface Reaction and Diffusion Kinetics in Semiconducting Metal Oxide Film Gas Sensors

Aravind Reghu
*University of Maine*, aravindreghu14@gmail.com

# SURFACE REACTION AND DIFFUSION KINETICS IN SEMICONDUCTING METAL OXIDE FILM GAS SENSORS

By Aravind Reghu

B.Tech. University of Calicut, 2004

M.S. University of Maine, 2007

A DISSERTATION

Submitted in Partial Fulfillment of the

Requirements for the Degree of

Doctor of Philosophy

(Interdisciplinary in Sensor Science and Engineering)

The Graduate School

The University of Maine

May, 2018

Advisory Committee:

John Vetelino, Professor of Electrical Engineering, Co-Advisor

Brian Frederick, Professor of Chemistry, Co-Advisor

Robert Lad, Professor of Physics

David Frankel, Senior Research Scientist

Guido Faglia, Professor of Chemistry and Physics for Engineering and Materials, Universita Degli Studi Di Brescia

# SURFACE REACTION AND DIFFUSION KINETICS IN SEMICONDUCTING METAL OXIDE FILM GAS SENSORS

By Aravind Reghu

Dissertation Co-Advisors: Dr. John Vetelino and Dr. Brian Frederick

An Abstract of the Dissertation Presented
in Partial Fulfillment of the Requirements for the
Degree of Doctor of Philosophy
(Interdisciplinary in Sensor Science and Engineering)
May, 2018

Chemiresistive metal oxide gas sensors based on materials such as $SnO_2$, ZnO, and $TiO_2$, have been investigated extensively by many researchers for a wide range of applications. The band bending model, based on the surface chemistry of highly reactive ionosorbed species ($O_2^-$ or $O^-$) and the semiconducting material properties of $SnO_2$, $TiO_2$ and ZnO, adequately predicts the dependence of the change in sensor conductivity ($\Delta\sigma$) as a function of target gas pressure and temperature. However, the band bending model is not applicable to gas sensors based on reducible oxides such as $WO_3$, $MoO_3$ and $V_2O_5$, in which lattice oxygen reacts with adsorbed target gases creating oxygen vacancies which diffuse rapidly into the film bulk. In this study, a bulk conduction model which includes the kinetics of surface reaction and vacancy diffusion is developed in order to predict the response of reducible oxides, exposed to a target gas. In particular, $\Delta\sigma$, is predicted to be independent of film thickness, in contrast to the band bending model in which $\Delta\sigma$ is a function of film thickness. The time dependence of the sensor response was also analyzed and it shows that the response time increases with film thickness in the bulk conduction model. In contrast, the response time for the band bending model is independent of film thickness. In order to validate the theoretical predictions of the bulk conduction model, experimental data was obtained by exposing ppb levels of $NH_3$ gas to glancing angle deposited (GLAD) film with nanorod morphology and

planar Au/$WO_3$ film sensors at 450 °C. $\Delta\sigma$ as a function of $NH_3$ concentration was linear with a slope of unity for all the films and was also independent of volume to area ratio. Since the bulk conduction model predicts $\Delta\sigma$ to be linear with a slope of unity with target gas concentration in the low pressure regime and also predicts $\Delta\sigma$ to be independent of volume to area ratio, there is good agreement between the model and the experimental sensor response. This clearly indicates that the sensor response is due to bulk conduction mechanism. In summary it has been shown that theoretical model for bulk conduction mechanism is most appropriate to describe the response of $WO_3$ film gas sensors as opposed to the band bending model.

## ACKNOWLEDGEMENTS

First, I would like to thank my Ph.D co-advisor, Dr. John Vetelino, for the continuous support of my Ph.D study, and also for his encouragement and motivation. His advice was of immense help during the course of my research and also during the writing of this thesis. I also wish to thank my other Ph.D co-advisor Dr. Brian Frederick, for his incredible mentorship and untiring support. His guidance combined with his incredible knowledge of my research subject was priceless for the successful completion of my research and also for my growth as a research scientist. I would also like to thank the rest of my advisory committee: Dr. Robert Lad, Dr. David Frankel and Dr. Guido Faglia for their help and guidance. I also wish to acknowledge W.M. Keck foundation for providing the funding for this project. I wish to acknowledge the help of Dr. Paul Mayewski, Dr. George Bernhardt, Dr. Derya Deniz, Mike Call and Rahim Stennett during the course of this project.

I wish to acknowledge the support of my close family: my mother, Geetha, my father, Reghu, my son, Anay, my brother, Gautham, my parent in laws Ramanujam and Girija and my extended family and friends.

Above all, I want to thank my wife, Anusha, for her patience, encouragement, and unwavering love and support. These were the bedrock upon which the past several years of my personal and academic life were built.

## TABLE OF CONTENTS

## LIST OF TABLES

## LIST OF FIGURES

# 1. INTRODUCTION

## 1.1 Background

In recent years, concerns for a clean and healthy environment in locations ranging from homes to the global level have motivated researchers to develop a wide range of gas sensors.[1] In general the need for gas detection necessary to address these concerns can be divided into the following five major categories[1-3],

- Exhaust gases from internal combustion engines such as motor vehicles.
- Harmful gases emitted during industrial processes.
- Gases in human breath for the detection and monitoring of diseases.
- Gases in the home and workplace to ensure indoor air quality.
- Greenhouse gases to ensure environmental air quality.

Depending upon the application, many types of gas sensors are commercially available with the more common ones being catalytic detectors, optical detectors and chemiresistive gas sensors.[4] Catalytic detectors operate on the principle that as the gas oxidizes, it releases heat and the associated temperature change is converted to an electrical signal to identify the target gas.[5] There are two major types of gas analyzers that use optical techniques. The first one uses spectrophotometric detection, which involves a change in color as a target gas reacts with a reagent. The second type involves optical absorption detection where light is incident on a gas selective layer and the reflected or transmitted light is analyzed by a spectrometer to determine the presence and/or concentration of the target gas.[6] The chemiresistive gas sensor typically consists of a film deposited over an electrically insulating substrate in which the change in the electrical properties (resistivity or conductivity) of the film is monitored as the target gas

interacts with the film.[7-8] The sensing film layer can be made from materials like semiconducting metal oxides (SMO), conducting polymers (CP), carbon nanotubes (CNT) and metals.

### 1.1.1 Chemiresistive Gas Sensors

Of all the gas sensors, the chemiresistive gas sensor with an SMO film has been the most widely studied due to advantages such as ease of fabrication, simplicity of design, portability and low cost of production.[7] SMO films can be fabricated using a number of methods such as physical vapor deposition (thermal evaporation, RF magnetron sputtering etc), chemical vapor deposition and sol-gel techniques. The ability of SMO films to respond to multiple gas exposures, their reproducibility, high sensitivity to a wide range of gases and the ease of integrating them into a portable, cheap sensor system makes them an attractive target selective film in gas sensing applications.[9] The first work in semiconducting gas sensing was done by Bardeen in 1947, when he noticed a change in electrical conductivity in semiconductors such as silicon due to surface states created by adsorbed foreign atoms.[10] The first major work on SMO films for gas sensing was done by Seiyama et.al[8] in 1963 where they developed a ZnO thin film detector for sensing gases like toluene, carbon dioxide, ethyl alcohol, propane and benzene. Since the work of Seiyama et al, several others have done work on different SMO films for detecting a wide range of gases.[11-15] One of the most significant work was done by Taguchi in 1968 where he developed an $SnO_2$ film based methane gas sensor.[16] In 1969, Figaro Engineering Inc commercialized the gas sensor developed by Taguchi and subsequently spawned research into a wide range of SMO films for their use as sensing layers for detecting various gases.[9, 17-18]

In concert with SMO film based chemiresistive sensors, conduction polymer (CP) and carbon nanotube (CNT) based chemiresistive sensors have been studied for gas sensing applications since the 1980's.[19-25] CP based chemiresistive sensors offer advantages like ease of

fabrication, high sensitivity, fast response times and room temperature operation whereas CNT based chemiresistive sensors offer advantages such as being small and light weight and are resistant to temperature changes. The disadvantages of CP based sensors are their long term instability and lack of selectivity[1] while the major disadvantage of CNT based sensors is the expense involved in fabricating the sensor.

Since SMO film based chemiresistive gas sensors offer a cheap, effective and long term solution to gas sensing applications compared to CP and CNT based sensors, the focus of this thesis is on SMO film based chemiresistive gas sensors and particularly on the transduction mechanisms which describe how the target gas reacts with the SMO film and changes the film electrical properties.

### 1.2 Semiconducting Metal Oxide (SMO) Film Structure

Although SMO films can in general be amorphous or polycrystalline, it has been observed that polycrystalline film SMO sensors have better sensitivity to gases compared to amorphous films.[9, 14] SMO films deposited in vacuum systems such as the RF magnetron sputtering system at room temperature tend to be amorphous. To make polycrystalline films, film deposition needs to be done at an elevated temperature or the amorphous film formed at a lower temperature needs to be annealed at a higher temperature for a certain period of time to make it polycrystalline. The amorphous to polycrystalline transition, which is irreversible, depends on the SMO material and the annealing temperature. In the polycrystalline state, the films consists of crystallites separated by a grain boundary resulting in the surface of these films being highly discontinuous with metal cations and oxygen anions present at the surface.

Post deposition structural analysis of polycrystalline SMO films indicate that they are not stoichiometric and a certain amount of oxygen vacancies exists in the film. For example tungsten trioxide is not exactly $WO_3$, but $WO_{3-x}$ where 3-x is slightly less than 3.[26] Since there are weakly bound electrons associated with metal ions in the vicinity of the oxygen vacancies, many of these electrons become free and hence most SMO films are n-type semiconductors.

### 1.2.1 Deposited SMO Film Interaction with Oxygen ($O_2$) Gas

Since SMO film sensors are typically operated in a 20% $O_2$ environment, it is important to describe the SMO film interaction with $O_2$. From electron spin resonance (ESR) studies,[27-30] it has been shown that $O_2$ adsorbs on the SMO film and forms the superoxide, $O_2^-$, at room temperature by accepting free electrons near the film surface as described by the following equation,

$$O_2 + e^- \rightleftharpoons O_2^- . \quad (1.1)$$

Evidence for the stability and reactivity of $O_2^-$ on a variety of oxide surfaces is well understood from ESR studies, extensively reviewed by Che and Tench.[27-28] The $O_2^-$ species are stable at temperatures up to 200 – 300 °C on oxides with lower cation charge such as $SnO_2$ and $TiO_2$ but only up to about 150 °C on oxides with higher cation charge such as $MoO_3$ and $WO_3$.[30] As temperature is increased (above 150 °C for $WO_3$ and above 300 °C for $SnO_2$), ESR studies on metal oxides reported by Shvets et.al[29-30] have shown that $O_2^-$ dissociates to form $O^-$ by taking free electrons near the film surface as described by the following equation,

$$O_2^- + e^- \rightleftharpoons 2O^- . \quad (1.2)$$

Therefore, depending on the type of SMO material used and the sensor operating temperature, it is possible that both $O^- \; and \; O_2^-$ surface species may coexist on the SMO film surface.

The $O^-$ species may or may not desorb from the film surface. In particular, for $SnO_2$, $O^-$ is stable to temperatures of 300 – 450 °C and then desorbs into the ambient as gaseous oxygen.[31] In contrast, for $WO_3$, $V_2O_5$ and $MoO_3$, at 350 °C, ionosorbed $O^-$ migrates into the film[32] forming metal oxygen bonds by accepting weakly bound electrons (to form a stable outer shell) associated with metal ions (due to oxygen vacancies). This oxygen species is called lattice oxygen ($O^{2-}$) as described by the following equation,

$$O^- + e^- \rightleftharpoons O^{2-}. \quad (1.3)$$

### 1.2.2 Deposited SMO Film Interaction with Target Gas

The gas interaction with the SMO film surface depends on the type of SMO film along with the film operating temperature. The ionosorbed oxygen species on SMO films like $SnO_2$, with lower cationic charge is stable up to 450 °C while in SMO materials like $WO_3$ which has a higher cationic charge, the ionosorbed oxygen species are stable up to 350 °C. It is important to note that the operating temperature of the sensor is determined by observing the temperature for which the sensitivity to the target gas is the highest. For example, when a $SnO_2$ film sensor is exposed to a target gas operating at a temperature of 450 °C, the interaction of the target gas would most likely be with the ionosorbed $O^-$ species while at the same operating temperature, the target gas would be interacting with $O^{2-}$ species in SMO films like $WO_3$. Thus when a target gas interacts with the SMO film, it can either react with the surface ionosorbed $O^- \; and \; O_2^-$ species (depends on the sensor operating temperature and the type of SMO film) or the lattice $O^{2-}$ species resulting in two types of transduction mechanisms. The transduction mechanism involving interaction with surface adsorbed $O^- \; and \; O_2^-$ species is called **band bending**

**mechanism** while interaction with lattice $O^{2-}$ species is called **bulk vacancy conduction mechanism.**

### 1.2.2.1 Band Bending Mechanism

As mentioned earlier, the band bending mechanism depends on the temperature of operation and the SMO film material. After deposition, the SMO film is removed from the vacuum system and then exposed to $O_2$. If the SMO film is heated, the ionosorbed $O^- \; and \; O_2^-$ surface species are formed (given by equations (1.1) and (1.2)) by trapping weakly bound electrons from the surface. This results in a region depleted of mobile carriers (depletion region). A potential barrier is then formed in the depletion region due to the accumulated negative charge on the film surface and the ionized donors in the depletion region which gave up their electrons.

Upon application of a dc voltage the free electrons in the bulk of the SMO film need to overcome this barrier potential to move from one crystallite to another. When the film is then exposed to a target gas, the gas-film reaction depends on whether the target gas is an oxidizing or reducing agent. The following equations show a reduction reaction where the reducing target gas, $A$, reacts with the ionosorbed species to form reaction product, $B$, along with free electrons,

$$A + O^- \rightarrow B + e^- . \tag{1.4}$$

and

$$A + O_2^- \rightarrow B + e^- . \tag{1.5}$$

In this case, some ionosorbed $O^- \; and \; O_2^-$ species are removed and there is an increase in the concentration of free electrons. This results in reducing the barrier potential and increasing the

film conductivity. The target-gas film reaction may also be an oxidation reaction where the oxidizing target gas, $RO_2$, dissociates to form the reaction product, $RO$, and ionosorbed, $O^-$, species by taking free electrons from the film surface[33-34] as shown below,

$$RO_2 + e^- \rightarrow RO + O^- . \quad (1.6)$$

In this case, free electrons near the surface are removed to form ionosorbed $O^-$ species. This results in an increase in the barrier potential and a decrease in electrical conductivity. In SMO films such as ZnO, $SnO_2$ and $TiO_2$, the transduction mechanism is **band bending**.

#### 1.2.2.2 Bulk Vacancy Conduction Mechanism

In the bulk vacancy conduction mechanism both reduction and oxidation reactions can occur as the target gas interacts directly with the lattice $O^{2-}$ species which are located at the surface and in the film bulk. In the equation given below, a reducing target gas, $A$, reacts with lattice $O^{2-}$ to form the reaction product, $B$, resulting in the creation of a lattice oxygen vacancy, $V_o$, and free electrons,

$$A + O^{2-} \rightarrow B + V_o + 2e^- . \quad (1.7)$$

If the target gas-film reaction, is as shown in equation (1.7), oxygen vacancies are formed along with free electrons in the film which in turn results in an increase in SMO film electrical conductivity. In the equation below, an oxidizing gas, $RO_2$, dissociates to form reaction product, $RO$, along with the creation of lattice $O^{2-}$ species,

$$RO_2 + V_o + 2e^- \rightarrow RO + O^{2-} . \quad (1.8)$$

In an oxidation reaction, the oxygen vacancy, $V_o$, is annihilated and electrons are consumed in the formation of metal oxygen lattice bonds. This results in a decrease in the number of free

electrons in the film bulk and therefore a decrease in electrical conductivity. This **bulk vacancy conduction mechanism** is observed in SMO films such as $WO_3$, $MoO_3$ and $V_2O_5$.

### 1.3 Sensor Response Characteristics Based on Transduction Mechanisms

It is obvious that the sensor response (sensitivity and response time) of an SMO film sensor has a dependence on the type of transduction mechanism. Response is taken as the magnitude of the change in steady state conductivity ($\Delta\sigma$) of the sensor when exposed to the target gas and air. The magnitude of this change depends on the rate at which gas reacts with surface ionosorbed oxygen species (band bending mechanism) or surface lattice species ($O^{2-}$ $and$ $V_o$ for bulk vacancy conduction mechanism) to produce free electrons. However, the response time ($\tau$), which is defined as the time taken to reach 90% of $\Delta\sigma$, can be different for both these cases. In the band bending mechanism, the response time is the time taken for the target gases to react with the ionosorbed oxygen species on the film surface but this could be different for the bulk vacancy conduction case. In the latter case the response time depends on the rate at which target gas reacts with surface lattice species ($O^{2-}$ $and$ $V_o$ on the surface) and the rate at which the surface oxygen vacancies diffuse into and equilibrate throughout the bulk of the film. Consider a target gas reaction on surface $O^{2-}$species to get surface oxygen vacancies given by equation (1.7). In this case, because of the creation of surface oxygen vacancies, there will be a vacancy concentration gradient in the film bulk and it will take a certain amount of time for the vacancies to diffuse into and equilibrate in the film bulk. Thus, if one observes the total sensor response to this target gas, the response time will include both the time taken for the target gas to react with the surface $O^{2-}$ to create surface vacancies and also the time taken for these vacancies to diffuse and equilibrate in the bulk. If the target gas reaction with the lattice species on the SMO film surface is slow compared to the rate at which vacancies are diffusing into the bulk of

the film, the fast diffusion of vacancies ensures that the vacancies are quickly and uniformly spatially distributed throughout the film. Thus there is no appreciable vacancy concentration gradient in the film bulk. In this situation, the overall sensor response time is determined primarily by the time taken for the target gas to react with the surface $O^{2-}$ species to form enough vacancies to equilibrate the bulk of the film and the sensor response is considered as **surface reaction limited**. Now referring again to equation (1.7), if the surface reaction is very fast compared to the bulk vacancy diffusion time, then a constant flux of lattice vacancies are present at the surface of the film. In this case a concentration gradient exists in the bulk of the film and the response time of the sensor to the target gas is determined primarily by the time taken for the vacancies to diffuse into and equilibrate in the bulk of the film. Thus, this type of sensor response is considered to be **bulk vacancy diffusion limited**.

In addition to surface reaction rates which determine the rate at which vacancies are formed at the surface of the film due to target gas interaction and the bulk vacancy diffusion coefficient which determines the rate at which vacancies diffuse in the bulk of the film, other critical parameters on which the SMO film sensor response depends are surface area to volume ratio, film thickness, surface barrier potential and width, concentration of surface oxygen vacancies and surface $O^{-}\ and\ O_2^{-}$ species and crystallite size. Parameters like surface barrier potential and width depend on the concentration of surface $O^{-}\ and\ O_2^{-}$ species which become important if the sensor response is due to band bending mechanism while other parameters like diffusion coefficients and film thickness become prominent when the sensor response is due to bulk vacancy conduction mechanism. In spite of the commercial availability of SMO film based chemiresistive gas sensors, a complete understanding of the gas-film interaction is not well known since the effect of these aforementioned parameters on the sensor response has not been

properly understood. Compared to bulk conduction mechanism, the transduction mechanism due to band bending has been studied extensively. Effects of different parameters like crystallite size[35], film surface area[36-37], and target gas concentration[38] on the sensor response, have been studied through experimental work and kinetic modeling.

### 1.4 Existing Models on Transduction Mechanism in SMO Sensors

#### 1.4.1 Band Bending Mechanism

Relative to band bending models, in 1953, Weisz developed a detailed model involving sorption of gas molecules on a semiconductor surface.[39] An expression for the barrier potential as a function of the space charge layer width can be derived from the Weisz model. Weisz also derived an expression for the total number of chemisorbed molecules as function of donor density and barrier potential.[39] In 1996, Kim et.al have experimentally determined the variation in the barrier potential and conductance due to oxygen adsorption on the surface and carbon monoxide (CO) reaction to these adsorbed oxygen species by using the I-V characteristics of ZnO–ZnO single crystal contact.[40] From the inflection of I-V curves, he was able to calculate the change in barrier potential when the contact was exposed to CO. Applying a forward bias voltage ($V_b$) across the contact, the electrons move from the negatively biased metal oxide to the positively biased metal oxide through the contact zone and the expression for current in terms of bias voltage $V_b$ was derived. Both the aforementioned models were developed for single crystals. Li et al,[37] in 1999, studied grain size effects in $SnO_2$ based sensors (powder) using a grain boundary contact model. They determined that sensors with smaller grain size provided higher surface area and showed higher sensitivity to the target gas. In 2001, Weimar et.al[31] derived a model to explain the conduction model in $SnO_2$ polycrystalline film sensors based on the band bending transduction mechanism. In this work, the ratio of conductance values after gas

exposure to the value in air as a function of target gas concentration was presented. In 2005, Ahlers et.al[41] applied a simplified version of the Weimar model to experimental data for detection of reducing gases on thin $SnO_2$ films. The model was used to extract parameters, such as film thickness, depletion layer widths, and activation energies, to fit the sensitivity as a function of gas concentration, and temperature. More recently in 2015,Vuong et.al[42] studied the adsorption-desorption kinetics of oxidizing gases in $WO_3$ nanowire sensor and observed that the detection limit and selectivity of the sensor to the target gas depends on the reaction kinetics at the surface. In 2016, Vuong et.al[43] modeled the surface reaction mechanism of reducing gases on surface ionosorbed $O^-$ species in $WO_3$ nanowire sensors of different diameters under the assumption that $O^-$ species may be present on the surface at 300 °C. They reported that the sensor response to reducing target gases depends on the surface reaction kinetics of the target gas with ionosorbed $O^-$ species. They also reported that the maximum sensor response and minimum response time to target gas was when the diameter of the nanowire sensor was equal to the thickness of the depletion region (under total depletion condition).

### 1.4.2 Bulk Vacancy Conduction Mechanism

In the bulk vacancy conduction mechanism, the sensor response time could be **bulk vacancy diffusion limited** or **surface reaction limited**. Several attempts have been made to model bulk diffusion in polycrystalline films. In 1951, Fischer was the first to make a phenomenological analysis of diffusion in polycrystalline medium. This was followed in 1954 by Whipple who presented a mathematical solution to Fischer's analysis to describe the grain boundary and lattice diffusion effects in a semi-infinite polycrystalline medium.[44-45] Several others like Roe (1954), Levine (1960), MacCallum (1960) and Suzuoka (1961) presented models to determine the diffusant concentration as a function of grain boundary depth.[46-48] These models were primarily

for determining the effect of grain boundary diffusion with respect to lattice diffusion in semi-infinite medium. In 1976, Gilmer and Farrell developed a mathematical model based on Whipple's solution for describing the grain boundary and lattice diffusion for finite medium.[49] This solution could be applicable in understanding the diffusion effects in polycrystalline SMO film sensors. Parameters like film thickness and diffusion coefficient could play important roles in the sensor response in a diffusion limited case. In addition, the film morphology also plays an important role in developing a model to account for vacancy diffusion in polycrystalline films. In nanostructured films like glancing angle deposited (GLAD) films, which have cylindrical nanorods, vacancies can not only diffuse along the length of the cylinder but also radially.

In 2000, LeGore[50] was the first to develop a finite element model for oxygen vacancy diffusion coupled to surface oxidation reactions and reduction by $H_2S$ to estimate surface reaction rate constants and the vacancy diffusion coefficients from fitting experimental sensor response data for films of thickness 80 – 600 nm. The effects of diffusion were evident from the shape of the response with increasing film thickness. Conductivity measurements for reduction under vacuum at 300 °C and oxidation by 100 mbar $O_2$ at 300 °C suggested that the oxidation reaction was bulk vacancy diffusion limited, while the reduction reaction was surface reaction limited. For the reaction of $H_2S$ on $WO_3$ films in synthetic air, the response is surface reaction limited. In 2003, Pilling et al.[51] developed a kinetic reaction model to quantify the $WO_3$ gas sensor response and the limitations of the delivery system response time. They showed that at lower concentrations, the delivery system's response time became significantly longer and can preclude accurate measurements of the sensor response time. Response times were quantified experimentally and revealed effects attributed to adsorption on the tubing and the role of dead volumes (volume, not including the SMO film, the gas can occupy in the test cell). Therefore, the

faster response at higher concentration was probably an effect of the delivery system, not the sensor. In 2009, Shen et al.[36], experimentally showed that porous $WO_3$ films responded faster to $H_2$ gas due to higher surface area to volume ratio. In 2010, Deniz et al.[52] created $WO_3$ nanorods using glancing angle deposition (GLAD) to achieve higher surface area to volume ratios, and based on the results of Shen et al.[36] suggested that the nanostructure and morphology can improve magnitude of sensor response.

### 1.5 Rationale

Previous work, based on ESR studies, have shown that factors like operating temperature and the type of SMO sensing film are critical in determining the transduction mechanism in SMO film sensors. Even though ESR studies are valuable in determining the stability of surface adsorbed oxygen species, one should not rely totally on ESR data in determining the sensor transduction mechanism since actual sensor test conditions could be different from that used in ESR studies. In literature, the band bending model has been applied to sensors based on $WO_3$, $V_2O_5$, and $MoO_3$, assuming explicitly[53] or implicitly[18, 54-56] that the model is applicable. The band bending mechanism assumes that ionosorbed species are stable on the surface at sensor operating temperatures; the electrons in the near-surface region of the semiconductor are repelled by the localized charge of the ions at the surface causing upward band bending of the electrostatic potential and a depletion of electron carrier density near the surface. This implies that there are no other mobile charged species (e.g. dopants, point defects) that can neutralize the surface charge. This might be true for less reducible oxides ($SnO_2$ and $TiO_2$). But for reducible oxides ($WO_3$, $MoO_3$ and $V_2O_5$), where vacancy diffusion can be numerous orders of magnitude higher[57], surface charge neutralization can occur, which makes band bending unlikely in these materials. These papers, which imply band bending in $WO_3$ films, however are based on the

conduction mechanism in $SnO_2$ and $TiO_2$ based SMO film sensors where ESR studies, on these materials, have shown that surface ionosorbed oxygen species are much more stable at higher temperatures compared to high valency transition metal oxides. Moreover, in the band bending model proposed by Weimar et al.[31], the sensitivity varies with changing film thickness where thinner films exhibit higher sensitivity compared to thicker films. He also mathematically proved that for thicker films, film conductance has a weak dependence on target gas concentration. This might not be the case for the bulk conduction transduction mechanism. Moreover, even though there are a few models for band bending mechanism[31, 35-38], hardly any focus on developing comprehensive models for bulk conduction mechanisms in SMO films exists. The few papers[58-59] that have dealt with bulk conduction mechanism have failed to garner much attention.

In order to determine the bulk conduction transduction mechanism in transition SMO film, one needs to setup and solve differential equations taking into account both target gas-SMO film surface reactions and bulk diffusion of oxygen vacancies in the film. Solutions to these equations help in understanding the kinetics of oxygen vacancy formation and diffusion in the presence of a target gas (rate at which surface vacancies are formed, rate at which vacancies diffuse into the bulk of the film and how quickly equilibrium is reached). Using these solutions, a relationship between the sensor response and different kinetic and geometric parameters can be established. In this case the kinetic parameters are the gas reaction rates and vacancy diffusion coefficients while film thickness, film morphology and electrode geometry are geometrical parameters. $\Delta\sigma$ of the sensor depends on kinetic parameters whereas $\tau$ of the sensor (defined in section 1.3) can depend on both kinetic and geometric parameters. Geometric parameters are typically adjustable parameters since they are defined in the design/fabrication phase. Kinetic parameters depends on operating temperature and SMO film type. Once the dependence of $\tau$ and

$\Delta\sigma$ on these adjustable parameters are known, it may be possible to design faster responding, higher sensitivity, application specific sensors.

None of the existing papers on bulk conduction models have studied the effect of both kinetic and geometric parameters in determining the overall sensitivity and response time of the films. LeGore[50], in his thesis attempted to model a planar sensor response to a target gas by combining both surface reaction and bulk vacancy diffusion effects. However his model did not identify any unique sensor response characteristics that could differentiate a response limited by surface reaction or vacancy diffusion. Moreover, LeGore's model focuses only on planar film sensors and does not show the effect of film geometry on response time of non-planar films. Thus, designing fast responding application specific sensors was not possible based on the model. Relative to non-planar film sensors, currently no model exists to show the relation between sensitivity and response time of nanostructured (films such as nanorods, nanowires and nanofibers) films to changes in surface to volume ratio, diffusion coefficient, film thickness, reaction rates and gas concentration.

Thus if a kinetic model for the surface reaction limited and bulk diffusion limited cases for bulk vacancy conduction transduction mechanism in SMO films can be developed, the following would result:

- Determination as to how the sensor response due to bulk vacancy transduction mechanism is different from band bending transduction mechanism.
- Determination as to whether the sensor response due to bulk vacancy conduction transduction mechanism is diffusion limited or surface reaction limited.
- Development of mathematical expressions for the sensitivity and response time as a function of sensor parameters such as film thickness, diffusion coefficient and reaction

rates associated with the bulk vacancy conduction transduction for surface reaction limited and bulk vacancy diffusion limited cases.

- Suggestion of application specific SMO films (planar and nanorod films with certain film thickness, nanorod height and radius for better sensitivity and faster response time) based on the sensitivity and response time expressions.

**1.6 Objectives**

In this thesis, both surface reaction limited and bulk vacancy diffusion limited models associated with the bulk vacancy conduction mechanism are studied with a focus on kinetic and geometric parameters that could affect sensor sensitivity and response time. For a surface reaction limited case, the bulk vacancy diffusion process is assumed to be very fast. In this case both sensitivity and response time of the film is governed by the time taken for the gas to react with the surface of the film to produce surface vacancies which then diffuse quickly into the bulk. Parameters like reduction and oxidation rates, surface area to volume ratio (in this thesis volume to surface area is used) and gas concentration could play important roles in determining sensor response for this case. For a bulk diffusion limited case (bulk in this paper refers to the entire volume of the film), the surface reaction is assumed to be fast such that a constant flux of vacancies is available at the film surface. In this case sensitivity depends on the surface reaction rate, which determines the total number of surface vacancies but the response time is dependent on the vacancy diffusion coefficient and film thickness which determine how quickly the bulk vacancies diffuse and equilibrate throughout the volume of the film.

The main objective of this thesis is the development of kinetic models for bulk conduction mechanism for both the bulk vacancy diffusion limited and surface reaction limited cases. Based on these models derivation of expressions for the magnitude of the change in steady

state conductivity of the sensor when exposed to the target gas and air ($\Delta\sigma$) and response time ($\tau$) of these sensors as a function of various kinetic and geometric parameters will be developed. The results from the models will then be compared to experimental sensor test data to determine their practical usability and also to determine whether the sensor response is due to band bending mechanism or bulk vacancy conduction mechanism. If the sensor response is due to bulk vacancy conduction, further analysis will be performed to determine whether the response is surface reaction limited or bulk diffusion limited. Suggestions will then be made on the modification of kinetic and geometric parameters to develop sensors with better sensitivity and faster response time to the target gas of interest.

In order to compare the model predictions to actual experimental data, two different types of SMO film structures will be considered. The first type is a standard polycrystalline planar film while the second type is a glancing angle deposited (GLAD) film with nanorod morphology. The GLAD film, with their nanorod architecture, have larger surface to volume ratio[52] which could help in fast detection of low concentrations of target gases compared to planar films. The SMO material used in the fabrication of planar and GLAD films was chosen to be tungsten trioxide ($WO_3$). $WO_3$ is a reducible transition metal oxide and has been used for hydrodeoxygenation applications[60] where surface vacancies are formed and annihilated, and therefore makes a good material for studying bulk vacancy conduction mechanism. Their ability to operate at elevated temperatures for long periods of time also makes $WO_3$ a viable option for gas sensing applications.[18, 61] The target gas chosen in this study is ammonia ($NH_3$) which is toxic to humans. Ppb concentrations of $NH_3$ also plays a role in climate change and in the detection of certain diseases.[62-64] Both GLAD and planar $WO_3$ films were doped with gold (Au) since it has been reported that by doping $WO_3$ with catalysts like platinum (Pt), palladium (Pd) and gold (Au), the

sensitivity of the sensor to gases like $NH_3$ is enhanced.[18, 65] This could possibly be due to the fact that these surface catalysts can act as adsorption /dissociation centers which lowers the dissociation energy of the target gas molecule and this in turn affects the surface reaction rates on the SMO film thereby affecting the concentration of surface lattice oxygen vacancies.

To model the surface reaction limited case for $NH_3$ reaction on Au doped $WO_3$ films, an understanding the surface adsorption/reaction centers at the film surface, as well as identifying the products of the reaction would enable in obtaining balanced reaction for $NH_3$ gas reaction on the film surface. The role of the Au additive in determining the overall reaction rate could also be helpful in improving the overall accuracy of the model. This can be achieved using analytical studies (Gas Chromatography/Mass Spectroscopy (GC/MS) and Diffuse Reflectance Infrared Fourier Transform Spectroscopy (DRIFTS)) on Au-loaded $WO_3$ powder catalysts. These GC/MS and DRIFTS studies were performed on powder catalysts with well-defined particle sizes since the surface area (which is important in determining reaction rates) of the catalysts can be accurately determined using Brunauer-Emmett-Teller (BET) surface area analysis. Also, powder catalysts are readily available. GC/MS and DRIFTS studies are done using pure and 0.1% w/w (mass fraction) Au-loaded $WO_3$ powders. By comparing the % conversion of $NH_3$ (total % of $NH_3$ converted into reaction products) on pure and 0.1% w/w Au-loaded $WO_3$ powder catalyst, using GC/MS, the surface reaction rates can be determined and also the effect of Au on the $NH_3$/0.1% w/w Au-loaded $WO_3$ catalyst reaction. Besides determining surface reaction rate, % yield of reaction products (total % of reaction products formed as a result of $NH_3$ conversion) can also be obtained as a function of reactor temperature. This can provide input to the development of balanced kinetic equations for the $NH_3$/Au doped $WO_3$ film surface reaction limited models. DRIFTS would indicate the $NH_3$ adsorption sites on the $WO_3$ catalyst, as well as

the rate of reduction of the surface in the presence of $NH_3$ gas. By comparing the change in peak area, at a particular frequency associated with surface reduction as a function of time, to the known integrated rate equations, the order of $NH_3$ reaction on both 0.1% w/w Au-loaded and pure $WO_3$ catalyst can be obtained. This will also be helpful in getting balanced reactions for modeling of $NH_3$/ Au doped $WO_3$ film surface reaction limited models.

### 1.7 Organization

This thesis is organized into six chapters, the first of which is the introduction. The second chapter details the theoretical background which will facilitate the understanding of both the surface reaction limited and bulk vacancy diffusion limited mechanisms. The third chapter presents the surface reaction and diffusion models associated with both GLAD and planar films. The fourth chapter describes the experimental methods associated with sensor fabrication and testing, powder sample preparation along with the powder characterization technique and analytical setup involving GC/MS and DRIFTS. The fifth chapter presents the results of the GC/MS and DRIFTS study and also compares the models to the sensor test data. The sixth chapter presents the summary, conclusions and potential future work.

# 2. BACKGROUND

In this chapter, a review of the theory of kinetics of gas sensing associated with both the band bending and bulk vacancy diffusion mechanisms is presented. Previous work relating to gas –SMO surface reactions and their role in both mechanisms is also presented along with the role of grain boundaries and various defects such as line defects, point defects and planar defects in the film bulk. Since both GLAD and planar $WO_3$ film sensors are used in this study, the chapter also presents a detailed explanation of the morphology of both GLAD and planar $WO_3$ films.

## 2.1 Kinetics of Surface Reactions

The reaction mechanism of gases, through adsorption and desorption of gases on a film surface can take place through three well known mechanisms. The first mechanism, which was proposed by Langmuir in 1921 and further developed by Hinshelwood in 1926, relates to two molecules adsorbing on neighboring sites and undergoing a bimolecular reaction to form products. The second mechanism was proposed by Eley and Rideal in 1938 and involves a reaction taking place between an adsorbed molecule and a reactant in the gas phase. The third mechanism, proposed by Mars and van Krevelin in 1954, involves an oxidation reaction with lattice oxygen species whereby the lattice is an active part of the reaction process. All three mechanisms, clearly explained in a review paper by Bettuzzi[66], are summarized as follows.

- *The Langmuir-Hinshelwood* mechanism involves two reactants adsorbing on nearby surface sites before a reaction takes place between them. This mechanism is significant to the band bending phenomenon where a target gas such as $NH_3$ adsorbs on the surface of the film and reacts with the surface chemisorbed oxygen ions to form products. These reaction products desorb leading to the release of trapped electrons.

- *The Eley-Rideal* mechanism involves only one of the reactants adsorbing on the surface while the other reactant interacts with the adsorbed species only from the gas phase. The hydrogenation of $CO_2$ during formate synthesis follows this mechanism where hydrogen is the adsorbed species.[66]
- *The Mars-Van Krevelen* mechanism involves the surface as an active part of the reaction and a reactant forms a chemical bond with the surface.[66] In this mechanism, for a metal oxide, the target gas first adsorbs on a surface site and then reacts with the surface lattice oxygen species to form reaction products. These products desorb from the surface leaving behind oxygen vacancies. Reactions with gas phase oxygen can then fill these vacancies. The selective oxidation of propene to acrolein on $MoO_3$ and $WO_3$ bronze follows this mechanism.[60, 67]

Relative to determining which mechanism predominates in SMO sensors, the operational temperature of the sensor is critical. Typically SMO sensors are operated in a temperature range of 200-500 °C. As mentioned in the first chapter, for metal oxides like $SnO_2$, in the aforementioned temperature range, target gas interactions take place with ionosorbed oxygen species leading to band bending[31, 68] while in transition metal oxides like $V_2O_5$ and $WO_3$ at temperatures over 350 °C,[27-28] the target gas reacts with lattice oxygen species leading to bulk conduction mechanism. So in a temperature range where chemisorbed oxygen species are present, the most likely gas reaction mechanism would be the Langmuir- Hinshelwood where the gases adsorb on the surface and then react. But for materials like $WO_3$ operating at temperatures over 350 °C, the reaction mechanism is likely to be the Mars-Van Krevelen type mechanism.

### 2.1.1 Surface Reaction Rate Effects on Sensitivity and Response Time of SMO Film Sensors

The surface reaction rate directly affects the sensitivity and response times of SMO sensors. For the purpose of explaining the effects of reaction rates on sensitivity and response time, consider the reaction of hydrogen on a metal oxide film sensor in the presence of air ($O_2$).[41] The following are possible reactions that could happen on the film surface,

$$\frac{1}{2}O_2 + e^- \rightleftharpoons_{k_2}^{k_1} O^-, \tag{2.1}$$

$$H_2 \xrightarrow{k_{diss}} 2H\,, \tag{2.2}$$

and

$$2H + O^- \xrightarrow{k_3} H_2O + e^-. \tag{2.3}$$

From the above set of equations, during a chemical reaction some species are consumed while other species are formed. The *rate of conversion* is typically the change in number of moles of the reactants per unit time. The ***rate of a reaction*** is dependent on the particular reaction process and is typically the rate of conversion (or rate of formation) per unit area. Reaction (2.1) is a reversible reaction taking into account both the oxidation and reduction of the SMO surface in air where chemisorbed oxygen species are formed (where atomic oxygen takes an electron from the metal oxide surface to form $O^-$) or removed (desorbing as gaseous oxygen by releasing trapped electrons) respectively. In this case $k_1$ $and$ $k_2$ are the rate constants associated with the rate of oxidation and reduction respectively of the metal oxide surface. Reaction step (2.2) shows the dissociation of $H_2$ gas where $k_{diss}$ is the rate constant associated with the rate of hydrogen dissociation. Reaction step (2.3) shows the reduction of the metal oxide surface in the presence of $H_2$ gas resulting in the formation of $H_2O$ which then desorbs leaving behind a free electron. Here $k_3$ is the rate constant associated with the rate of consumption of the ionosorbed $O^-$ species in the presence of the $H_2$ target gas.

From the three equations, it is clear that an increase in reduction rates will result in more electrons injected into the metal oxide surface resulting in an increase in $\sigma$ (conductivity) in the metal oxide sensor while an increase in oxidation rate will result in electrons being removed from the metal oxide surface which in turn will cause a decrease in $\sigma$ of the sensor. The dissociation rate does not play a direct role in the conduction mechanism but it generally determines the sensor response time, which is the time taken for the sensor to reach 90% of its final steady state value, and is dependent on the rate limiting step of the reaction. The actual transduction mechanism involved in changing conductivity in metal oxide films will be discussed in section 2.2.

## 2.2 Band Bending Mechanism

### 2.2.1 Surface States and Energy Band Structure in As Deposited SMO Films

After deposition, the metal oxide film surface is discontinuous as the crystal lattice periodicity is highly interrupted with metal cations and oxygen anions present at the surface along with oxygen vacancies distributed uniformly throughout the film. These surface cations and anions lead to localized energy bands.[9] Determining the position of these bands is possible using computational methods like Density functional theory (DFT), Hartree-Fock method, full potential muffin tin approximation (FP-LMTO) or experimental methods like angle resolved photoemission spectroscopy (ARPES) and electron energy loss spectroscopy (EELS).

For nearly stoichiometric post transition metal oxides like ZnO and $SnO_2$, the valence band is primarily due to the filled O 2p orbitals separated from a metal based conduction band which is due to the metal s orbitals which are mostly empty.[69] The main difference between these oxides and the nearly stoichiometric transition metal oxides like $WO_3$ and $V_2O_5$ is that, the conduction band is formed from the metal d orbitals rather than s orbitals and the conduction

band is empty only for $d^0$ transition metal oxides like ($WO_3$[70] and $V_2O_5$) while in oxides like $V_2O_3$, $Ti_2O_3$ and FeO which are $d^n$ transition metal oxides with n>0,; there are some electrons in the conduction band.[69] The presence of defects like oxygen vacancies, metal vacancies and interstitials can alter the electronic structure of the metal oxide surface and bulk. The electronic structure of post transition and transition metal oxide surfaces with defects have been extensively studied over the years.[69, 71-76] Some of the results of these studies relating to ZnO and $WO_3$ is discussed later in this section. Since the electronic structure and behavior of these metal oxides depend on the position of the bands and also on the location of the defect states present in the band gap, some of the studies relating to defect states and associated models from these studies are discussed below.

Levine and Mark[77] developed a single electrostatic model for charge neutral surfaces of ionic crystals of stoichiometry MX. In this model, the valence and conduction band does not include dispersion. On an adsorbate free ionic crystal surface, the acceptor states due to metal cations lie below the conduction band and the donor states due to the anions lie above the valence band, symmetric with respect to the center of the band gap as shown in figure 2.1.[77] The assumption in this model is that the surface is the same as the bulk but the surface has a reduced Madelung constant. The ratio of the surface band gap to the bulk band gap depends on the Madelung constant. The surface cations and anions can act as electron and hole traps respectively, which can be populated under photon-induced excitation, resulting in the formation of depletion type Schottky barrier. When the illuminated surface is heated to 50 °C[78], the traps relax and the system returns to a flat band condition. The location of these surface electron traps on CdS are such that they should be above energy levels of adsorbed species, such as $O^-$ , so that electrons can move from the traps to the surface adsorbate ions leading to band bending.

This model based on an electrostatic approach to surface states on ionic crystal surfaces has limited applicability for metal oxides as the surface of some metal oxides like $WO_3$ are more covalent than the bulk.[69] Moreover, the model of Levine and Mark cannot take into account the role of vacancies and interstitials, which result in other types of localized energy levels in the band gap changing the electronic structure of the metal oxide.

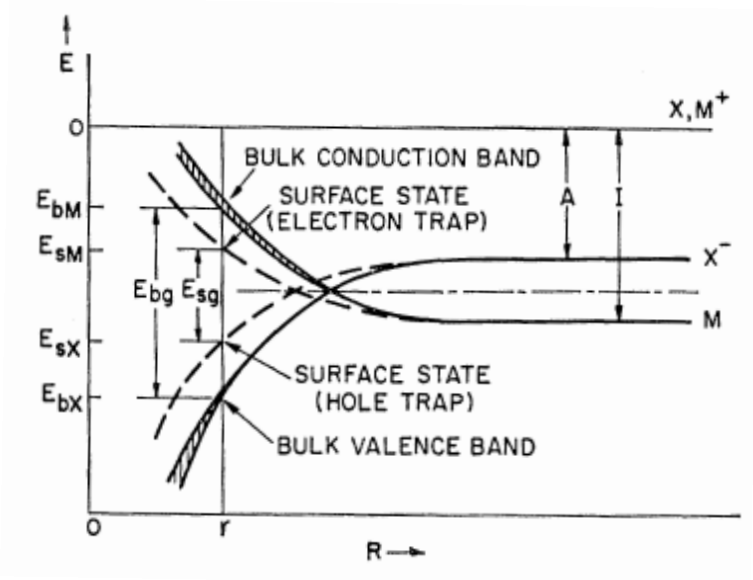


**Figure 2.1**. Energy levels as a function of interionic distance, R, for ionic crystal MX. At equilibrium distance, r, configuration is ionic due to Madelung stabilization energy.[77]

Like Mark and Levine, Morrison et al. have proposed three simple models, based on an electrostatic approach, for the location of these energy bands on the ionic crystal surface.[79] The location of energy bands in each model is shown in figure 2.2. Figure 2.2 (a) shows the double band case where there are both surface acceptors and donors present. Figure 2.2 (b) shows a case where there is a high concentration of surface vacancies such that there is an excess amount of free carriers at the surface compared to the bulk resulting in an accumulation layer. Figure 2. 2 (c) is a case where there is an excess amount of metal vacancies on the SMO film surface

resulting in an inversion layer where the majority carriers are holes. This model is more appropriate in the case of $Cu_2O$ which is a p type SMO.

These proposed models are very general and the most important question is whether these models are applicable to all metal oxides.

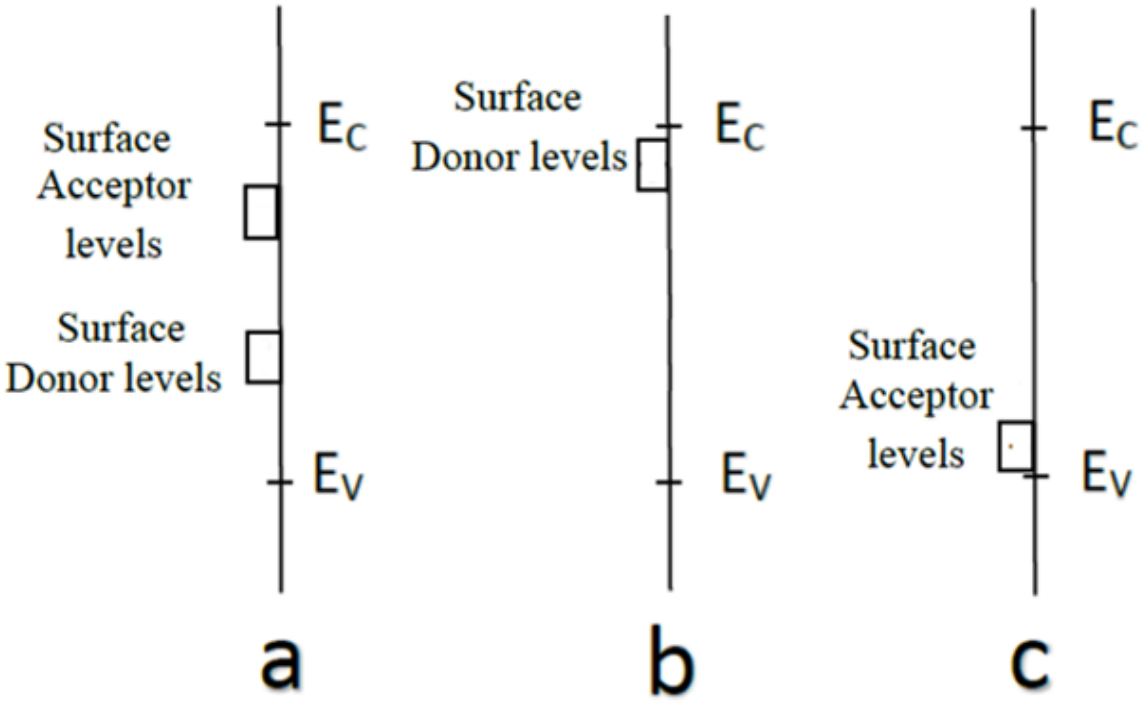


**Figure 2.2**. Various models for the surface metal cation acceptor and surface oxygen donor levels (a) Double layer model, (b) Accumulation layer model and (c) Inversion layer model.

For post transition metal oxides like ZnO, according to Boccuzzi et al., there are both oxygen vacancies and metal vacancies or oxygen interstitials present in ZnO leading to localized energy levels in the metal oxide band gap.[71-72] ZnO has a band gap of 3.2 eV where the filled valence band is primarily due to O 2p states and the conduction band is due to Zn 4s states and are insulators when purely stoichiometric.[69, 71-72] However most metal oxides are not stoichiometric and have defects in them. Gopel et al. have mentioned the presence of both donor

type and acceptor type defects present on the ZnO surface.[80] The oxygen vacancy's donor levels are located 0.05 eV and 0.18 eV below the conduction band minima (0.18 eV is for the singly ionized donor level) and the acceptor level is located 0.7 eV above the valence band maxima.[71-72] The model of donor and acceptor states in ZnO is similar to that shown in figure 2 (a) except that the donor levels are close to the conduction band and the acceptor levels are close to the valence band. The bulk and surface oxygen vacancies are very similar and the electronic levels are at the same distance from the bottom of the conduction band. At high temperatures, electrons are injected into the conduction band from the donor states and they are highly delocalized resulting in plasmon phonon coupling.[71]

The electronic structure of transition metal oxides is slightly different from post transition metal oxides due to variable oxidation states of transition metal oxides. The energy difference between a cation $d^n$ configuration and either $d^{n+1}$ or $d^{n-1}$ configuration is small.[69] In the case of $WO_3$, the conduction band is due to W 5d states and the valence band is made up of filled O 2p states and the band gap of $WO_3$ is approximately 2.6 eV.[70] For near stoichometric $WO_3$, the conduction band is empty and it behaves like an insulator. Berak et al.[81] have done Hall Effect measurements on $WO_3$ single crystals and have proved that they are n type semiconductors at room temperature, where the majority carriers are electrons. Moulzolf et al.[82] extended the Hall Effect studies done by Berak et al.[81], to sub-stoichiometric polycrystalline $WO_3$ thin films, to show the n type behavior of $WO_3$ thin films at room temperature. This is due to the fact that sub-stoichiometric $WO_3$ have shallow oxygen vacancies (close to the conduction band) that can act as electron donors.[69] Berak and Sienko have reported ionization energies between 0.009 eV and 0.016 eV for monoclinic $WO_3$ and these shallow donor levels account for the room temperature conductivity of $WO_3$.[81, 83] Moulzolf et al.[82] have determined these donor sites to be

approximately 0.13 eV from mobility and conductivity data obtained from Hall effect measurements. Recently Wang et al.[76] have used hybrid Density functional theory (DFT) to determine the location of these donor states and determined that these are shallow states and they introduce electrons into the conduction band resulting in the n type behavior of $WO_3$ even at room temperature.

Band bending or depletion layer occurs as a result of oxygen ionosorption in which adsorbed oxygen traps free electrons on the metal oxide surface. Reactions associated with oxygen and target gases have already been discussed in section 1.2.1 and 1.2.2. Oxygen, which constitutes 20% of ambient air, chemisorbs on the surface of the film as $O^-$ and $O_2^-$ on exposure, resulting in localized surface acceptor states on the film surface. Figure 2.3 describes the situation after the electrons have been trapped by these localized surface acceptor states. A **depletion layer** is formed with negative charge associated with the localized surface acceptor states on the SMO film surface and the uniformly distributed positive charged donors (ionized) near the surface of the SMO film. Due to charge separation, a layer depleted of mobile carriers called the depletion region is formed. This depletion layer, creates a potential barrier at the film surface which the free electrons in the SMO film bulk must overcome to reach the film surface.[79] From the point of view of sensor response, the overall effect is a decrease in film conductivity when the film is exposed to an oxidizing gas and an increase in conductivity in the case of a reducing gas. Band bending transduction mechanism has been widely reported for ZnO, $TiO_2$ and $SnO_2$ film sensors.[84-85]

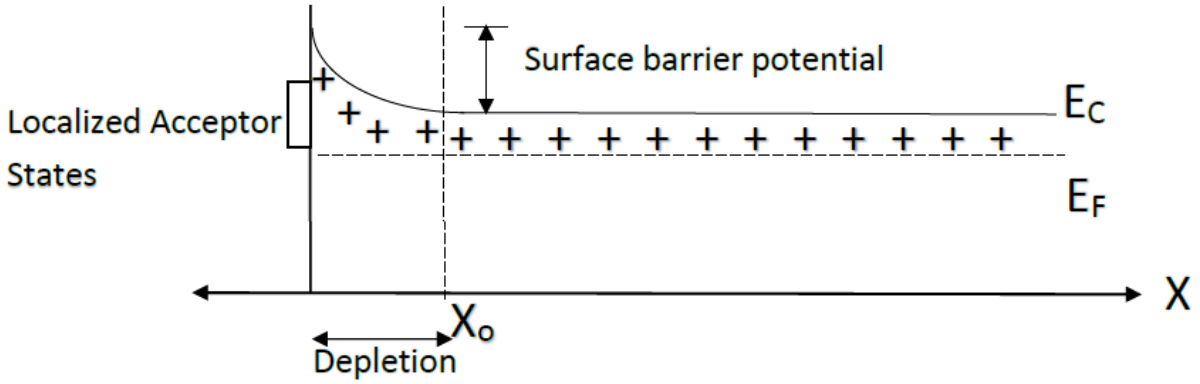


**Figure 2.3**. Depletion layer formed as a result of electrons moving into the surface acceptor states.

In order to obtain an expression for the variation of potential barrier as a function of distance into the SMO film, one needs to solve Poisson's equation subject to the charge distribution and boundary condition at the film surface and at the depth of the depletion region. The solution to Poisson's equation is presented in Appendix A where the height of the potential barrier ($V_s$) at the SMO film surface is the following[86],

$$V_s = \frac{q\, n_D}{2\varepsilon} x_0^2 \,. \tag{2.4}$$

where $q$ is the electronic charge, $n_D$ is the density of oxygen vacancies in SMO film, $\varepsilon$ is the dielectric constant of the film and $x_0$ is the depletion layer width.

In actuality, annealed SMO films are polycrystalline and consists of many crystallites. An example of a porous polycrystalline film prepared using e-beam evaporation and annealed is shown in figure 2.4. The surface of the crystallites is negatively charged with partially occupied surface acceptor states. Also shown in the figure is the depletion region. From the figure, most of the resistance in polycrystalline SMO films occurs in the depletion region. When a potential is applied, the electrons in the crystal lattice must overcome the potential barrier at the surface of each crystallite along with a potential introduced by boundaries between neighboring crystallites

to move from one crystallite to another. This resulting potential may be slightly different for each crystallite due to the different crystallographic orientations of the crystallites and the direction of the electric field associated with the applied voltage.

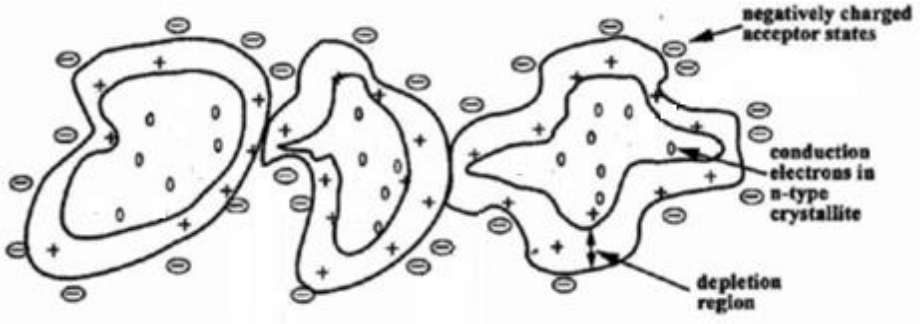


**Figure 2.4**. Two dimensional view of three crystallites in an annealed porous polycrystalline film prepared using e-beam evaporation. The negative sign is associated with the surface acceptor states, the positive sign is associated with the ionized donors and the circles are associated with conduction electrons in the crystallites.[9]

### 2.3 Bulk Vacancy Conduction Mechanism in SMO Film Sensors

In the previous two sections, the location of energy bands associated with surface metal anions and surface oxygen cations in an as deposited SMO film in vacuum is presented. It was pointed out that experimentally in the presence of redox gases, the most appropriate band structure is the double layer. Further it was noted that upon exposure to redox gases most of the SMO films like $SnO_2$, ZnO and $TiO_2$ exhibit the band bending transduction mechanism. However for some metal oxides like $WO_3$, $V_2O_5$ and $MoO_3$, the transduction mechanism due to band bending may be appropriate at low temperatures, but at high temperatures, the bulk conduction mechanism predominates. This is due to the fact that when a SMO film is taken out of the vacuum system and exposed to ambient air ionosorption of oxygen occurs on the film surface. As mentioned in section 1.2, as film temperature is increased, the ionosorbed superoxide

becomes less stable above 150 °C and dissociates to form $O^-$surface species. The stability of these species also depend on the temperature of the film and also on the type of metal oxide used. For metal oxides with higher cationic charge, like $WO_3$, $MoO_3$ and $V_2O_5$, the $O^-$ species are more prone to be less stable at higher temperatures than in metal oxides with lower cationic charge like $SnO_2$, ZnO and $TiO_2$. In the case of $WO_3$, as temperature is increased, the $O^-$ species move into the surface oxygen vacancy sites to form $O^{2-}$species as given in equation (1.3) in chapter 1. In this case when the film is then exposed to a redox target gas, there can be two possible reactions. The target gas can either react with the surface $O^{2-}$ species to create surface vacancies resulting in an increase in film conductivity for a reducing target gas as given by equation (1.7) or react with surface oxygen vacancies resulting in their annihilation causing a decrease in film conductivity for an oxidizing target gas as shown in equation (1.8) in chapter 1. The resulting mechanism is bulk vacancy conduction mechanism.

### 2.3.1 Mars-Van Krevelen Mechanism

Referring to the reaction mechanisms discussed earlier in section 2.1, it appears that the target gas-SMO film reaction in $WO_3$ and similar oxides which exhibit bulk vacancy conduction mechanism follows the Mars-Van Krevelen mechanism. This mechanism was proposed by Mars and Van Krevelen in 1954[87] and involves a redox process. As per this mechanism, when an SMO film is exposed to a reducing target gas, the lattice oxygen ($O^{2-}$) is consumed from the oxide surface on reacting with that particular target gas leading to partially oxidized products and oxygen vacancies, which are then replaced by $O^{2-}$ when exposed to ambient air through dissociative adsorption of $O_2$[88-89] and bulk diffusion of oxides.[90]

Thibodeau et al.[60] have shown conversion of acrolein to propene using hydrodeoxygenation mechanism on $WO_3$ bronze powder catalysts. Also, Moberg et al.[67] have

theoretically predicted the potential energy change for hydrodeoxygenation of acrolein to propene on $MoO_3$ surface. Both these reaction mechanisms are similar to Mars-Van Krevelen mechanism. However, since these reactions involve reduction and not selective oxidation, these cannot be considered as typical examples of Mars-Van Krevelen mechanism. One example of Mars-Van Krevelen mechanism was proposed by Grasselli[67, 89] involving the selective oxidation of propene on bismuth molybdate powder catalyst to form acrolein at 320 °C as shown in figure 2.5. As depicted in the figure, propene chemisorbs on the catalyst (A) and then undergoes hydrogen abstraction by bridging oxygen (Bi-O-Mo) associated with the catalyst to form a π-allyl intermediate (B). The reaction of $NH_3$ on $WO_3$ surface would undergo a similar hydrogen abstraction process as that of propene on bismuth molybdate catalyst. The next step involves the oxygen attached to Mo inserting into the π-allyl species to form σ-allyl intermediate (C). This is followed by a second hydrogen abstraction on Mo site to form acrolein and water leaving behind an oxygen vacancy (reduced Mo site) (D). Re-oxidation of the active site and vacancy filling follows using gaseous oxygen follows (E). Vacancies can also be filled by bulk diffusion of lattice oxygen from neighboring sites[89] and even though this is a part of the Mars-Van Krevelen mechanism, the discussion would be best suited in the vacancy diffusion section.

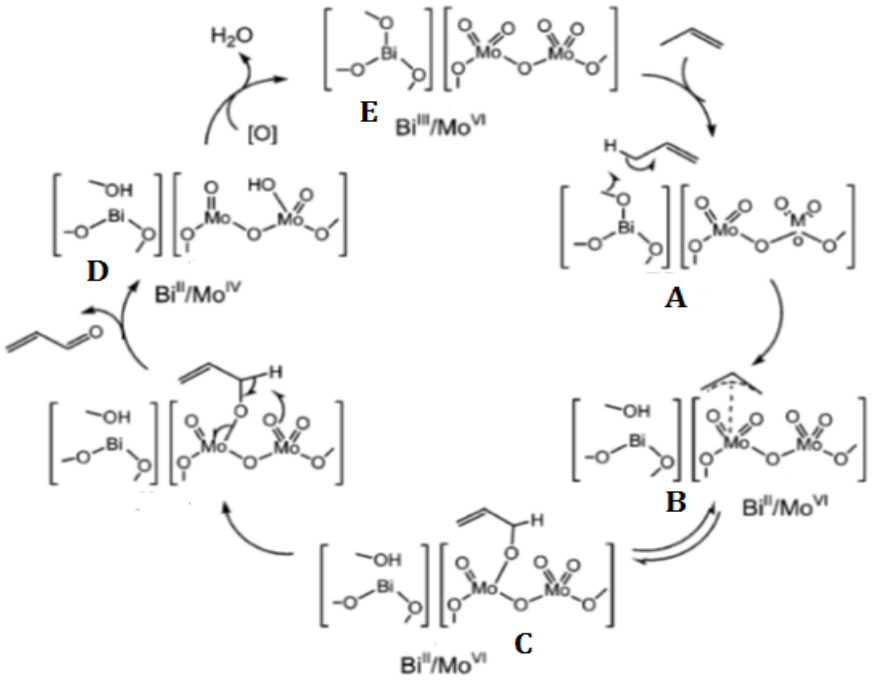


**Figure 2.5**. Mars-Van Krevelen mechanism showing the selective oxidation of propene to acrolein on bismuth molybdate catalyst.[89]

Once it was experimentally proved that lattice oxygen plays a role in reaction mechanisms (Mars-Van Krevelen) like the one shown by Grasselli, the next step was to determine the role that metal oxygen (M-O) bond strength plays in chemical reactivity and selectivity. If the M-O bond strength is too strong, no reaction will occur; if it is too weak, the metal oxide catalyst will be highly reactive which in turn affects its selectivity.[89] Simply put, for the selective oxidation of propene to acrolein, if the catalyst used is highly reactive, one may not obtain partially oxidized product like acrolein but $CO_2$. Figure 2.6 shows a schematic of the effectiveness of the metal oxides to undergo a redox reaction in relation to the M-O bond strength.

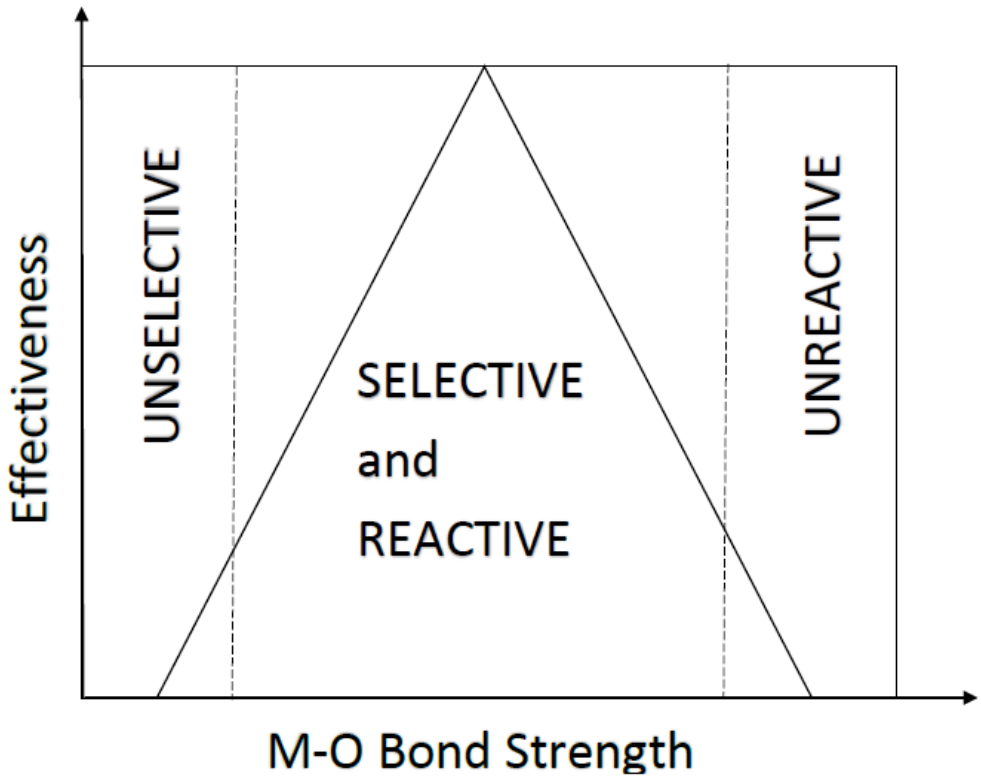


**Figure 2.6.** Effectiveness of the metal oxides to be selective and reactive based on bond strength.

Ponec et al. presented M-O bond strength values from literature and how they impact hydrogenation of acetic acid to acetaldehyde.[91] They preferred to have a reducible oxide with intermediate M-O bond strength for their application. For example, the tungsten oxygen bond strength is about 500 $\frac{KJ}{mol}$ and has applications as a catalyst in hydrodeoxygenation[60] processes apart from gas sensing applications. Figure 2.7 shows the relative M-O bond strength of various metals. From the figure, one can see that $WO_3$ is a much more reducible oxide than MgO or $TiO_2$.

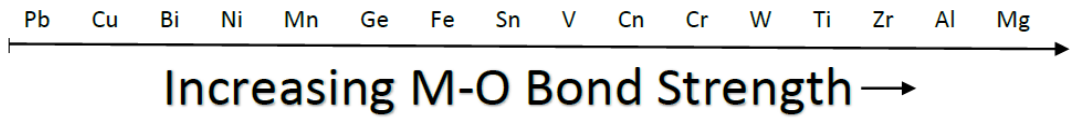


**Figure 2.7**. M-O bond strength [adapted from Ponec et al.[91]].

### 2.3.2 Vacancy Formation and Conductivity Changes in SMO Films due to Gas Reaction

As mentioned earlier, the gas-surface reaction mechanism involves vacancy formation like the Mars-Van Krevelen pathway which is a redox mechanism. The polycrystalline film is first reduced by a target gas ($NH_3$ in this example) followed by exposure to oxygen gas as shown in figure 2.8. The expression for conductivity is given by

$$\sigma = n\, e\, \mu. \tag{2.5}$$

$n$ is the number of carriers per unit volume, e is the charge of an electron and μ is the mobility of the carriers at the particular operating temperature ($\mu \propto T^{-3/2}$). During a reduction reaction, lattice oxygen is consumed (more vacancies) resulting in an increase in the number of free electrons ($n$) (each $O^{2-}$ leaves behind 2 $e^-$). Thus, electrical conductivity of the material increases when the metal oxide film surface gets reduced. The effect is the opposite for an oxidation reaction on the film surface. Thus for n type metal oxides like $WO_3$, the conductivity is due to the formation or removal of electrons due to vacancies being created or annihilated.

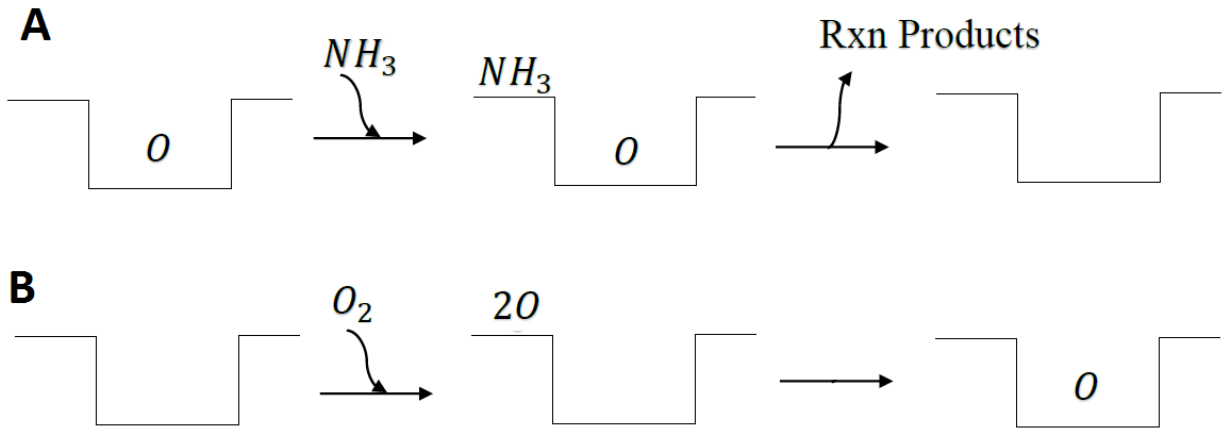


**Figure 2.8.** Lattice vacancy formation (A) and elimination (B).

For p type metal oxides like $Cu_2O$, conduction due to holes arises as a result of oxygen excess in the material due to copper vacancies, $V_{Cu}$, or oxygen interstitials, $O_i$.[92] Shao et.al have

used copper oxide nanowires to detect $NH_3$ gas and have reported that the electrons released due to the interaction of $NH_3$ on the nanowire surface results in the release of free electrons resulting in a decrease in hole concentration and thereby an increase in resistance.[93]

### 2.3.3 Bulk Defects and Diffusion Processes in Polycrystalline films

Polycrystalline films are made up of crystallites (grains) that are separated by grain boundaries. Film defects are present both at the surface and in the bulk of these films, but the exact location and density of defects can vary from one film to another. The bulk transduction mechanism due to creation of vacancies, which are point defects, have been discussed in the previous sections. Point defects (vacancies) are present on the grains as well as along the grain boundaries. Vacancy diffusion mechanism in polycrystalline metal oxide films is the result of lattice oxygen migration from a bulk site to a vacancy site. A brief background study of the different types of defects and the diffusion of these defects are presented in this section. At any temperature, solids contain structural and compositional defects and these are often divided into three main groups[94]:

1. Point defects
2. Planar defects
3. Line defects

Some of these defects include vacancies, interstitials (point defects), shear planes (planar defect but some also call it an extended point defect), and dislocations (line defect). Since defect diffusion can control the response time of the sensor, a brief overview of the defect diffusion mechanisms are given below:

- Defect Diffusion along the Lattice
- Defect Diffusion along Grain Boundaries

Lattice diffusion generally refers to defect diffusion in single crystal film lattice, where there are no grain boundaries. In this thesis, lattice diffusion refers to defect diffusion in the crystallite or grains (not involving grain boundaries). Since polycrystalline films also contain crystallites or grains, the term "lattice diffusion" also refers to defect diffusion within the crystallites of these films. The following sections give a detailed explanation of defect diffusion mechanisms along the lattice and grain boundaries.

#### 2.3.3.1 Defect Diffusion along the Lattice

##### 2.3.3.1.1 Point Defects

Point defects in polycrystalline metal oxide films typically consist of

- Vacancies
- Interstitial atoms

Non-stoichiometric metal oxides like $WO_3$ consist of an excess amount of metal and the vacancies in such materials are mostly oxygen vacancies. Lattice diffusion takes place through the migration of vacancies or interstitial atoms.[94] According to Grasselli et al.[89], the diffusion of surface vacancies, formed as a result of a reduction reaction, into the bulk in reducible metal oxides is due to the migration of surrounding bulk lattice $O^{2-}$ species to fill the surface vacancy resulting in vacancy diffusion into the bulk. It has also been reported by Goddard et al.,[95] for the selective oxidation mechanism of propene to acrolein using bismuth molybates, that lattice oxygen migration (resulting in vacancy diffusion) is responsible for the re-oxidation of the reduced Mo sites. In some metal oxides, like $Fe_3O_4$, there are interstitial atoms present in the oxide.[94] These atoms jump to an interstitial site to a neighboring interstitial site resulting in a process called the interstitial mechanism. However this mechanism is not common in large ions of metal oxides as their movement is restricted.[94] Figure 2.9 shows the two different mechanisms

for diffusion. Carrasco et al.[96] have studied oxygen vacancy diffusion in several metal oxides and have reported that the Madelung potential associated with charge distribution controls the oxygen vacancy diffusion in highly ionic oxides like $Al_2O_3$, CaO and MgO. They calculated the energy barrier for oxygen vacancy diffusion for these metal oxides and observed that the barrier varied like MgO>$Al_2O_3$>CaO. For oxides of Mo, V, and W, the vacancy diffusion barrier is low.[96]

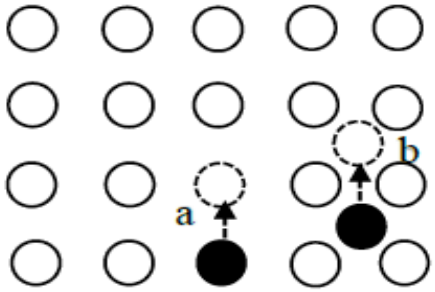


**Figure 2.9**. Diffusion mechanism in metals (a) Vacancy Diffusion mechanism (b) Interstitial mechanism.

**2.3.3.1.2 Planar Defects**

In materials like $WO_3$, there are planar defects (also called Wadsley defects) which are formed due to the ordering and elimination of point defects.[94] $WO_3$ consists of corner sharing octahedra that link up via shared oxygen atoms. When this material is exposed to a reducing gas, oxygen vacancies are formed which then migrate to certain planes within the crystal. Here the vacancies are eliminated by a process, where the octahedron collapses into the vacant sites whereby the structure closes up to form a plane containing edge sharing octahedra.[97] This results in a change in anion coordination along the plane resulting in the elimination of oxygen vacancy defects. Ordered Wadsley defects are called crystallographic shear (CS) planes and figure 2.10 shows the entire formation of shear planes.

At sufficiently low defect concentration, the higher entropy of point defects could lead to shear plane dissociation provided that the free energy associated with the point defects are much lower than that of the shear planes.[98] The conduction band electrons created during reduction process are trapped by the shear plane and is liberated when the shear planes dissociate.[98] In materials like $MoO_3$, creation and annihilation of shear planes play a role in the oxidation of propene.[99] Crystallographic shear planes are also observed in materials like $WO_3$ and $TiO_2$.[100] In $WO_{3-x}$, Ingham et al.[101] have reported that the Fermi level moves towards the conduction band as x increases and for x= 0.2, the Fermi level coincides with the conduction band corresponding to a β-γ phase transition ($W_{20}O_{58}$ to $W_{18}O_{59}$ transition).

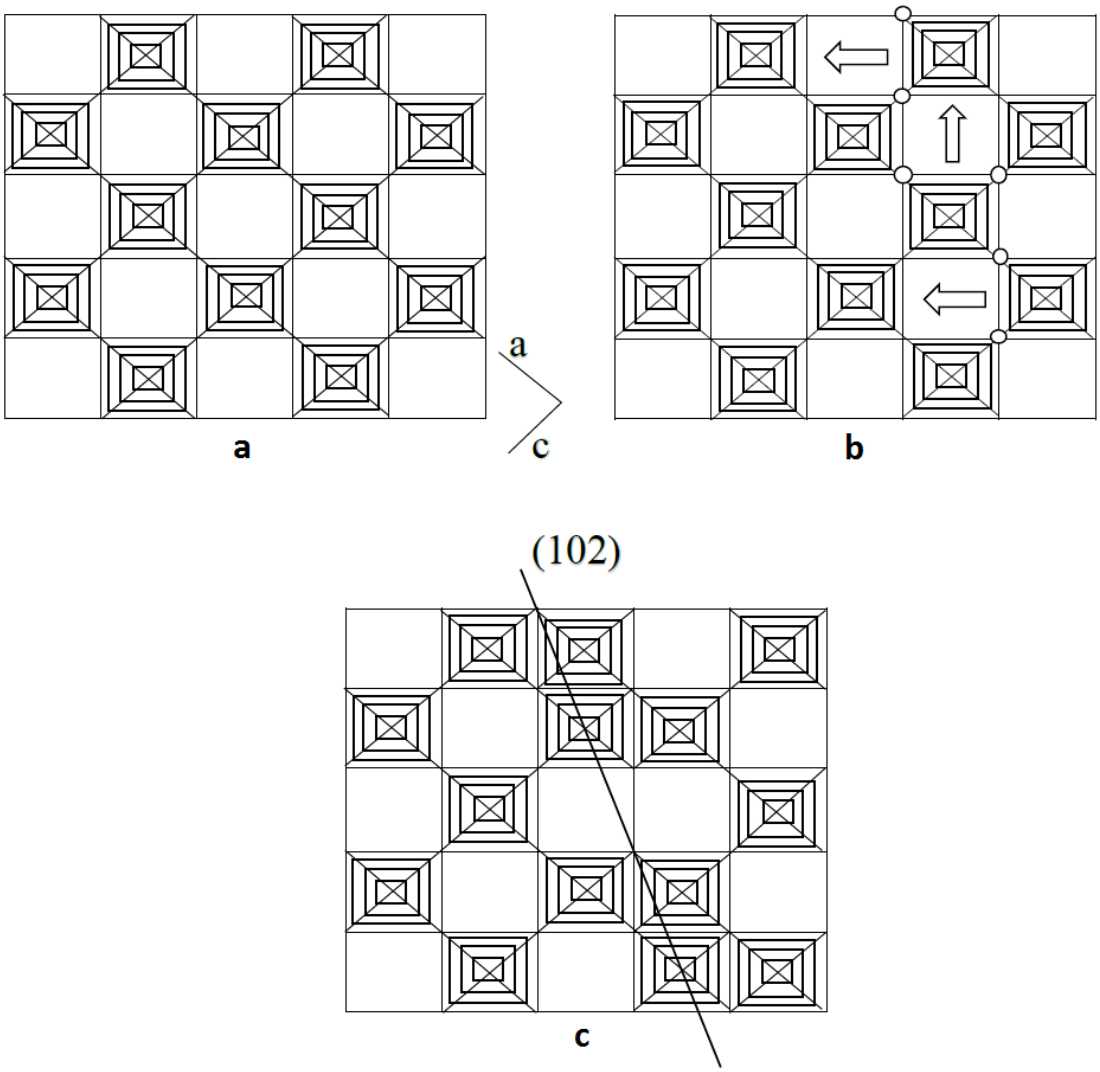


**Figure 2.10**. Formation of crystallographic shear planes (a) $WO_3$ structure consisting of corner shared $WO_6$ octahedra. (b) In slightly reducing atmosphere, oxygen vacancies are formed which migrate to certain planes in the structure. The vacancies are eliminated as the octahedra collapse into the neighboring vacant sites (as shown by arrows). (c) Formation of (102) shear planes whereby the structure changes from corner sharing to edge sharing along the plane [Adapted from [97]].

#### 2.3.3.1.3 Line defects

Line defects are formed when subjected to certain strains where the crystals can deform, by a process called slip, where one part of the crystal lattice is translated relative to the adjacent part.[97] Dislocations are considered as line defects in which a plane of atoms stops within the crystal producing a line of dangling bonds.[97] The two dislocations observed in crystals are edge dislocations and screw dislocations. Edge dislocations are formed due to the insertion of an extra atomic plane due to applied stress in the crystal. Figure 2.11 shows the schematic of an edge dislocation in a simple cubic lattice. Slip plane is the plane along which dislocations are formed. When a stress is applied to an edge dislocation, it causes the dislocation to move along the same slip plane (dislocation glide) or move up into a different slip plane (dislocation climb). These mechanisms are important at high temperatures where atomic diffusion takes place.[97] The dislocation core plays an important role in diffusion and will be discussed later in the section.

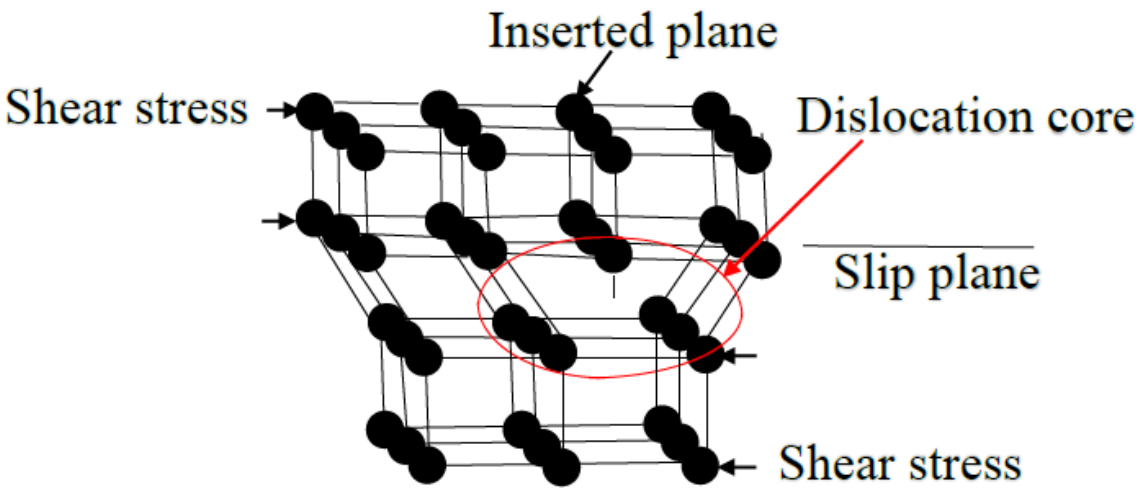


**Figure 2.11**. Edge dislocation in a simple cubic lattice.

The second type of dislocations are called screw dislocations. In this case defect movement is perpendicular to the direction of applied stress as opposed to edge dislocations where the movement is parallel to the applied stress.[102] Figure 2.12 shows the schematic of a screw dislocation along with the position of the atoms. When a stress is applied across one end of a crystal, it will begin to tear off as shown in figure 2.12 (a). The atoms shown in blue in figure 2.12 (b) are still in its original position, while the red atoms have already moved out into their new position and have formed bonds. The green atoms are out of their initial position and about to move into their new positions. If more stress is applied, the green atoms will move into their new positions and form bonds to become red atoms while the blue atoms will move out to become green atoms. Thus the dislocation moves in a direction perpendicular to the applied stress.[102]

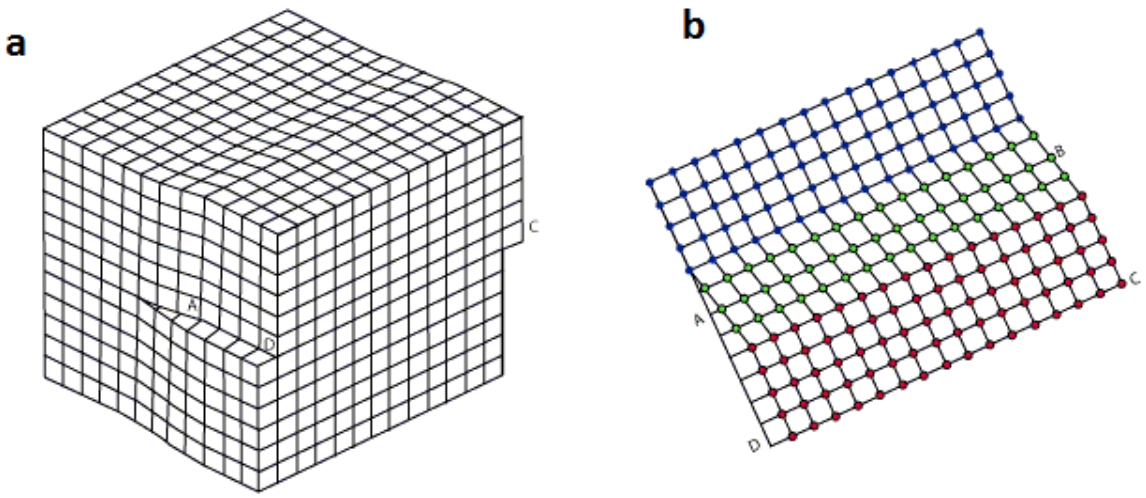


**Figure 2.12**. (a) Screw dislocation due to applied stress; (b) atomic arrangement of the crystal due to applied stress.[102]

Also line dislocations within a crystal can align themselves to form low angle sub grain boundaries. This network of line dislocation arrays produces a small difference in the orientation

of the crystal on either side due to angular distortion. Diffusion of atoms takes place along the diffusion lines of these low angle grain boundaries.[103-104]

Diffusion effects in crystals are due to edge and screw dislocations as well as low angle sub grain boundary diffusion. One possible explanation for diffusion through dislocations have been explained by Hoffman and Turnbull.[105] They postulated that there was a marked segregation of vacancies close to the edge dislocations and this segregation resulted in vacancy sites.[104] Since atomic diffusion consists of jumps along lattice vacancy sites, the vacancy sites along the edge dislocations are also available for atoms with sufficient energy to make diffusion jumps. They also believed that any strained lattice region would accelerate the diffusion process. Love et al.[106] have also observed that diffusion along edge dislocations is significantly higher than that in screw. Another alternate route for diffusion was proposed by Love[104], where he reported that rapid diffusion can take place through the dislocation core (shown in figure 2.11). The dislocation core tends to have interstitials and vacancies, and diffusion occurs due to the net motion of vacancy-interstitial pairs between creation and annihilation (vacancies can combine with interstitials while another vacancy and interstitial is created simultaneously with it).[104]

### 2.3.3.2 Defect Diffusion along Grain Boundaries

Of all the diffusion mechanisms in polycrystalline films, grain boundary diffusion has received the most attention due to the presence of small grains and large density of boundaries.[107] Grain boundaries exist in polycrystalline materials due to planar defects in the grain contact area arising from crystallographic misalignment.[108] For ease of understanding, figure 2.13 shows a highly idealized polycrystalline film with square grains and grain boundaries.

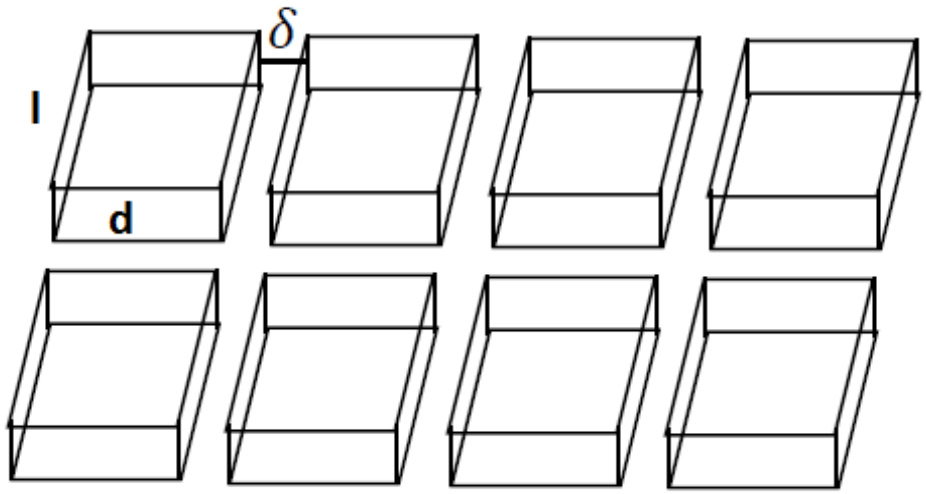


**Figure 2.13**. Idealized polycrystalline film with square grains and grain boundaries.

Here δ is the width of the grain boundary which is several angstroms thick, d is the thickness of the grain and l is the length of the grain. The number of vacancies that flows per unit time through the grain boundary is proportional to the grain boundary diffusion coefficient and the concentration gradient of the diffusant. Balluffi, in his work, has mentioned that vacancies could be formed more easily in the grain boundaries than in the lattice and that the vacancies in the boundary could execute jumps to various sites more easily.[109]

Several researchers[44-47] have tried to study grain boundary diffusion and the first one to develop a grain boundary diffusion model was Fischer in 1951.[44] He observed that the rate of diffusion in polycrystalline films was higher than that of single crystals at low temperatures and

that the logarithm of concentration of the diffusant varied linearly with penetration depth. This was supported by Whipple in his work.[45] Whipple's mathematical expression for diffusion was based on a constant source model applicable to a semi-infinite medium and the validity of these models were only applicable at low temperatures.[46] However Suzuoka observed that the logarithm of concentration of diffusant was proportional to the 6/5 power of penetration depth using an instantaneous source model also for a semi-infinite medium.[46] Expression for diffusion coefficient (which determines the rate at which concentration of diffusant changes along the grain boundaries) for grain boundary diffusion using Suzuoka's model is given by:[107]

$$D_{GB} = -.66\left(\frac{dlnC}{dy^{\frac{6}{5}}}\right)^{-\frac{5}{3}}\left(\frac{4D_L}{t}\right)^{\frac{1}{2}} \quad (2.9)$$

where C is the concentration of diffusant, $D_L$ is the lattice diffusion constant and y is the penetration depth. He also showed mathematically, using a polycrystalline medium consisting of cubic grains of edge 2b, that the contribution of grain boundary diffusion is lowered with increasing grain size, predicting that the average concentration at depth y and time t is

$$C\ (y,t) = \frac{K}{\sqrt{\pi D t}}\left(c1 + \frac{1}{b}c2\right) \quad (2.10)$$

where $K$ is the amount of diffusant per unit area, D is the lattice diffusion coefficient, $c1 = e^{-\frac{\eta^2}{4}}$ is the lattice diffusion expression where $\eta = \frac{y}{\sqrt{Dt}}$ is a dimensionless quantity, $\frac{1}{b}$ is the number of grain boundaries per unit area and $c2 \propto \frac{\pi}{\sqrt{K}}$ is the grain boundary diffusion expression. Having large grain size tends to reduce the number of grain boundaries per unit area and thus overall effect is a reduction in grain boundary diffusion.

Suzuoka[46] observed that at relatively high temperatures (>800 °C), diffusion in polycrystalline silver is similar to that in single crystals. This means that grain boundary

diffusion coefficient and lattice diffusion coefficient are very comparable at very high temperatures, but at lower temperatures grain boundary diffusion effects dominate. It was observed that self-diffusion in polycrystalline silver (Ag), at 936 °C, agrees well with that in single crystals.[46, 110] Figure 2.14, based on Suzuoka's observation, shows a schematic representation of diffusion kinetics in a polycrystalline film containing an array of parallel grain boundaries. At high temperatures, lattice diffusion is also significant such that it is comparable to diffusion through the grain boundary arrays. As temperature reduces, the lattice diffusion effect also reduces and at low temperatures most of the diffusion is through the grain boundaries.

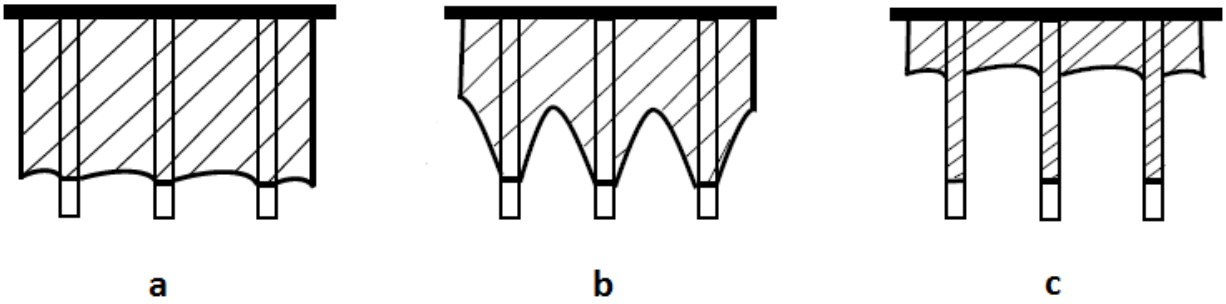


**Figure 2.14**. Schematic representation of diffusion kinetics in polycrystalline films from (a) highest temperature to (c) lowest temperature.

However, Oishi et al.[111] studied oxygen diffusion effects in single crystal and polycrystalline $Al_2O_3$ and observed that oxygen diffusion at high temperatures (greater than 1400 °C) in polycrystalline films are at least two orders of magnitude higher than that in single crystals, as the grain boundary diffusion coefficient was found to be much higher than the lattice diffusion coefficient. These studies do show that grain boundary diffusion is one of the most important mechanisms relating to vacancy diffusion in polycrystalline films under certain conditions. However, neither the Suzuoka model nor the Whipple model for diffusion can be

applied to thin film metal oxides as their mathematical expressions were for a semi-infinite medium. Gilmer and Farrell[49] developed a mathematical expression for grain boundary vacancy diffusion for finite thickness medium and this will be discussed in detail in chapter 3.

This section has detailed the defect diffusion processes. For thin polycrystalline films, vacancy diffusion would be primarily due to grain boundaries. Lattice defects due to vacancies, interstitials, shear planes and dislocations also exists in thin films. The effective diffusion coefficient associated with vacancy diffusion in polycrystalline films would depend on all of these defects and can affect diffusion mechanisms.

## 2.4 Tungsten Trioxide ($WO_3$)

The SMO of interest in this thesis is $WO_3$. Understanding the structural properties of $WO_3$ films, including the film surface, would be useful in understanding $NH_3$ interaction on the $WO_3$ based gas sensors and also help in the subsequent surface reaction and diffusion models. This section details the structural properties of $WO_3$ including the $WO_3$ film surface. Planar and GLAD $WO_3$ film morphology is discussed in chapter 3 and film fabrication is detailed in chapter 4.

### 2.4.1 Structural Properties of $WO_3$

Stable monoclinic $WO_3$ exhibits a rhenium oxide ($ReO_3$)-type structure based on corner sharing of $WO_6$ octahedra with the O atoms at the corner of the octahedron.[112] Figure 2.15 shows a schematic model of the $WO_3$ crystal structure. The symmetry of the $WO_3$ octahedra is lowered by two distortions and they are

- Rotation of $WO_6$ octahedra with respect to each other.[26]
- Displacement of tungsten from the center of the octahedron.[26]

Salje [113] determined that the deviation of $WO_3$ octahedra was characterized by the zig zag motion of W ion along the [011] direction (along b and c as shown in figure 2.15 (b)) along with a tilt with tilt angles around a direction. The octahedra are not strongly distorted, but the tungsten atoms are off-center and the octahedra are rotated to form diamond-shaped cages. During $WO_3$ bronze formation, these cages are occupied by cations like $H^+$, $Li^+$ or $Na^+$ and the tunnels formed by these cages also facilitate rapid diffusion of small cations.[26]

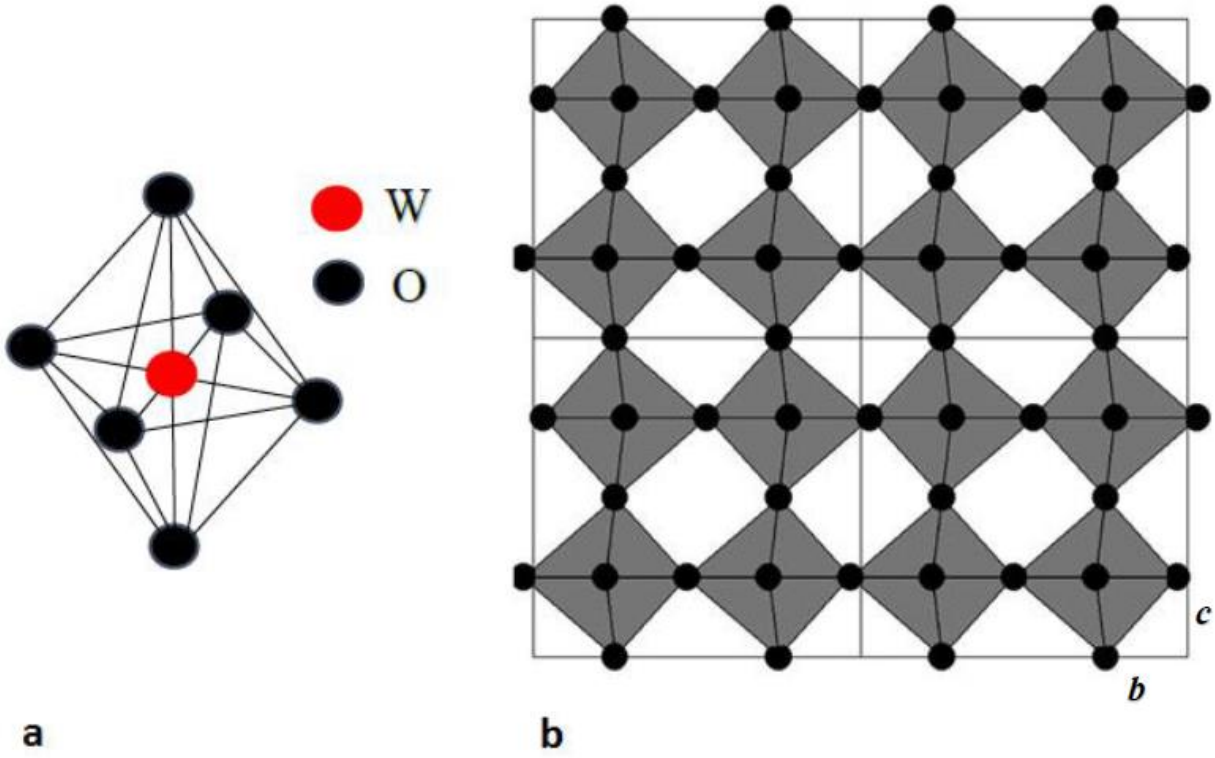


**Figure 2.15**. (a) $WO_6$ octahedra and (b) Distorted $WO_3$ crystal structure along [011] direction.

According to Cora et al.[70] lattice distortion in $WO_3$ due to W ion displacement is driven by covalent interaction with neighboring oxygen ion and these distortions in $WO_3$ symmetry give rise to several phase transitions. $WO_3$ adopts at least five distinct crystallographic modifications between absolute zero and its melting point of 1700 K.[112] As the temperature is increased the crystallographic symmetry for $WO_3$ changes in the sequence: monoclinic-triclinic-monoclinic-

orthorhombic-tetragonal and remains in the tetragonal phase upto the melting point. Table 2.1 shows the summary of these transitions.[114]

**Table 2.1**. Summary of phase transition for $WO_3$.

| **Structure** | **Temperature range (K)** |
|---|---|
| Monoclinic | 0 – 230 |
| Triclinic | 230 – 290 |
| Monoclinic | 290 – 600 |
| Orthorhombic | 600 – 1000 |
| Tetragonal | > 1000 |

Stoichiometric $WO_3$ readily loses oxygen to form $WO_{3-x}$. In slightly reduced $WO_3$, shear planes are introduced in many directions at irregular intervals (Wadsley defects) where $WO_3$ moves from a corner sharing arrangement to an edge sharing arrangement as shown in figure 2.10.[26] As reduction proceeds, the random directions are suppressed and the [1 0 2] direction predominates at irregular intervals (see figure 2.10). Finally, at greater reduction, 1 0 3 planes dominate at regular spacing.[26] These phases containing shear planes with edge sharing $WO_6$ octahedra are called Magneli phases. Typically in sub stoichiometric $WO_3$, $W_{18}O_{49}$ ($WO_{2.72}$) and $W_{20}O_{58}$ ($WO_{2.90}$) Magneli phases are observed.[115] It does not seem likely that shear plane formation would cause any sudden discontinuity in electrical conductivity during oxidation or reduction, since it appears to be a rather continuous process.[26]

Since gas-film interaction takes place on the surface, which is discontinuous, it becomes necessary to examine the geometry of the $WO_3$ surface. Consider the case shown in Figure 2.16.

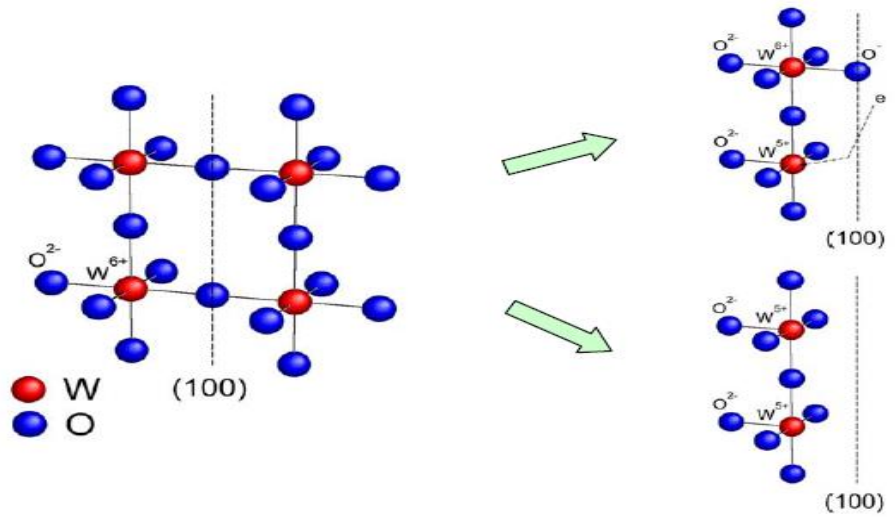


**Figure 2.16**. Structure of a $WO_3$ grain surface with fracture planes (100) is shown (left). Formation of $W^{5+}$ sites in both cases are shown (right).[112]

Kuzmin et al.[116] has proposed that if the crystal is cleaved along the (100) plane as shown in the above figure, two different situations can be considered. In the first case, half of the tungsten atoms remain in the valence state 6+ and are connected to the terminal oxygen ions giving one of their electrons to the nearest tungsten ion which transforms to $W^{5+}$ state. In the second case, all tungsten atoms at the surface change their valence state to 5+. $WO_3$ surface consists of W=O layer[117] possibly due to formation of $W^{5+}O$ terminal layer. The presence of monoxo layer on $WO_3$ surface was also shown by Wachs et al. using Raman spectroscopy that the surface consist W=O sites along with W-O-W sites.[118] Kuzmin et al. also observed that in both cases, the surface $W^{5+}$ sites can react with the oxidizing atmosphere of air to form $W^{6+}$-OH bonds in the presence of humidity.[116] These reduced $W^{5+}$ sites could act as Lewis acid sites where reducing gases like $NH_3$ could adsorb and undergo the surface reaction process. Gallardo[112] has stated that $W^{6+}$-OH sites are typically Brønsted acid sites where $NH_3$ could

potentially adsorb as well. Altman et al.[119] used scanning tunneling microscopy (STM) and TPD to characterize adsorption of alcohols on $WO_3$ (100) single crystal. They observed water desorption at 425 K, formed as a result of alkoxide formation due to de-protonation of alcohol. The alkoxide did not show any particular affinity for defects on the surface but binds to surface tungsten cation sites.

# 3. THEORETICAL MODELS FOR SURFACE REACTION AND BULK DIFFUSION EFFECTS IN METAL OXIDE GAS SENSORS

In this chapter, a theoretical model for the bulk conduction mechanism in both the surface reaction limited and bulk diffusion limited cases is presented for both planar and nanostructured metal oxide film gas sensors. Based on these models, expressions for the magnitude of the change in steady state conductivity of the sensor when exposed to the target gas ($\Delta\sigma$) and response time ($\tau$) of these sensors as a function of various kinetic and geometric parameters are obtained.

## 3.1 Morphology of Planar and GLAD $WO_3$ Films

In order to predict conductivity changes and response times in $WO_3$ films exposed to ppb level concentrations of $NH_3$ gas, one must assume a particular morphology for the thin film. In this section the film morphology associated with both planar and GLAD films is presented.

### 3.1.1 Planar Film Morphology

Polycrystalline planar film morphology varies with film growth conditions such as deposition temperature and annealing temperatures.[120] Figure 3.1 shows an example of the the X-ray Diffraction (XRD) pattern of planar monoclinic $WO_3$ films deposited at 650 °C, room temperature (30 °C) and 200 °C respectively and the appropriate annealement process. The crystallographic axis (a, b and c) are shown in the figure along with the associated film microstructure.

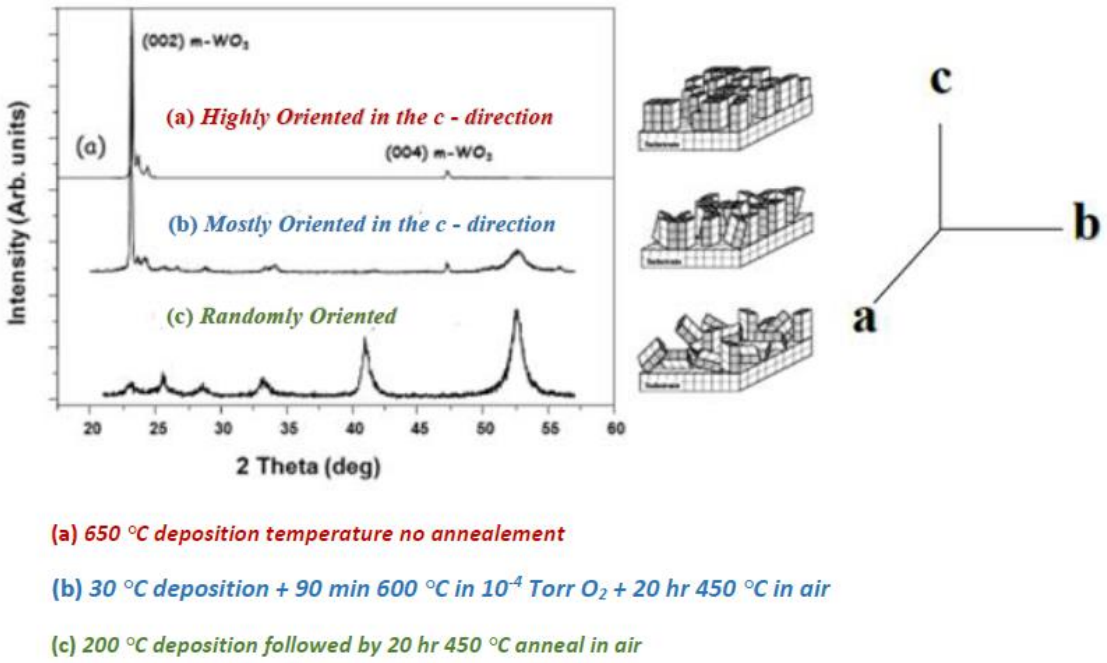


**Figure 3.1.** XRD patterns showing the microstructure of (a) highly oriented (b) mostly oriented and (c) randomly oriented polycrystalline $WO_3$ film for different deposition and annealing temperatures.[120] Models of the orientation of the crystallites with respect to the crystallographic a, b and c axis are also shown.

As shown in figure 3.1, the films deposited at 650 °C are highly oriented in the c-direction whereas the films deposited at room temperature and annealed are mostly oriented along the c-direction with a modest misalignment between the neighboring crystallites.[121] Lastly, for films deposited at 200 °C and annealed, the film morphology consists of randomly oriented crystallites. As expected, the XRD pattern shows that more peaks in randomly oriented polycrystalline films compared to the other polycrystalline film morphologies.

In this thesis, polycrystalline planar $WO_3$ films were deposited at room temperature on an insulating r-cut sapphire substrate using magnetron sputtering and annealed at 500 °C for 6 hours (discussed in chapter 4). Based on the results shown in figure 3.1, the crystallites in these planar

films are likely to be mostly oriented in the c-direction. Figure 3.2 shows a cross sectional schematic in the b c plane of a mostly oriented polycrystalline $WO_3$ film whose crystallites are columnar. An SEM image of the top of the film surface is also shown in the figure.[122] Due to the fact that the crystallites are not all oriented in the c-direction, the film surface is not expected to be flat. The top view shows a dense cauliflower like morphology with no obvious voids between the crystallites (grains).

In order to theoretically predict changes in conductivity and response time an approximation to the structure shown in figure 3.2 is made.

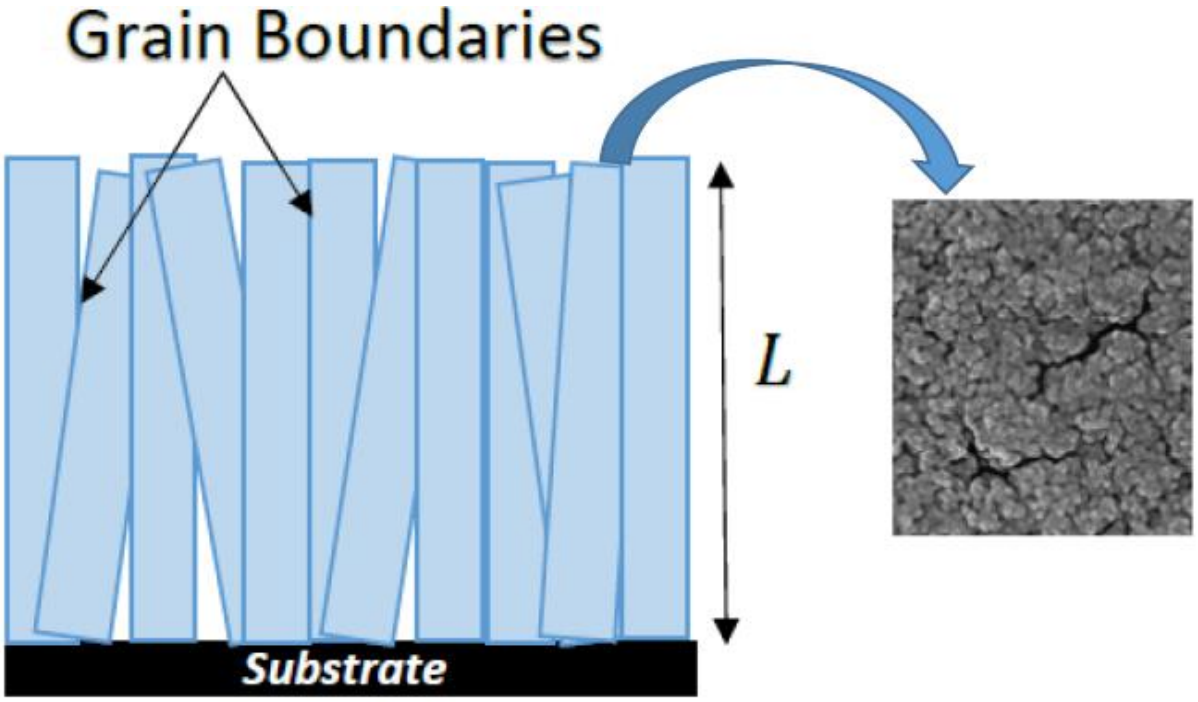


**Figure 3.2.** Cross sectional view of a mostly oriented polycrystalline film with a film thickness L and an SEM image of a $WO_3$ film surface.[122]

In particular, ***the crystallites are assumed to be parallel and of uniform height with a flat surface*** as shown in figure 3.3. The film thickness, *L*, is the distance between the substrate surface and the crystallite surface. ***The boundaries between the crystallites are assumed to be perpendicular to the substrate surface***. ***The top view shows a single crystallite surface which is approximated as having a hexagonal cross section for close packing of the crystallites so as to eliminate any voids on the surface.***

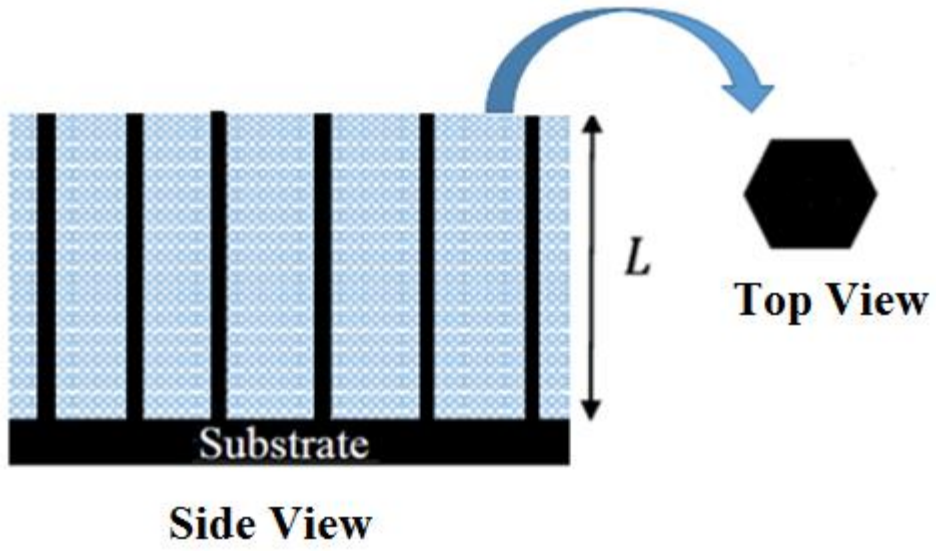


**Figure 3.3.** Side and top view of an approximate structure for a mostly oriented polycrystalline planar film.

### 3.1.2 GLAD Film Morphology

The angle between the vapor flux and substrate normal is expected to have an effect on the film morphology. In the case of the planar films, the angle was approximately 17.6° whereas for GLAD films the angle was approximately 80° as shown in figure 3.4.

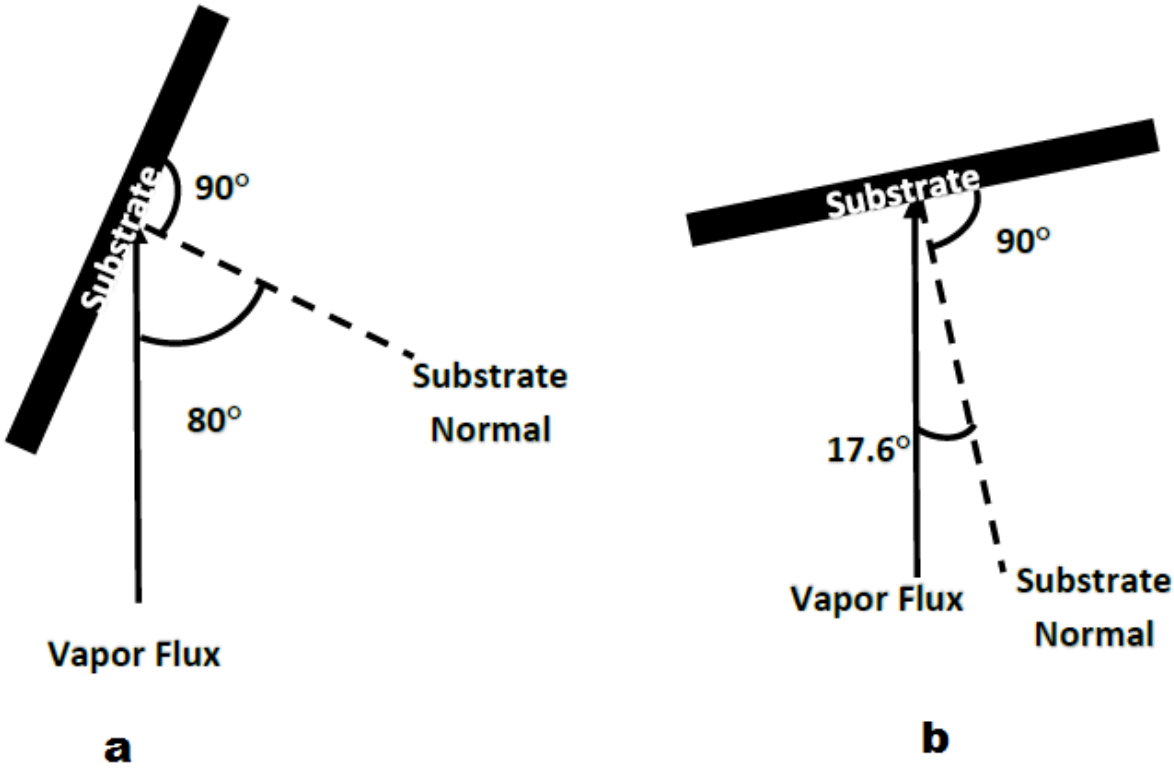


**Figure 3.4.** Angle between vapor flux direction and the substrate normal for (a) GLAD and (b) planar films.

Due to the fact that the angle between the vapor flux and the substrate surface is only 10° for GLAD films, the vapor flux will not reach certain regions of the substrate (atomic shadowing effects). This combined with the low surface mobility of adatoms (incident atoms from the vapor flux which are adsorbed on the substrate surface) results in the growth of certain grains to form well-spaced (voids) columnar microstructures/nanorods[52, 123] as shown in figure 3.5 a. The grains that do not form columnar nanorods, due to atomic shadowing effects, nucleate on the surface to form a thin polycrystalline base layer. The nanorods are widely spaced single *crystalline grains*, which may have a large number of defects (oxygen vacancies, oxygen interstitials) in the nanostructures. Figure 3.5 b shows the cross sectional scanning electron microscope (SEM)

image of $WO_3$ GLAD films grown by magnetron sputtering in which a slight tilt in the grains along with voids are observed.

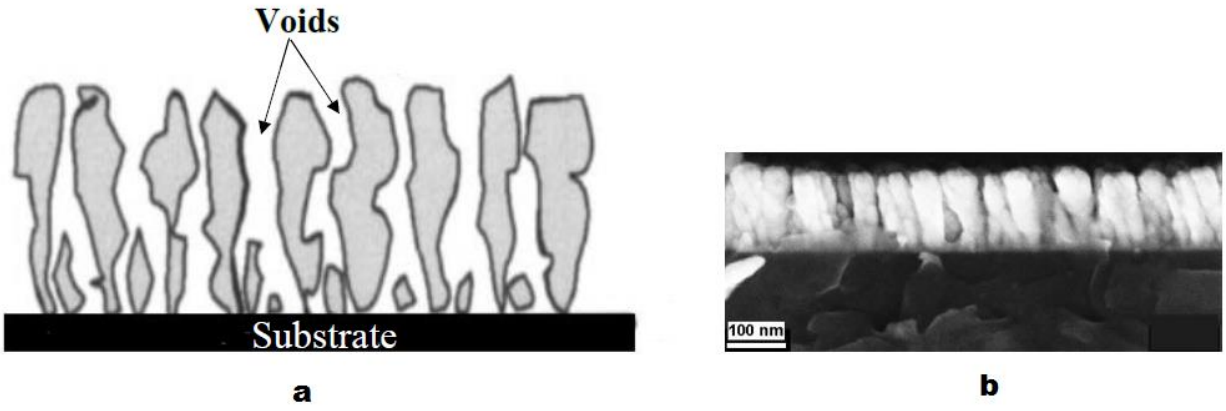


**Figure 3.5.** Nanorod morphology of the GLAD film is shown using (a) a schematic of the cross sectional view of a GLAD film and (b) cross sectional SEM image of $WO_3$ GLAD film.[52]

The adatom mobility characteristics of the material and deposition conditions determine the height of the isolated grain columns/nanorods. Moreover, the diameter of the nanorods is shown to slowly increase with the nanorod height with the top of the nanorod having larger diameter than the bottom.[124-126] This is due to atomic diffusion, which leads to lateral growth of the nanorods over the duration of the deposition.[126] Further details on the fabrication of both these films will be provided in chapter 4.

In order to theoretically predict changes in conductivity and response time, the well spread cylindrical structures on a thin polycrystalline layer shown in figure 3.6 is used as an approximation for the GLAD film.

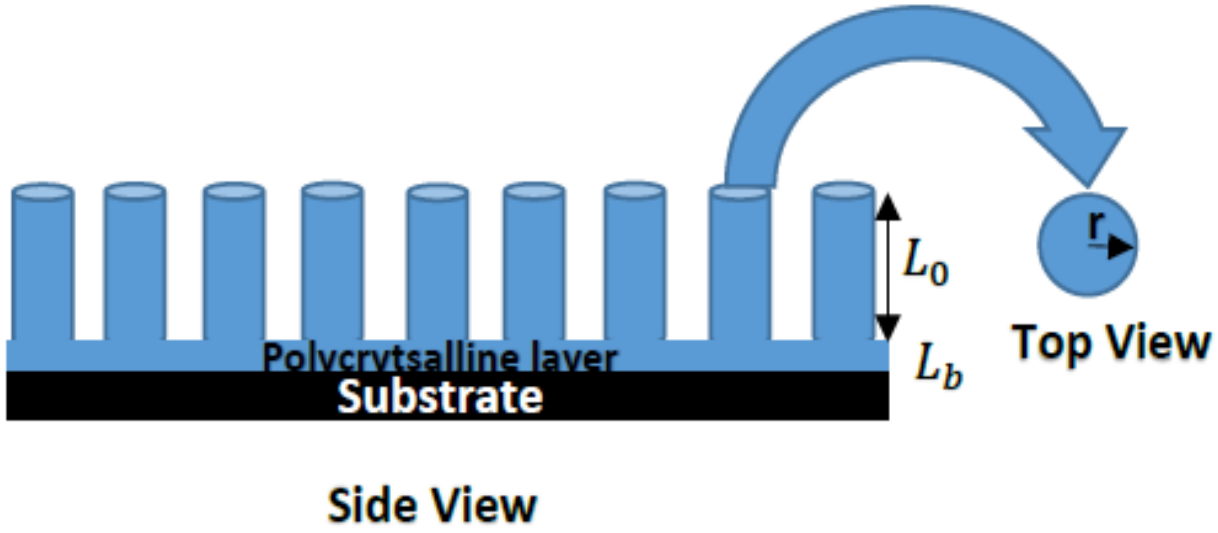


**Figure 3.6.** Side and top view of an approximate structural model for a GLAD film. $L_o$ is the nanorod height, $r$ is the nanorod radius and $L_b$ is the thickness of the base polycrystalline layer.

### 3.2 Conductivity of Planar and GLAD Films

The conductivity of the planar and GLAD film depends on the electrode geometry. SMO films are poor semiconductors, which results in a very high resistance when only two electrodes are used. Therefore, an electrode geometry which can lower the resistance to a range that can be measured more accurately is needed. An interdigitated transducer (IDT) platinum (Pt) electrode is used to lower the film resistance. In the fabrication process, a Pt IDT is deposited on an insulating r-cut sapphire substrate followed by the deposition of the thin film. A Pt IDT was chosen instead of gold due to the high melting point of Pt. Figure 3.7 a shows the top view of the thin planar metal oxide film sensor. Figure 3.7 b shows the side view depicting two adjacent IDT fingers and the film. Each finger of the Pt IDT has a width of about 0.3 mm and a thickness of approximately 3000 Å. The separation ($X$) between the adjacent fingers of the IDT is approximately 0.3 mm. $L$ is the film thickness (250 nm and 125 nm planar films were used in this thesis). The film width,$w$, is approximately 3.0 mm. Figure 3.7 b shows a rough side view

between adjacent IDT fingers in the sensor. Since the conductivity, $\sigma_p$, occurs mainly through the film deposited on the substrate, it can be approximated as follows

$$\sigma_p = \frac{X}{wLR} \tag{3.1}$$

where $R$ is the film resistance between the adjacent IDTs and $wL$ is the cross sectional area of the film. Since the IDTs of the thin film sensor have 6 such conduction paths, as shown in figure 3.7 a, the measured film resistance will be only $\frac{1}{6}th$ of the actual film resistance measured when using only 2 electrodes.

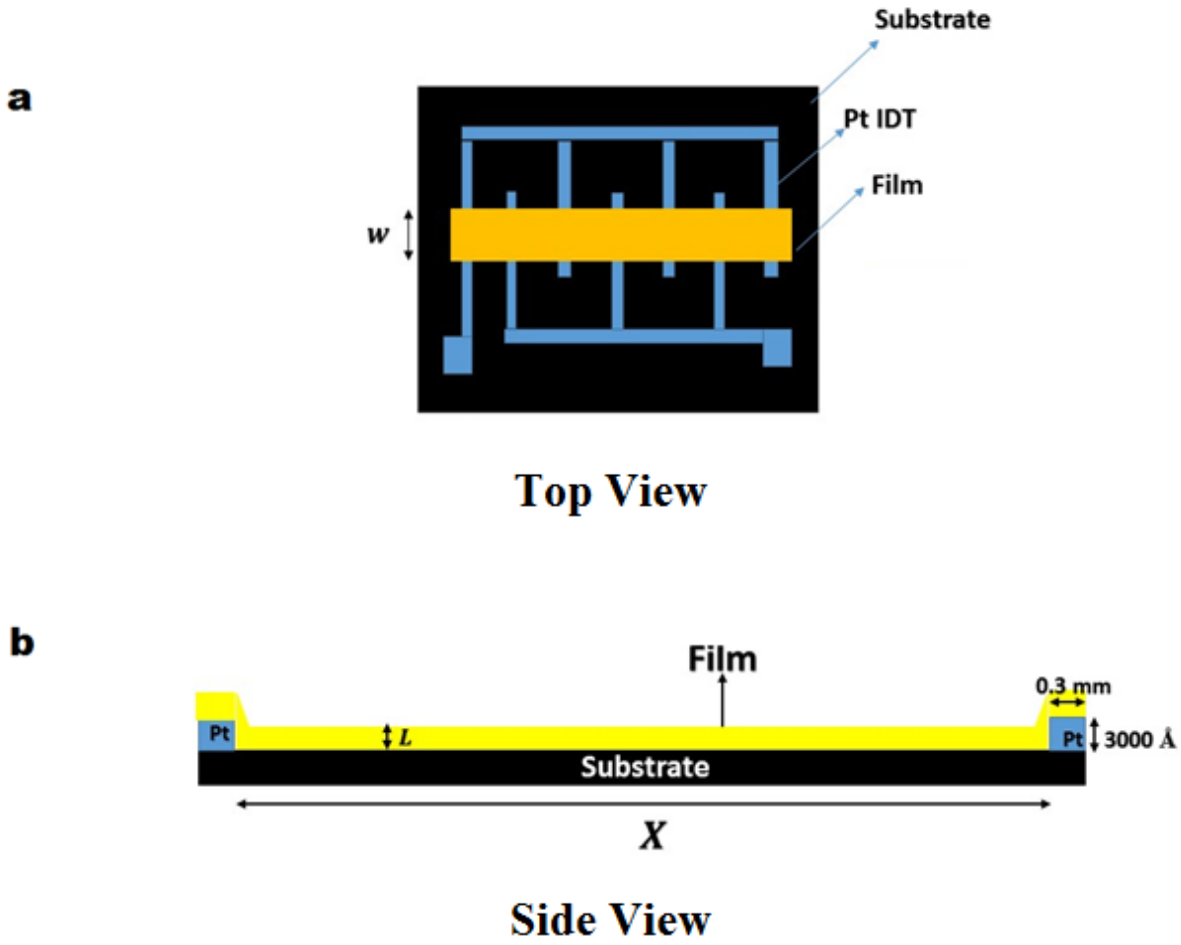


**Figure 3.7.** An illustration of a thin planar metal oxide film sensor (a) Top view and (b) Side view.

### 3.3 Volume to Surface Area Ratio of Planar and GLAD films.

Volume to surface area ratio is an important factor in determining sensor response time. Referring to figure 3.7, the cross sectional film area, $A_c$, the film volume, $V_{planar}$, and the film surface area, $A_{planar}$, between adjacent electrodes are the following

$$A_c = wL. \tag{3.2 a}$$

and

$$V_{planar} = wLX. \quad (3.2\ b)$$

and

$$A_{planar} = wX. \quad (3.2\ c)$$

It is then seen that the volume ($V_{planar}$) to surface area ($A_{planar}$) is given by

$$\frac{V_{planar}}{A_{planar}} = \frac{wLX}{wX} = L. \quad (3.3)$$

Equation 3.3 only depends only on film thickness, $L$.

Calculation of volume to surface area ratio in the GLAD film shown in figure 3.8 is slightly more complicated.

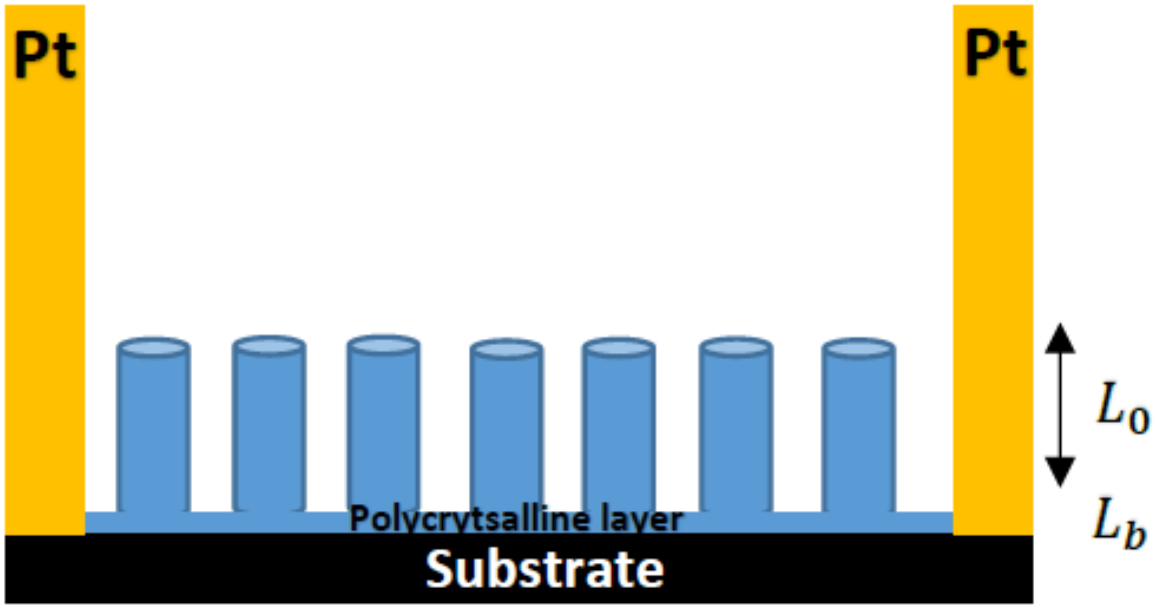


**Figure 3.8.** Schematic of the cross sectional view of the GLAD film between two adjacent Pt IDT fingers. Nanorod height,$L_o$, and polycrystalline base layer thickness, $L_b$, are also indicated.

In this case, the volume of the GLAD film, $V_{glad}$, is the sum of the volume of all the cylindrical nanorods between the adjacent IDTs and the volume of the polycrystalline base layer. The total number of rods, $N_{rod}$, depends on the size and spacing of the nanorods. Total surface area of the GLAD film, $A_{glad}$ is the sum of the surface area of each nanorod and the exposed surface area of the polycrystalline layer. The exposed surface area of the polycrystalline layer, where the sum of the circular base area of each cylindrical nanorod must be subtracted from the total surface area of the polycrystalline base layer. Referring to figure 3.8 it may be shown that the volume to surface area of the GLAD film is as follows.

$$\frac{V_{glad}}{A_{glad}} = \frac{wXL_b + N_{rod}\pi r^2 L_0}{wX + N_{rod}2\pi r L_0} \tag{3.4}$$

From the SEM images shown in figure 3.5 b, for nanorods of diameter 20 nm and spacing of 50 nm and a polycrystalline layer thickness of 10 nm, $\frac{V}{A} \sim 9\ nm$. Since the $\frac{V}{A}$ of planar films is the film thickness, and for a 250 nm planar film, $\frac{V}{A} \sim 250\ nm$ which is much bigger than the GLAD film.

### 3.4 Surface Reaction and Bulk Diffusion Rates

This section reports on the two limiting cases, where the sensor response is either limited by (i) surface reaction rates or (ii) bulk vacancy diffusion rates.

#### 3.4.1 Surface Reaction Rates

Equations (1.7) and (1.8) in chapter 1 shows surface reaction on a metal oxide film when exposed to reducing and oxidizing gases respectively. These, however, are not balanced reactions of any specific gas film surface interaction but mere expressions to introduce the reader to the concept of vacancy creation and elimination on the film surface. In equation (1.7), a

molecule or atom of the reducing target gas, A, reacts with an $O^{2-}$ ion on the surface, to form an atom or molecule of the reaction product, B, a surface oxygen vacancy, $V_o$, along with free electrons. Similarly, in equation (1.8), a molecule or atom of the oxidizing target gas, $RO_2$, reacts with a surface oxygen vacancy, $V_o$, consuming free electrons in the process to form reaction product, RO, along with a surface $O^{2-}$ ion. Using expressions similar to (1.7) and (1.8), rate equations can be written for specific gas interactions with metal oxide film sensors.

Consider the metal oxide film interaction with an oxidation gas like oxygen ($O_2$), since most metal oxide films are exposed to air at elevated temperatures. The equation is similar to that shown in equation (1.8) and is given by the balanced reaction given below,

$$\frac{1}{2}O_2 + V_o + 2e^- \rightleftharpoons_{k_2}^{k_1} O^{2-} \tag{3.5}$$

The expression shown in equation (3.5) is a reversible reaction with $k_1$ being the rate constant associated with oxidation of the film surface and $k_2$ being the rate constant associated with reduction of the film surface in air. Consider the forward reaction and as per rate laws discussed briefly in chapter 2, rate of oxidation of the film surface in air ($r_{ox}^{air}$) is the product of the oxidation rate constant, $k_1$, and the concentration of the reactants, which in this case are oxygen gas and surface vacancies. Change in surface oxygen vacancies would also affect the concentration of surface lattice oxygen species as well. At this point, two terms would be introduced to express the concentration of surface oxygen vacancies and surface lattice oxygen ions on a unit area of the film surface. Concentration of surface lattice oxygen vacancies per unit area of the film surface is expressed using the term $N_V$ (surface vacancy coverage) and the total number of surface lattice oxygen ions per unit area of the surface is expressed using the term $N_{ml}$. Here $N_{ml}$ is also the concentration of surface lattice oxygen sites available for gas reactions

on an ideal film surface (without vacancies) of unit area. But since vacancies are present on most metal oxide surfaces, the total number of available surface lattice oxygen sites per unit area is given by $(N_{ml} - N_V)$. Thus if $N_V$ changes as result of the reactions, a change in $(N_{ml} - N_V)$ is also observed. Thus using the above expressions, rate of oxidation of the film surface in air $(r_{ox}^{air})$ can be expressed as

$$r_{ox}^{air} = k_1\left(P_{O_2}\right)^a N_V. \tag{3.6}$$

Here $P_{O_2}$ is the partial pressure of oxygen in air and is proportional to molar concentration of oxygen in the air, and $a$ is a value that determines the order of the reaction which needs to be experimentally determined.

Similarly, for the reverse reaction shown in equation (3.5), where surface lattice oxygen combine to form $O_2$ gas, rate of reduction in air, $r_{red}^{air}$, is the product of the reduction rate constant, $k_2$, and the concentration of the reactants, which in this case are surface lattice oxygen ions. Concentration of surface lattice oxygen ions is given by $(N_{ml} - N_V)$ and the rate of reduction in air, $r_{red}^{air}$, can be written as

$$r_{red}^{air} = k_2(N_{ml} - N_V). \tag{3.7}$$

The value of $k_2$ depends on the reducibility of the metal oxide film. When a metal oxide film is exposed to air, the baseline conductivity (steady state conductivity in air), $\sigma_{air}$, is determined by equations (3.6) and (3.7), as these equations determine the concentration of surface oxygen vacancies (each vacancy is associated with 2 electrons as mentioned in chapter 1) which can then then diffuse into the bulk of the film.

Now consider the case where the metal oxide film is exposed to a reducing target gas (no air) $T_{gas}$, as shown in equation (1.7). The reducing gas reacts with the surface lattice oxygen ions to form reaction products along with surface oxygen vacancies and free electrons. Equation (1.7) can be written as shown below,

$$T_{gas} + O^{2-} \underset{k_3}{\rightarrow} P_{gas} + V_o + 2\,e^- \tag{3.8}$$

$k_3$ is the reduction rate constant associated with reduction of the metal oxide surface in the presence of a reducing target gas . In this case, the rate of reduction of the film surface due to reducing gas, $r_{red}^t$ , is the product of the reduction rate constant in the presence of $T_{gas}$, $k_3$, and the concentration of the reactants, which in this case are concentration of $T_{gas}$ and surface lattice oxygen ions $(N_{ml} - N_V)$. If $P_t$ is the partial pressure of target gas, then rate of reduction of the film surface in target gas, $r_{red}^t$, is given by

$$r_{red}^t = k_3 (P_t)^b (N_{ml} - N_V) \tag{3.9}$$

where b is the order of the reaction and is experimentally determined.

When a metal oxide film is exposed to target gas in air $(O_2)$, then the change in the number of oxygen vacancy sites per unit area, $N_V$, per unit time due to surface reaction is obtained using (3.6), (3.7) and (3.9)

$$\frac{dN_V}{dt} = -k_1 P_{O_2}^a N_V + k_2 (N_{ml} - N_V) + k_3 (N_{ml} - N_V) P_t^b. \tag{3.10}$$

The negative sign indicates that vacancies are being removed from the surface while in the positive signs indicate that vacancies are formed on the film surface. Thus when the metal oxide film is exposed to a reducing target gas in $O_2$, the final steady state conductivity, $\sigma_{target}$, is dependent on equation 3.10. However, if the metal oxide film is exposed to an oxidation agent

with partial pressure,$P_{ox}$, the steady state conductivity in the presence of $P_{ox}$ in air, $\sigma_{oxidation}$, would be a different expression from that given in equation 3.8, even though it depends on the same parameters like rate constants, $P_{O_2}$ and $P_{ox}$. For a n-type metal oxide film, where the majority carriers are electrons, and reduction of the surface results in creation of bulk vacancies (surface vacancies can diffuse into the bulk), the sensor responds with an increase in conductivity (more free electrons due to vacancies) while for a surface oxidation case, the vacancies are consumed and as a result the conductivity of the sensor decreases. In this thesis, the focus was on developing equations for surface reactions associated with reducing gases.

### 3.4.2 Bulk Vacancy Diffusion Rates

For the case when bulk vacancy diffusion rates limit the sensor response, steady state conductivity changes are still dependent on the surface reaction kinetics, however, the response time of the sensor depends on the time taken for the surface vacancies to diffuse into and equilibrate within the bulk of the film. The total number of bulk lattice oxygen vacancies, $[V_{ob}]$, is the total number of lattice oxygen vacancies per unit volume of the film. Expression which relates change in surface vacancy coverage (as a result of surface reaction) to the change in bulk vacancy concentration at the surface is given by Fick's first law of diffusion,

$$\frac{dN_V}{dt} = -D\,\frac{d[V_{ob}]}{dz}_{z=0}. \tag{3.11}$$

where $\frac{dN_V}{dt}$ is the rate of change in surface vacancy flux, $D$ is the diffusion coefficient of the vacancies. Here $z$ indicates the depth of the film and must not be confused with film thickness ($L$) where $z = 0$ is the film surface and $z = L$ is the film substrate interface.

Rate of change of bulk vacancies over film depth, $0 \leq z \leq L$, in the simplest case is given by Fick's 2nd law,

$$\frac{d[V_{ob}]}{dt} = D\,\frac{d^2[V_{ob}]}{dz^2} \quad . \tag{3.12}$$

Here, the boundary condition, $\frac{d[V_{ob}]}{dt}_{z=L} = 0$, is needed, where $L$ is the film thickness. This just shows that there is no bulk vacancy diffusion along the film substrate interface.

### 3.4.3 Combining Surface Reaction and Bulk Diffusion Rates

Combining (3.6), (3.7), (3.9) and (3.11) gives an expression for rate of change of surface vacancies due to both surface reaction and bulk vacancy diffusion as given below.

$$\frac{dN_V}{dt} = -k_1\,P_{O_2}^{a}\,N_V + k_2(N_{ml} - N_V) + k_3(N_{ml} - N_V)\,P_t^{b} - D\,\frac{d[V_{ob}]_{z=0}}{dz}, \tag{3.13}$$

Negative sign shows that vacancies are removed. Equations 3.12 and 3.13 are called as coupled differential equations and must be solved simultaneously so that the final expression for conductivity can therefore be calculated in terms of bulk vacancy concentration. Although numerical solution is possible using finite element methods[50], obtaining general expressions for the steady state change in conductivity and response time in terms of the physical parameters becomes difficult. We therefore examine limiting cases where the response is either surface reaction limited or diffusion limited.

### 3.5. Bulk Conduction Models

Depending on whether the sensor response is limited by surface reaction rates or bulk vacancy diffusion rates, the bulk conduction models can be classified as (1) Surface Reaction Limited or (2) Bulk Vacancy Diffusion Limited models. Surface reaction limited models are discussed first.

#### 3.5.1. Surface Reaction Limited Model

For the surface reaction limited case, bulk diffusion is assumed to be fast, such that the vacancies are uniformly spatially distributed throughout the film so that there is no concentration gradient in the film. Thus equation 3.13 can be approximated to equation 3.10. The rate of vacancy creation on a surface of area $A$ is given by $A\frac{dN_V}{dt}$ and the rate of change in concentration of bulk vacancies for a material of volume $V$ is given by $\frac{d[V_{ob}]}{dt} = \frac{A}{V}\frac{dN_V}{dt}$. Combining this with (3.10),

$$\frac{d[V_{ob}]}{dt} = \frac{A}{V}\left(-k_1\, P_{O_2}^{a}\, N_V + k_2(N_{ml} - N_V) + k_3(N_{ml} - N_V)\, P_t^{b}\right). \tag{3.14}$$

The surface oxygen vacancy coverage can be related to bulk vacancy concentration using a dimensionality conversion between the vacancies per unit area at the surface and the bulk concentration of oxygen vacancies (number per unit volume),

$$N_V = [V_{ob}]^{\frac{2}{3}}. \tag{3.15}$$

For ease of solving the differential equation (3.14) in Mathcad, one needs to convert $[V_{ob}]$ into a dimensionless form. Substituting (3.15) in (3.14), dividing by $N_{ml}$, and making the substitution $\eta = \frac{[V_{ob}]}{N_{ml}^{\frac{3}{2}}}$ , where $\eta$ is a dimensionless vacancy concentration, (3.10) becomes

$$\frac{d\eta}{dt} = \left\{ \frac{1}{N_{ml}^{\frac{1}{2}}} \frac{A}{V} \left( -k_1 P_{O_2}^{a} \eta^{\frac{2}{3}} + k_2 \left(1 - \eta^{\frac{2}{3}}\right) + k_3 \left(1 - \eta^{\frac{2}{3}}\right) P_t^{b} \right) \right\} \tag{3.16}$$

Taking $\kappa_{ox}^{air} = k_1 P_{O_2}^{a}$, $\kappa_{red}^{air} = k_2$, and $\kappa_{red}^{t} = k_3 P_t^{b}$ equation (3.12) can be simplified as

$$\frac{d\eta}{dt} = \left\{ \frac{1}{N_{ml}^{\frac{1}{2}}} \frac{A}{V} \left( -\kappa_{ox} \eta^{\frac{2}{3}} + \kappa_{red} \left(1 - \eta^{\frac{2}{3}}\right) + \kappa_{red}^{t} \left(1 - \eta^{\frac{2}{3}}\right) \right) \right\} \tag{3.17}$$

From the solution of (3.17) for $\eta(t)$, the bulk carrier concentration, $n_C$, is given by

$$n_C = 2\eta \, N_{ml}^{\frac{3}{2}} , \tag{3.18}$$

for doubly ionized oxygen vacancies (each vacancy corresponds to 2 electrons). The steady state bulk vacancy concentration in air, $[V_{ob}]^{air}$, when $P_t = 0$, from (3.17) is:

$$[V_{ob}]^{air} = \left\{ N_{ml} \frac{\kappa_{red}^{air}}{\left(\kappa_{red}^{air} + \kappa_{ox}^{air}\right)} \right\}^{\frac{3}{2}}, \tag{3.19}$$

while in the presence of target gas (along with oxygen) is,

$$[V_{ob}]^{t} = \left\{ N_{ml} \frac{\left(\kappa_{red}^{air} + \kappa_{red}^{t}\right)}{\left(\kappa_{red}^{air} + \kappa_{red}^{t} + \kappa_{ox}^{air}\right)} \right\}^{\frac{3}{2}} . \tag{3.20}$$

The change in conductivity ($\Delta\sigma$) is

$$\Delta\sigma = 2e\mu (N_{ml})^{\frac{3}{2}} \left\{ \left( \frac{\left(\kappa_{red}^{air} + \kappa_{red}^{t}\right)}{\left(\kappa_{red}^{air} + \kappa_{red}^{t} + \kappa_{ox}^{air}\right)} \right)^{\frac{3}{2}} - \left( \frac{\kappa_{red}^{air}}{\left(\kappa_{red}^{air} + \kappa_{ox}^{air}\right)} \right)^{\frac{3}{2}} \right\}, \tag{3.21}$$

which shows that the magnitude of sensor response depends directly on the relative rates of the oxidation and reduction reactions (which vary with temperature and partial pressure), but the

response is independent of the area to volume ratio. The factors $N_{ml}$ and and mobility, $\mu$, are material parameters that depend on crystal structure and electronic band structure.

For the surface reaction limited case, the time dependent sensor response is approximated as a convolution of the time-dependent target gas pressure, $P(t)$, and the sensor step response function, which is obtained experimentally for a step increase in target gas concentration as illustrated in Figure 3.9 (b). The shape of film conductivity (σ) curve, shown in figure 3.9 (a), is a 1- exponential decay, and the sensor response time ($\tau$) can be defined as the time to reach 90% of the final steady state conductivity value.

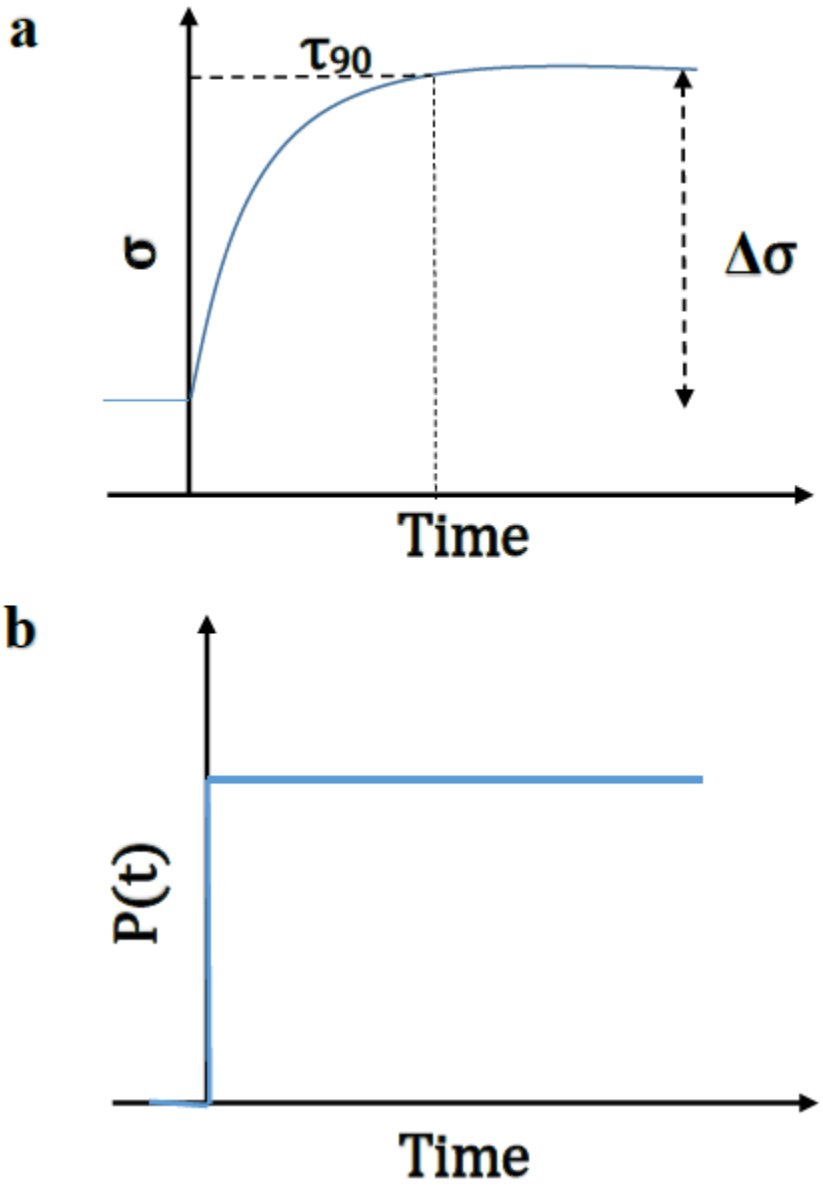


**Figure 3.9.** Illustration of (a) 1- exponential decay behavior of the sensor response with sensor response time well defined for a (b) Step response function of P(t).

### 3.5.1.1. Dependence of Sensitivity and Response Time on Kinetic Parameters

Figure 3.10 (a) shows the dimensionless change in vacancy concentration, $\Delta\eta$, as a function of $K_t$ (parametrized relative to the rate of oxidation in air as $K_t = \frac{k_3 P_t^b}{k_1 P_{O_2}^a} = \frac{\kappa_{red}^t}{\kappa_{ox}^{air}}$) for a wide range of oxide reducibility, $K$ (where $K = \frac{k_2}{k_1 P_{O_2}^a} = \frac{\kappa_{red}^{air}}{\kappa_{ox}^{air}}$). This simplified kinetic model reveals three regimes. When the rate of target gas reaction is less than the intrinsic oxide reduction rate ($K_t < K$; i.e. $\kappa_{red}^t < \kappa_{red}$) the response, $\Delta\eta \sim K_t K^{1/2}$. For constant sensor temperature ($K$ is constant) $\Delta\sigma$ is proportional to $k_3 P_t^b$. Because the value of $K$ increases with temperature the response increases. More reducible oxides (larger $K$) give greater response. The value of $K_t$ typically increases with temperature due to the temperature dependence of $k_3$ but may go through a maximum if the reaction rate becomes adsorption limited (decreasing the surface coverage) or due to thermodynamic limitations if the reaction is exothermic.

In the regime where $K_t > K$ for $K<1$, the response, $\Delta\eta \sim K_t^{3/2}$, and therefore $\Delta\sigma$ is proportional to $P_t^{3b/2}$. The model predicts that the choice of oxide, as represented by its reducibility, would not directly affect response. Increasing temperature generally increases the surface reaction rate, $\kappa_{red}^t$, thereby increasing $\Delta\sigma$. When $K \geq 1$, the oxide will be completely reduced to metal. Therefore, the magnitude of $\Delta\sigma$ is independent of target gas pressure: it is simply the difference between the conductivity of the oxide in air and metal. The material could be used in this regime as a dosimeter, where the time for reduction would depend on both the target gas (via $k_3$) and its partial pressure.

Figure 3.10 (b) shows the response time as a function of $K$ and $K_t$. In the low temperature/pressure regime, where $K_t < K$, and $\Delta\sigma \propto K_t K^{\frac{1}{2}}$, $\tau \sim \frac{K^{\frac{1}{2}}}{\kappa_{ox}}$, independent of target gas

pressure ($K_t$). Since both $\Delta\sigma$ and $\tau$ depend on oxide reducibility as $K^{\frac{1}{2}}$, for sensors operating in the low pressure regime there is a tradeoff between magnitude and speed of response when choosing the oxide and operating temperature for the sensor. For faster detection of toxic gases, in this regime, a less reducible oxide needs to be used. On the other hand, if the objective is to detect low concentration gases for environmental monitoring, where longer response times are acceptable, more reducible oxides can be used to increase $\Delta\sigma$. For the intermediate regime, where $K_t > K$ and $\Delta\sigma \propto K_t^{\frac{3}{2}}$, $\tau \sim \frac{K_t^{\frac{1}{2}}}{\kappa_{ox}}$, which predicts increasing response time with target gas pressure. Both $\Delta\sigma$ and $\tau$ increase with target gas partial pressure. There is still a tradeoff between magnitude and speed of response, but the reducibility of the oxide, $K$, is not a factor in this pressure regime.

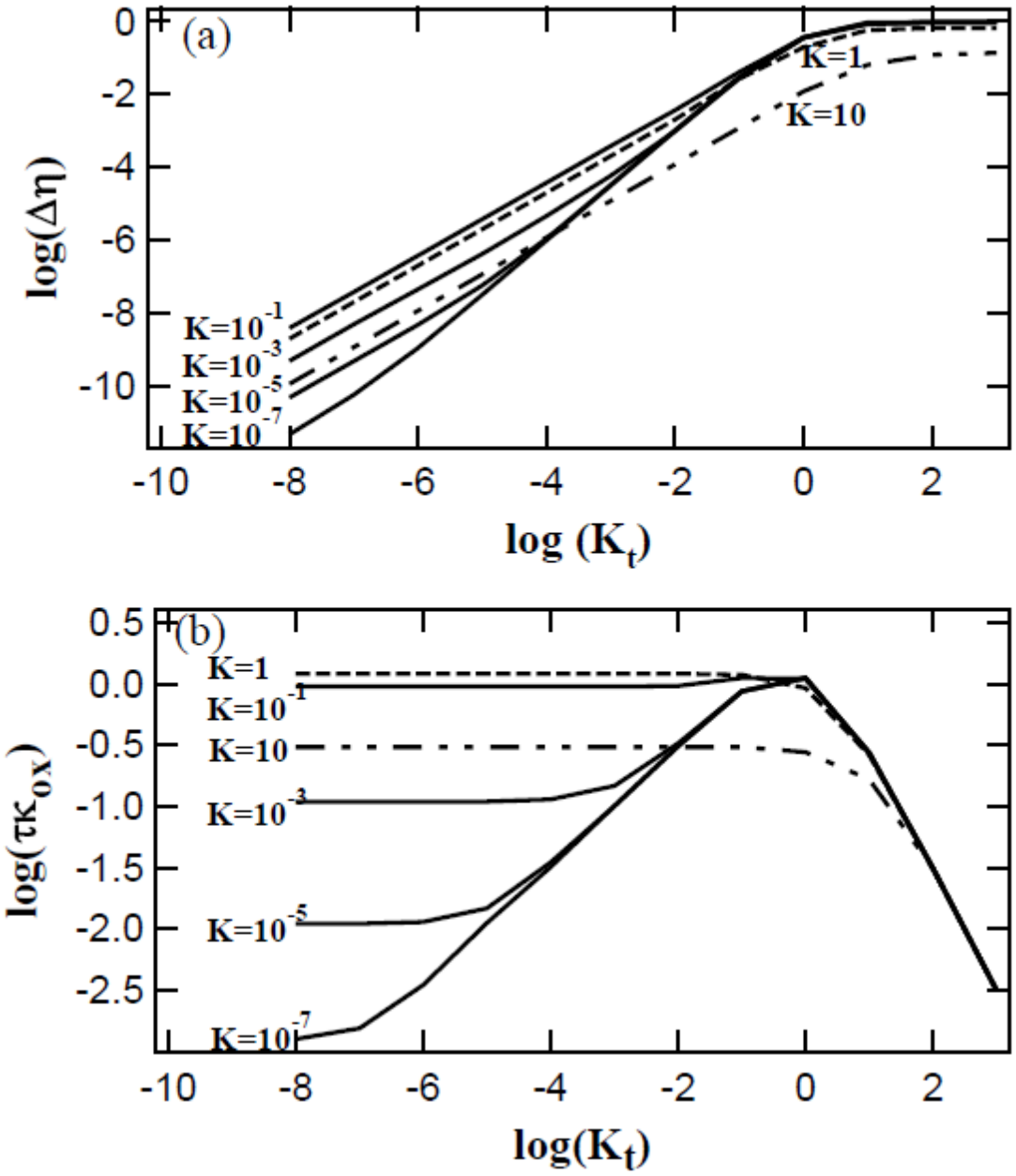


**Figure 3.10.** Illustrating the dependence of **(**a) dimensionless vacancy concentration ($\Delta\eta$) and (b) response time ($\tau$) as a function of target gas pressure for a particular oxide's reducibility. For this case $\frac{V}{A} = 1\ nm$ and $N_{ML} = 1\ \frac{nm^2}{s}$ are taken as constants.

### 3.5.1.2. Overall Response and Response Time

For the surface reaction limited model, as given by equation (3.21), the magnitude of $\Delta\sigma$ does not depend on the $\frac{V}{A}$ ratio. However, equation (3.17) shows that the rate of vacancy creation depends linearly on $\frac{A}{V}$. Therefore, the response time, $\tau$, increase with $\frac{V}{A}$ as it determines how long is required for bulk vacancies to reach steady state concentration. Even though $\Delta\eta \propto \Delta\sigma \propto N_{ML}^{\frac{3}{2}}$ (from equation 3.21) and $\tau \propto N_{ML}^{\frac{1}{2}}$ (from equation 3.17), the number of lattice oxygen sites per unit area typically is of order $10^{15}$/cm$^2$ for most surfaces. $N_{ML}$ may vary somewhat with crystal face and the structure of the metal oxide but $N_{ML}$ is not an adjustable parameter in the model.

The magnitude of response ($\Delta\sigma$) can be determined directly from the graphs of ($\Delta\eta$) for specific kinetic parameters by scaling with $2e\mu N_{ML}^{\frac{3}{2}}$ . From figure 3.10 (a), an expression for log ($\Delta\eta$) in terms of log ($K_t$) can be obtained for the different regimes. Since change in bulk vacancy concentration, $\Delta V_{ob} = N_{ml}^{\frac{3}{2}}\,\Delta\eta\,\left(\frac{1}{nm^3}\right)$ and using (3.19)

$$\Delta\sigma(K, K_t) = 2.0\,(2e\mu)\left(\frac{N_{ML}}{1nm^{-2}}\right)^{\frac{3}{2}}\left(K_t K^{\frac{1}{2}}\right)\left(\frac{1}{\Omega\,nm}\right), for\ K_t < K\ and\ K < 10^{-1} \quad (3.22)$$

while in the intermediate pressure regime,

$$\Delta\sigma(K_t, K) = 2.0\,(2e\mu)\left(\frac{N_{ML}}{1nm^{-2}}\right)^{\frac{3}{2}}(K_t)^{\frac{3}{2}}\left(\frac{1}{\Omega\,nm}\right), for\ K_t > K\ and\ K < 10^{-1} \quad (3.23)$$

From figure 3.10 (b), an expression for log ($\tau\,\kappa_{ox}^{air}$) in terms of log ($K_t$) for the different regimes are given below. In the low pressure regime, where $K_t < K$

$$\tau = 3.44 \left( N_{ML}^{\frac{1}{2}} \frac{V}{A} \right) \frac{K^{\frac{1}{2}}}{\kappa_{ox}^{air}} \text{ (s)} for\ K_t < K\ and\ K < 10^{-1} \quad (3.24)$$

In the intermediate pressure regime, where $K_t > K$

$$\tau = 3.44 \left( N_{ML}^{\frac{1}{2}} \frac{V}{A} \right) \frac{K_t^{\frac{1}{2}}}{\kappa_{ox}^{air}} (s) for\ K_t > K\ and\ K < 10^{-1} \quad (3.25)$$

Solving differential equation (3.17), an approximate solution can be obtained for overall conductivity as a function of time which can be expressed as

$$\sigma(t) = \sigma_{air} + \Delta\sigma\ (1 - \mathrm{e}^{-\mathrm{t}/\tau_{exp}}) \quad (3.26)$$

Where exponential time constant, $\tau_{exp} = \left( N_{ml}^{\frac{1}{2}} \frac{V}{A} \right) \frac{\sqrt{K+K_t}}{\kappa_{ox}(1+K+K_t)^{3/2}}$ (s)

### 3.5.1.3. Temperature Dependence of Surface Reaction Rates

For predicting sensor performance from bulk conduction band model, temperature dependence of surface reaction rates and $\Delta\sigma$ needs to be determined. From $K$ and $K_t$, the response, $\Delta\sigma$, can be determined from figure 3.10 (a) whereas the response time is given by figure 3.10 (b).

The temperature dependence of the rate of vacancy creation (in air) in equations 3.6 and 3.7 is determined by $k_2 = A_2 \exp(-E_{vac}/RT)$, where the vacancy creation activation energy, $E_{vac}$, is the dehydroxylation barrier and $A_2$ is a constant. Thibodeau et al.,[60] found apparent activation energies of 40-120 kJ/mol depending on the sub-stoichiometry of $WO_{3-x}$. The temperature dependence of the oxidation rate is weak, as specified by $k_1 = \frac{s}{\sqrt{2\pi m_{O_2} k_B T}}$, where $s$ is the sticking coefficient, $m_{O_2}$ is the molecular mass of $O_2$, and $k_B$ is Boltzmann's constant. The steady state state solution for the vacancy concentration in air constrains $A_2$ and $s$, given a value for $E_{vac}$.

The $NH_3$ reaction rate constant, $k_3$, in equation 3.9 is an effective rate constant that may in general be controlled by the adsorption rate or the surface reaction rate. The rate constants for adsorption, $k_{ads} = \frac{1}{\sqrt{2\pi m_{NH_3} k_B T}}$, and desorption, $k_{des} = A_{des}\exp(-E_{des}/RT)$,were implemented in a Langmuir adsorption model, where the $NH_3$ coverage was constrained to the monolayer coverage, $N_{ml}$. The $NH_3$ desorption energy, $E_{des}$, depends on the adsorption site. Microcalorimetry data find strongly bound species on $WO_3$ with heats of adsorption, $\Delta H_{ads}$, of 175 and $150\ kJ/mol$, with more weakly bound species at 75 kJ/mol.[127] DFT calculations for $NH_3$ on Lewis acid sites (i.e. surface oxygen vacancies) on $W_9O_{42}$ clusters give $\Delta H_{ads} = 150\ kJ/mol$, while interaction of $NH_3$ with surface terminal hydroxyl groups (i.e. Brønsted acid sites) give $\Delta H_{ads} = 75\ kJ/mol$.[128] The sticking coefficient was taken as $2.6\text{x}10^{-10}$. The surface reaction rate constant, $k_3 = A_3\exp(-E_{rxn}/RT)$ was implemented in a second order process, where the reaction rate, $r_{rxn} = k_3\theta_{NH_3}\theta_O$, depends on both $NH_3$ and lattice oxygen coverage, but for small surface oxygen vacancy coverages, $\theta_O \approx N_{ml}$, and the rate becomes pseudo first order in the $NH_3$ coverage. The values of the kinetic parameters were chosen to match the values of $K$ and $K_t$, based on experimental test data of the $WO_3$ film sensors to ppb concentrations of $NH_3$ gas at 450 °C. The temperature dependence of reaction rates and $\Delta\sigma$, along with sensor optimization details, will be given in chapter 5.

### 3.5.2 Bulk Vacancy Diffusion Limited Model

The surface reaction limited model presented in the previous section was developed under the assumption that the bulk vacancy diffusion process was fast compared to the rate of formation of surface vacancies such that the vacancy concentration gradient in the bulk is negligible. In the diffusion limited case, we assume that the surface reaction is fast, such that

there is a constant flux of vacancies at the surface which can then diffuse into the bulk of the film and the response time of the sensor depends on the diffusion coefficient and geometric parameter like film thickness for compact planar films, nanorod length and radius for nanostructured films.

### 3.5.2.1 Diffusion Model of Planar films

Diffusion of vacancies into planar films, ignoring edge effects, can be described by the 1 dimensional (1-D) solutions given by Crank[129], where

$$\frac{C-C_o}{C_1-C_0}(z,t) = 1 - \left\{\frac{4}{\pi}\sum_{n=0}^{M}\left(\frac{(-1)^n}{(2n+1)}\right)\cos\left(\frac{(2n+1)\pi z}{2L}\right)\, e^{\left(\frac{-D\,(2n+1)^2\pi^2 t}{4L^2}\right)}\right\}, \tag{3.27}$$

is the normalized dimensionless fractional change in vacancy concentration as a function of film depth, z, and time, t, which varies from 0 to 1 as the distribution changes from an initially uniform concentration $C_0$ to a final uniform concentration, $C_1$. $D$ is a homogeneous, concentration independent diffusion coefficient, and $z = L$ is the exposed film surface. Figure 3.11 (a) illustrates the evolution of the normalized fractional change in vacancy concentration, $\frac{C-C_o}{C_1-C_0}(z,t)$ as a function of $z$ for dimensionless time of $0.024\frac{L^2}{D}$. The surface vacancy concentration is greater than the initial bulk concentration due to the reduction reaction. Thus carrier concentration is also higher at the surface (since each vacancy corresponds to 2 electrons), to maintain charge neutrality. The orange curve in figure 3.11 (a) illustrate a later dimensionless time of $0.24\frac{L^2}{D}$, where vacancies have accumulated deeper into the film. Note that the behavior contrasts with the band bending model, which predicts a depletion of charge carriers at the surface, relative to the bulk.

The sensor conductivity is approximated to be proportional to $\bar{\eta}(t)$, the time-dependent dimensionless bulk vacancy concentration averaged over depth, $z$ , where,

$$\bar{\eta}(t) = \frac{\frac{1}{L}\int_0^L \left(\frac{C-C_o}{C_1-C_o}(z,t)\right)dz \times \Delta[V_{ob}] + [V_{ob}]_{air}}{N_{ml}^{\frac{3}{2}}} \tag{3.28}$$

where $\Delta[V_{ob}] = [V_{ob}]^t - [V_{ob}]^{air}$. The time dependence of $\bar{\eta}$ is shown as a function of time in figure 3.11 (b). From the plot, it can be determined that $\bar{\eta}(t)$ reaches 90% of the steady state value in a response time, $\tau = 0.85\frac{L^2}{D}\left(\frac{L^2/nm^2}{D_{eff}/(\frac{nm^2}{s})}\right)(s)$. From this expression, response time is faster in thinner films, but the thickness dependence is one of the significant factors that may distinguish the surface reaction limited case ($\tau \propto L$) from the diffusion limited case, $\tau \propto L^2$. Figure 3.11 (c) presents $ln(\bar{\eta})\ vs.\ ln\left(\frac{Dt}{L^2}\right)$ to show the characteristic $t^{\frac{1}{2}}$ behavior for $t \leq 0.05\frac{L^2}{D}$, after which it approaches saturation. The response time,$\tau$, dependence on the diffusion coefficient ($D$) and film length $L$ is illustrated in figure 3.11 (d). From the plot, $\tau \propto D^{-1}$ and $\tau \propto L^2$.

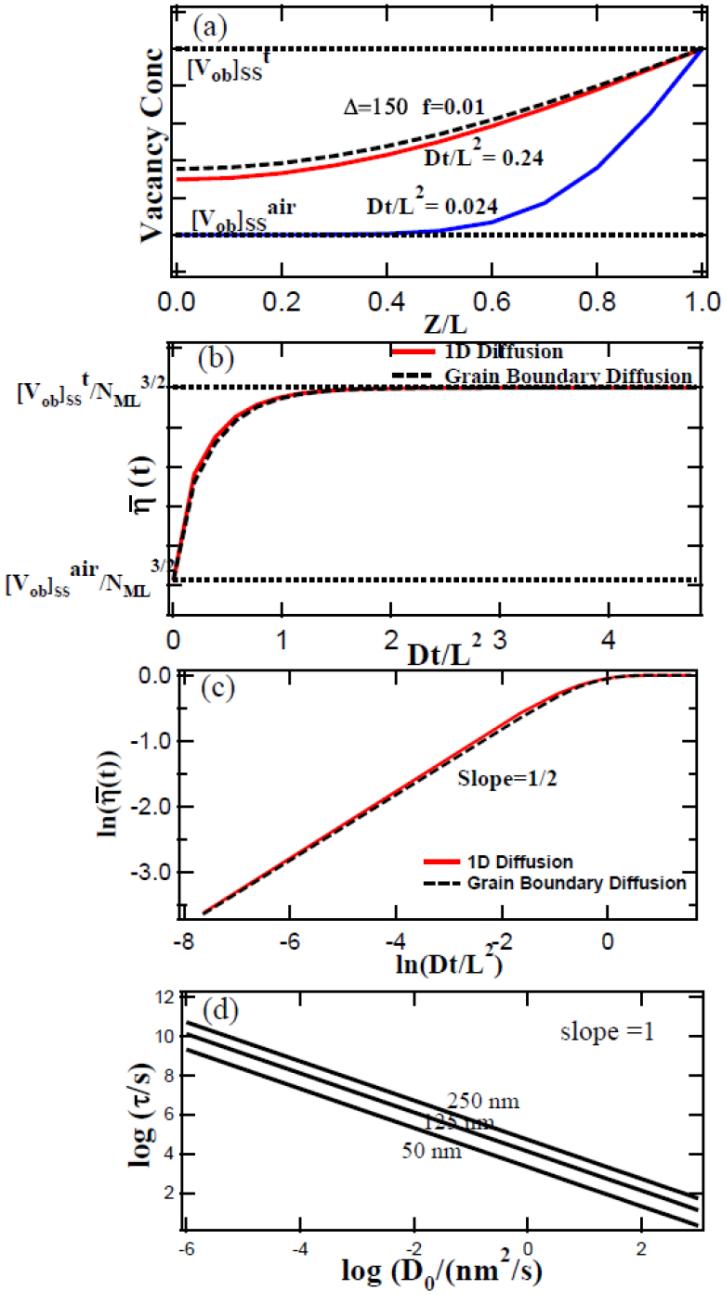


**Figure 3.11.** Illustration of diffusion model of planar films (a) The change in normalized dimensionless fractional change in vacancy concentration as a function of dimensionless depth. (b) Depth averaged bulk vacancy concentration, $\bar{\eta}$, vs. dimensionless time. (c) $t^{\frac{1}{2}}$ dependence of bulk conductivity as a function of time for $t \leq 0.05\frac{L^2}{D}$. (d) Response time dependence on 1-D diffusion coefficient $D$.

### 3.5.2.2 Gilmer-Farrell Model

The effects of grain boundaries in polycrystalline films has not been explicitly considered in sensor modeling. Grain boundaries can affect the response time in polycrystalline film sensors, as vacancies can diffuse more quickly through the grain boundaries than through the lattice. Several attempts[44-47] have been made to model bulk diffusion in different materials and these studies confirms that grain boundary effects can play a role in vacancy diffusion within metal oxide film sensors. However, these models were developed for a semi-infinite medium.

In 1976, Gilmer and Farrell[49] developed a mathematical model based on Whipple's solution for describing the grain boundary and lattice diffusion for finite medium. This approach treats grain boundaries with finite width and finite grain boundary separation running throughout the length of the film, and thus this solution is applicable to polycrystalline metal oxide film sensors. Bulk vacancy diffusion can take place along the grain boundaries as well as along the crystal lattice, and depending on the temperature of operation grain boundaries can be a significant factor in vacancy diffusion. For a finite thickness polycrystalline film, Gilmer and Farrell's mathematical expression for diffusion in finite medium can be used to evaluate the relative influence of grain boundary vs lattice diffusion in thin planar films. A major assumption is that the film surface has a constant concentration of diffusing species, and there is no diffusion parallel to the film/substrate interface (concentration gradient is 0). The expressions for vacancy concentration in the grain boundaries ($C_{gb}(x,z,t)$ and the concentration of vacancies in the lattice ($C_0(z,t)$) are given below:[49]

$$C_{gb}(x,z,t) = \left(\frac{2}{\eta_0}\right)\sum_{n=1}^{\infty}\mu_n \sin(\mu_n\eta)\int_1^{\Delta} e^{-\mu_n^2\sigma} \times erfc\left(\frac{1}{2}\times\left(\frac{\Delta-1}{\Delta-\sigma}\right)^{\frac{1}{2}} \times\left\{\xi+\frac{\sigma-1}{\beta}\right\}\right)d\sigma \quad (3.29)$$

$$C_0(z,t) = 1 - \left\{\frac{4}{\pi}\sum_{n=1}^{\infty}\left((2n-1)^{-1} \times \sin\left(\frac{(2n-1)\pi z}{2L}\right) \times e^{\left\{\frac{-(2n-1)^2\pi^2 D_0 t}{4L^2}\right\}}\right)\right\} \quad (3.30)$$

where $\eta_0 = \frac{L}{\sqrt{Dt}}$, $L$ is the thickness of the film, $D$ is the lattice diffusion coefficient, $\mu_n = \frac{(2n-1)\pi}{2L\sqrt{D_0 t}}$ where n=1,2…∞, $\Delta = \frac{D_{gb}}{D}$ where $D_{gb}$ is the grain boundary diffusion coefficient, $\xi = \frac{x}{\sqrt{Dt}}$ where $x$ is the distance along the grain boundaries, $\eta = \frac{z}{\sqrt{Dt}}$ where $y$ is the diffusion depth and $\beta \sim \frac{1}{\sqrt{t}}$ where $a$ is the width of the grain boundary.

Equation (3.30) is independent of grain boundary separation ($x$) and is similar to equation (3.27). The total concentration of vacancies in the thin film due to both grain boundaries and lattice is given by:

$$C_{gb-film}(x,z,t) = C_{gb}(x,z,t) + C_0(z,t) \quad (3.31)$$

The solutions of equations (3.29)-(3.31) are valid when the distance between the grain boundaries is much greater than $\sqrt{Dt}$. Grain boundaries run throughout the thickness of the film with width, a, as shown in figure 3.3. The grain size is taken as the distance between the center of one grain boundary to the center of next grain boundary. If the width of the collection of grains is taken as $w_{grain}$, then grain width, $w_{gb} = w_{grain} + a$.

The bulk vacancy concentration in the Gilmer Farrell model is similar to that in the 1-D model, in which equation (3.31) is integrated over film depth, $z$, and grain width, $w_{gb}$. The depth averaged bulk vacancy concentration $\overline{\eta_{GF}}(t)$ for a periodic grain boundary array is given by:

$$\overline{\eta_{GF}}(t) = \frac{\int_0^{w_{gb}}\int_0^{L} C_{gf-film}\, dz\, dx}{.5\, w_{gb}\, L} \quad (3.32)$$

The dashed curve in figure 3.11 (a) illustrates a condition revealing the greatest effect of grain boundaries on the depth dependent vacancy concentration using the Gilmer Farrell model in which $\Delta = D_{gb}/D = 150$ and the width of grain boundaries running perpendicular to the surface occupies a fraction, $f = .01$, of the surface area. Despite rapid diffusion through the grain boundaries and subsequent lateral diffusion into the grains, the shape of the depth distributions (figure 3.11 (a)) and depth averaged vacancy concentration vs. time (figure 3.11 (b)) do not differ significantly from the characteristic $t^{\frac{1}{2}}$ dependence expected for diffusion controlled processes. For small values of $\Delta$, the grain effects are minimal and response of the Gilmer Farrell model is similar to the simple 1-D lattice diffusion. Therefore, for the diffusion limited case, the shape of the conductivity vs. time curve should follow the standard solutions to the diffusion equation, whether the diffusivity is due to lattice diffusion or grain boundary diffusion.

Diffusion coefficient vary with operating temperature and in a diffusion limited case, the SMO sensor response time depends on the value of diffusion coefficient. The operating temperature for SMO films is typically between 200 and 500 °C. Temperature dependence of diffusion coefficients for single crystal and polycrystalline oxides are given in Appendix B. Comparison of diffusivities for single crystal with values for the polycrystalline materials illustrates that defect mobility can be dramatically higher in polycrystalline materials. Moreover defect mobility in materials like $WO_3$, compared to less reducible oxides like $SnO_2$, are very high and these mobile defects can migrate to the surface and neutralize surface charge species, making band bending unlikely in reducible oxides. Appendix C compares the dependence of response time, if diffusion limited, as a function of temperature for planar films of $WO_3$ to other oxides. For a $WO_3$ film with D = 300 $nm^2/s$ (figure B1) at 300 °C to achieve a response time of 1s, requires L = 19 nm.

Various authors have developed techniques to introduce an effective diffusion coefficient ($D_{eff}$), which takes into account both grain boundaries and lattice vacancy diffusion effects.[130-132] One important solution for calculating $D_{eff}$ was proposed by Moghadam et al.,[132] where the effective diffusivity is given by:

$$D_{eff} = D_{gb}\left\{1 + \frac{2D(1-f)(1-\Delta)}{D(1+\Delta-(1-f)(1-\Delta))}\right\} \tag{3.33}$$

where $0 \leq f \leq 1$ is the grain boundary area fraction and $\Delta = \frac{D_{gb}}{D} > 1$. Using $D_{eff}$ is an approximate way to include grain boundary effects in diffusion models of more complicated structures like nanorods and templated porous nanostructures.

### 3.5.2.3. Radial Diffusion in Cylindrical Nanostructures

A variety of nanotechnology synthesis methods have been developed to produce cylindrical nanostructures.[126] If gas phase transport to the cylindrical surface is fast, the response time require for radial diffusion into a nanowire of radius is shorter than for bulk diffusion in a planar film whose thickness is equal to the radius of the nanorod and also has the same diffusivity. Solutions to radial diffusion equations are presented to illustrate the characteristic behavior when radial diffusion is limiting the sensor response. In a cylinder, diffusion can, in general, take place along the length of the cylinder as well as radially (figure 3.6). The solution for vacancy diffusion along the length of the cylinder, with no reactions on the cylindrical sides, is similar to the 1-D solution described for the planar film case. Consider a situation where a target gas reacts on the sides of the cylinder and forms surface vacancies. The vacancy flux created at this surface, result in a radial concentration gradient that drives radial diffusion. The

mathematical expression for radial diffusion in a rod of radius, $R$, in terms of Bessel functions, is given by:[129]

$$C_{radial}(r,t) = \frac{2}{R^2}\sum_{m=1}^{M}\left(e^{-D_{eff}\,(\alpha 0_{m-1})^2 t} \times \frac{J0(r\,\alpha 0_{m-1})}{J1^2(\alpha 0_{m-1}\,r_{end})}\int_{r_0}^{R} r f(r) J0(r\alpha 0_{m-1})dr\right) \quad (3.34)$$

where $0 \le r \le R$; $f(r)$ is the concentration distribution within nanorod; $r\alpha 0_{m-1}$ are the roots of $J0(r\alpha 0_{m-1}) = 0$; and $J0(x)$ and $J1(x)$ are Bessels function of the first kind of order 0 and 1, respectively, suitably chosen so that initial and final boundary conditions are satisfied. As for planar films, $C_{radial}(r,t)$ is the normalized vacancy concentration with an initial boundary condition of a unity normalized vacancy concentration at the surface ($r = R$) at $t = 0$. For $t > 0$, the normalized vacancy concentration distribution within the nanorod ($0 < r < R$) is $f(r)$. To compare with the planar film case, the bulk vacancy concentration averaged over nanorod radius , $\overline{\eta_{rad}(t)}$ is calculated by integrating $C_{radial}(r,t)$ over $r$, which is similar to that shown in equation (3.28).

Figure 3.12 shows that, for $R = L$ and for the same diffusion coefficients, radial diffusion is much faster than 1-D planar diffusion for a dimensionless time of $0.24\ \frac{L^2}{D}$. The response time, $\tau = \ 0.4\left(\frac{R^2/nm^2}{D_{eff}/(\frac{nm^2}{s})}\right)\ (s)$. Despite being faster, the shape of the depth distributions do not differ significantly from the characteristic $t^{\frac{1}{2}}$ dependence expected for diffusion controlled processes (similar to figure 3.11 (c)).

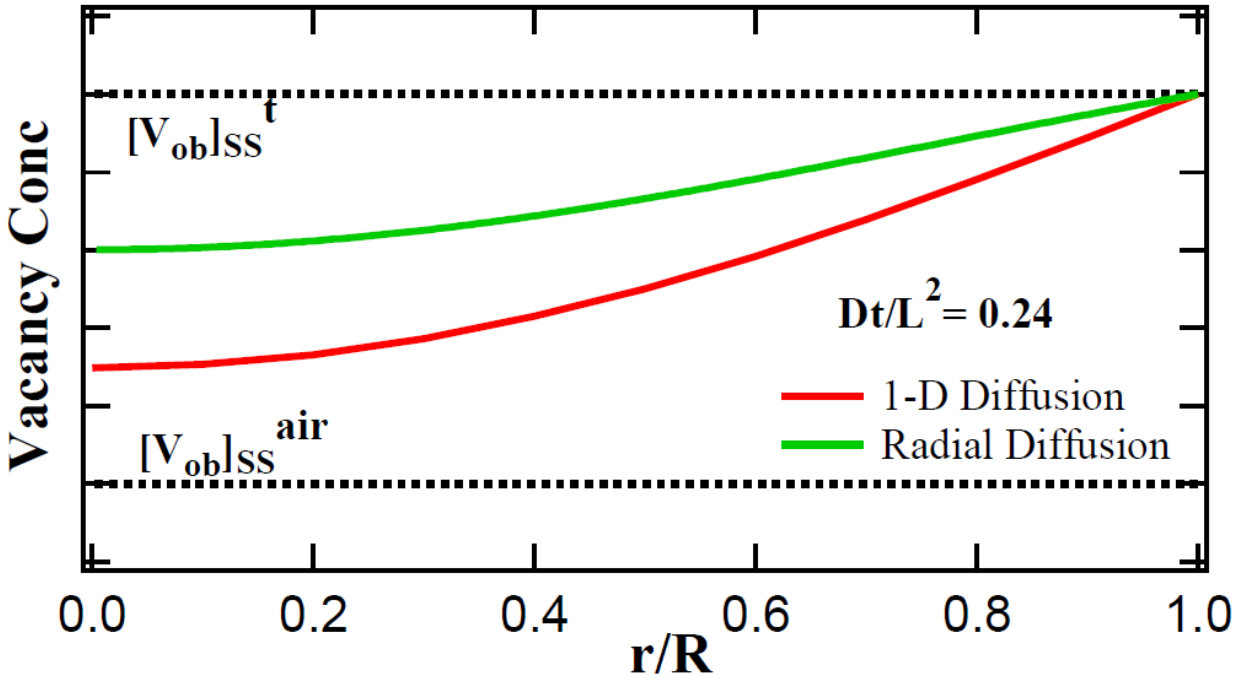


**Figure 3.12.** Change in normalized dimensionless radial vacancy concentration as a function of $\frac{r}{R}$. For $t = 0.24\ \frac{L^2}{D}$, $L = R$ and $D = D_{eff}$, radial diffusion is approximately twice as fast as 1-D diffusion.

### 3.5.2.4. Diffusion in GLAD Films

The diffusion models for cylindrical nanorods described in sections 3.5.2.2 and 3.5.2.3 are useful in modeling bulk vacancy diffusion in nanostructures where bulk conduction is along the length of the cylindrical nanostructures. From the GLAD film schematic shown in figure 3.8, the nanorods are well spaced and the potential applied along the platinum electrodes result in conduction only along the polycrystalline base layer. Thus vacancies formed in the nanorods as a result of gas interaction will move into the thin polycrystalline base layer and thus the base layer acts as a vacancy sink. Since electron flow is along the polycrystalline base layer, this base layer provides most of the resistance of the GLAD film. For a GLAD $WO_3$ film with baseline thickness of 10 nm and $D = 300\ \text{nm}^2/\text{s}$ at 300 °C (Appendix B), $\tau = .3$ s (from section 3.5.2.1).

This shows that vacancy equilibration is very fast at higher temperatures in the thin polycrystalline base layer. Therefore the time taken for the GLAD film sensor to respond depends on the time taken for the vacancies to diffuse into the polycrystalline layer through the nanorods. Thus the relative height and ratio of the nanorods play a role in determining whether the GLAD film response is surface reaction limited or bulk vacancy diffusion limited. This is further detailed in chapter 5.

### 3.6 Chapter Summary

Table 3.1 summarizes the dependence of $\tau$ and $\Delta\sigma$ on various kinetic and geometric parameters that depends on the film morphology and type of bulk conductivity mechanism. This table provides an overview of the key parameters used in bulk conductivity models, and serves as a quick reference to identify the important parameters that determine sensor response. The change in film conductivity is determined by the surface reaction kinetics, as highlighted in Table 1 (row 1), and the response time is controlled by the rate-limited mechanisms (rows 2 and 3). The models are then compared in chapter 5 to actual sensor test data to assess the effectiveness of predicting the response of planar and nanorod architecture $WO_3$ sensors to $NH_3$.

**Table 3.1.** Parameters controlling sensitivity (change in conductivity) and response time for Surface Reaction Limited and Lattice Diffusion Limited cases. The table also provides information about the response function of both planar and nanorod structured films.

| | Surface Reaction Limited | | Bulk Diffusion Limited | |
|---|---|---|---|---|
| | Planar | Nanorod | Planar | Nanorod |
| Baseline conductivity | $K = \frac{k_2}{k_1 P_{O_2}^a} = \frac{\kappa_{red}^{air}}{\kappa_{ox}^{air}}$ | $K = \frac{k_2}{k_1 P_{O_2}^a} = \frac{\kappa_{red}^{air}}{\kappa_{ox}^{air}}$ | $K = \frac{k_2}{k_1 P_{O_2}^a} = \frac{\kappa_{red}^{air}}{\kappa_{ox}^{air}}$ | $K = \frac{k_2}{k_1 P_{O_2}^a} = \frac{\kappa_{red}^{air}}{\kappa_{ox}^{air}}$ |
| Sensitivity | $K_t = \frac{k_3 P_t^b}{k_1 P_{O_2}^a} = \frac{\kappa_{red}^t}{\kappa_{ox}^{air}}$<br>$K = \frac{k_2}{k_1 P_{O_2}^a} = \frac{\kappa_{red}^{air}}{\kappa_{ox}^{air}}$ | $K_t = \frac{k_3 P_t^b}{k_1 P_{O_2}^a} = \frac{\kappa_{red}^t}{\kappa_{ox}^{air}}$<br>$K = \frac{k_2}{k_1 P_{O_2}^a} = \frac{\kappa_{red}^{air}}{\kappa_{ox}^{air}}$ | $K_t = \frac{k_3 P_t^b}{k_1 P_{O_2}^a} = \frac{\kappa_{red}^t}{\kappa_{ox}^{air}}$<br>$K = \frac{k_2}{k_1 P_{O_2}^a} = \frac{\kappa_{red}^{air}}{\kappa_{ox}^{air}}$ | $K_t = \frac{k_3 P_t^b}{k_1 P_{O_2}^a} = \frac{\kappa_{red}^t}{\kappa_{ox}^{air}}$<br>$K = \frac{k_2}{k_1 P_{O_2}^a} = \frac{\kappa_{red}^{air}}{\kappa_{ox}^{air}}$ |
| Response time | $K$, $K_t$<br>$\frac{V}{A} = L$ | $K$, $K_t$<br>$\frac{V}{A} = \frac{wXL_b + N_{rod}\pi r^2 L_0}{wX + N_{rod} 2\pi r L_0}$ | $D_{eff}$, $L$ | $D_{eff}$, $r$, $L_0$, $L_b$ |
| Dependence of $\tau$ on geometry | $\tau \propto L$ | $\tau \propto r$ | $\tau \propto L^2$ | $\tau \propto r^2$ |
| Step response function | Exponential decay | Exponential decay | Initially $t^{1/2}$, then saturates | Initially $t^{1/2}$, then saturates |

# 4. EXPERIMENTAL METHODS

This chapter details the preparation of the Au-loaded $WO_3$ powder catalyst by standard wet impregnation, as well as the fabrication of Au doped $WO_3$ ($Au/WO_3$) planar films by conventional magnetron sputtering and $Au/WO_3$ nanorod structured films by glancing angle deposition (GLAD). The powder catalyst was subjected to GC/MS and DRIFTS studies, using $NH_3$ gas, for determining the reaction products as a function of temperature, to add as input to the kinetic equations for the $Au/WO_3$ film surface reaction limited models presented in chapter 5. GC/MS and DRIFTS studies also help in identifying the role of Au additives in the reaction. Section 4.1 of this chapter describes the powder catalyst preparation method using standard wet impregnation method. Section 4.2 of the chapter deals with the analytical setup, which includes both GC/MS and DRIFTS, and a detailed view of the microreactor used in the GC/MS study is also given. Section 4.3 of this chapter explains the X-ray diffraction setup, which is a catalyst structural characterization technique used in this study. Section 4.4 of this chapter deals with $Au/WO_3$ planar and GLAD film fabrication. Two physical vapor deposition (PVD) techniques, namely sputtering and e-beam evaporation are presented as they are used in this study. Finally, section 4.5 describes the configuration of the gas delivery system.

## 4.1 Au-loaded $WO_3$ Catalyst Preparation

Aldrich 20 micron (μm) pure $WO_3$ powder with surface area of 1.7 $\frac{m^2}{g}$ and a 0.1% w/w (mass fraction) Au-loaded Aldrich 20 μm $WO_3$ powder catalysts were used in GC/MS and DRIFTS studies. The 0.1% w/w Au-loaded catalyst was prepared by standard wet impregnation using Gold (III) chloride trihydrate ($HAuCl_4.3H_2O$) salt. Calculations showing the mass of $HAuCl_4.3H_2O$ salt (0.02 g) used for 10 g of $WO_3$ powder to get 0.1% w/w Au-loading is given in Appendix D. 0.02 g of $HAuCl_4.3H_2O$ salt was dissolved in water and poured onto 10 g of $WO_3$

support using a pasteur pipette until the entire surface of the $WO_3$ powder was covered with the salt. The slurry was then placed in an oven and heated at 100 °C for 6 hours in air. The catalyst was then packed in a glass tube with silica support of size 90-180 μm and 180-425 μm as shown in Figure 4.1 and placed in the micro reactor. The next step was to reduce the catalyst in a flow of hydrogen (10% $H_2$/Air) for 2 hours at 200 °C to ensure the presence of elemental Au in the catalyst.

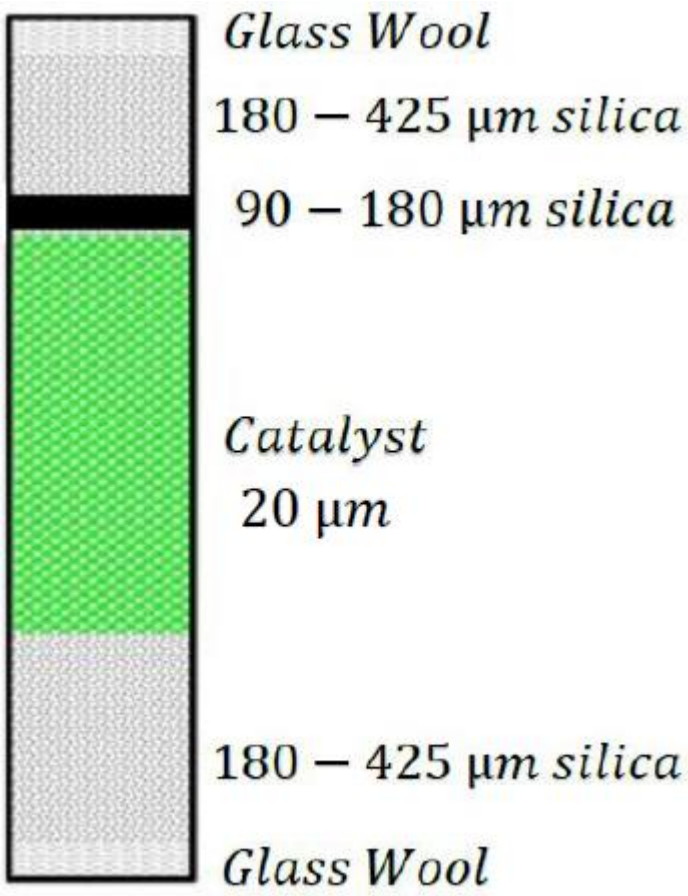


**Figure.4.1.** Packaging of $WO_3$ catalyst in the glass reactor tube.

### 4.2 Analytical Setup for Powder Catalyst Studies

The setup consists of a microreactor, a gas chromatograph and a mass spectrometer.

#### 4.2.1 Microreactor

The Au-loaded and pure $WO_3$ catalysts were packed in glass tubes and placed in the microreactor as shown in figure 4.2 (a).

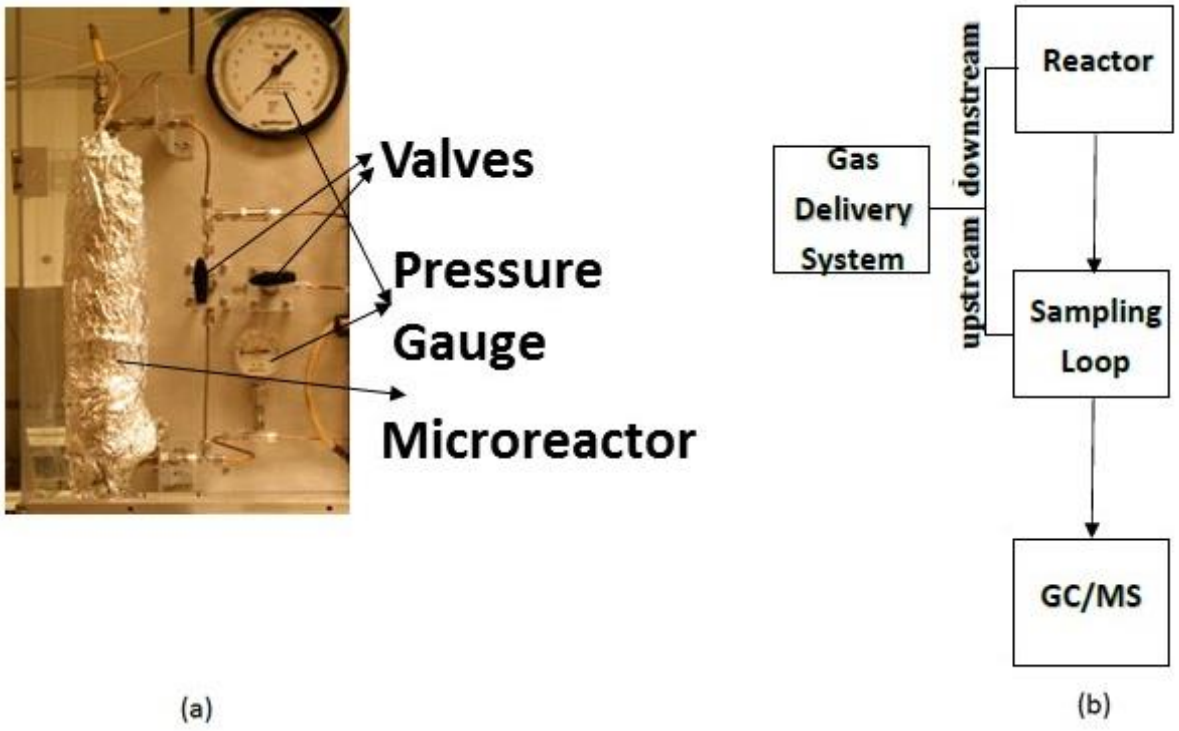


**Figure.4.2.** Microreactor set up and gas flow through the microreactor are illustrated using (a) photograph and (b) block diagram respectively.

The photograph also shows the pressure gauges for measuring upstream (at the base of the reactor, before the $NH_3$ gas mixed in air ($NH_3$/air) reaches the catalyst bed) and downstream (top of the reactor, after the $NH_3$/air passes through the catalyst bed) gas pressure as changes in gas pressure could cause inaccuracies in determining the % conversion of target gas. Also shown in

the picture are pressure valves for determining whether the gas pressure is measured upstream or downstream of the reactor. Figure 4.2 (b) shows the block diagram of $NH_3$/air flow through the microreactor setup. When the gas is sampled downstream, the $NH_3$/air is passed through the catalyst bed in the microreactor before entering the sampling loop, while the gas is directly passed into the sampling loop when it is sampled upstream. From the sampling loop, the gas is passed into the GC and then into the MS.

Figure 4.3, shows an in-depth view of the gas flow through the reactor. There are two gas flow lines, one is connected to a $NH_3$ bottle of 99.99% purity and the other to an air line supplied by a zero air generator. Mass flow controllers (MFCs) were used to control the flow rate of both $NH_3$ and air. The $NH_3$ flow rate was set at 7.3 standard cubic centimeters per minute (sccm) and the air flow rate was set at 80 sccm. The air and $NH_3$ ($NH_3$/air) get mixed together before entering the sampling loop whose volume is approximately 1 ml. The position of the valves is very critical, as valves 3 and 4 can either be in the "on" position or in the "off" position. Valve 4 determines whether the sampling is done upstream or downstream of the reactor. In the "off" position, the sampling is done downstream of the reactor, and in the "on" position, sampling is done upstream of the reactor. Sampling only takes place if valve 3 is in the "on" position during which the sampled gas flows to the injector port (GC); and in the "off" position, the gas is injected into the GC column under a flow of carrier gas (Helium).

In this study, both pure and 0.1% w/w Au-loaded catalysts were packed in two separate glass reactor tubes and each one was placed in the microreactor where they were pretreated at a temperature of 450 °C under a constant flow of air for 2 hours. The catalyst bed in the microreactor was heated using a temperature controller from room temperature to 450 °C at a rate of 5 °C /min. As the temperature in the catalyst bed increased, $NH_3$ gas sampling was done

both downstream and upstream of the reactor. The reaction products will only be seen downstream, and by comparing the ratio of $NH_3$ peak area observed downstream with respect to upstream (from gas chromatogram) along with the fragmentation pattern (from MS) in both cases, the % conversion of target gas, the type of reactant products formed and the % yield of products can be determined, for both pure and 0.1% w/w Au-loaded $WO_3$ catalysts.

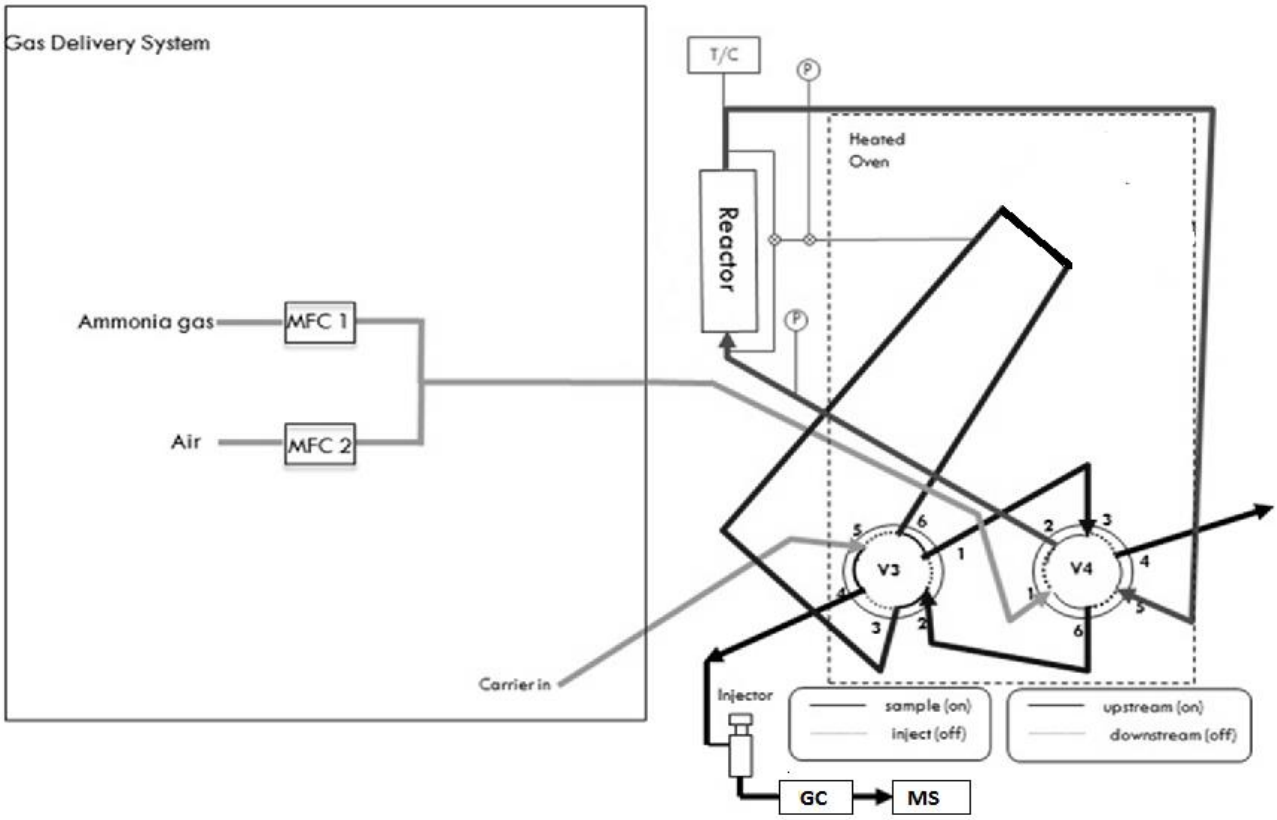


**Figure.4.3.** Reactor flow diagram showing the target gas flow through the microreactor. Also shown are valves V4 and V3, which determine whether sampling is done upstream or downstream of the rector, and whether sampling or injection is done, respectively.

### 4.2.2 GC/MS

Gas chromatography/Mass spectroscopy (GC/MS) is useful for separating various gaseous reaction products and identifying their molecular weight, elemental composition and structural information. This section gives a brief overview of the gas chromatography (GC) and Mass spectrometry (MS) techniques and the various components that make up the combined GC/MS instrument.

#### 4.2.2.1 Gas Chromatography (GC)

In this technique, the components of a mixture in the gaseous state are separated as the mixture passes over a stationary liquid or solid phase. Differences in the interaction between the sample components and the stationary phase account for the separation. The components of a mixture are eluted from the column and they pass directly into the detector (mass spectrometer is the detector used in this study) and the response of the detector is plotted as a function of time.[133]

##### 4.2.2.1.1 Instrumentation

The components of a gas chromatograph are shown in figure 4.4, each of which are described in detail below.

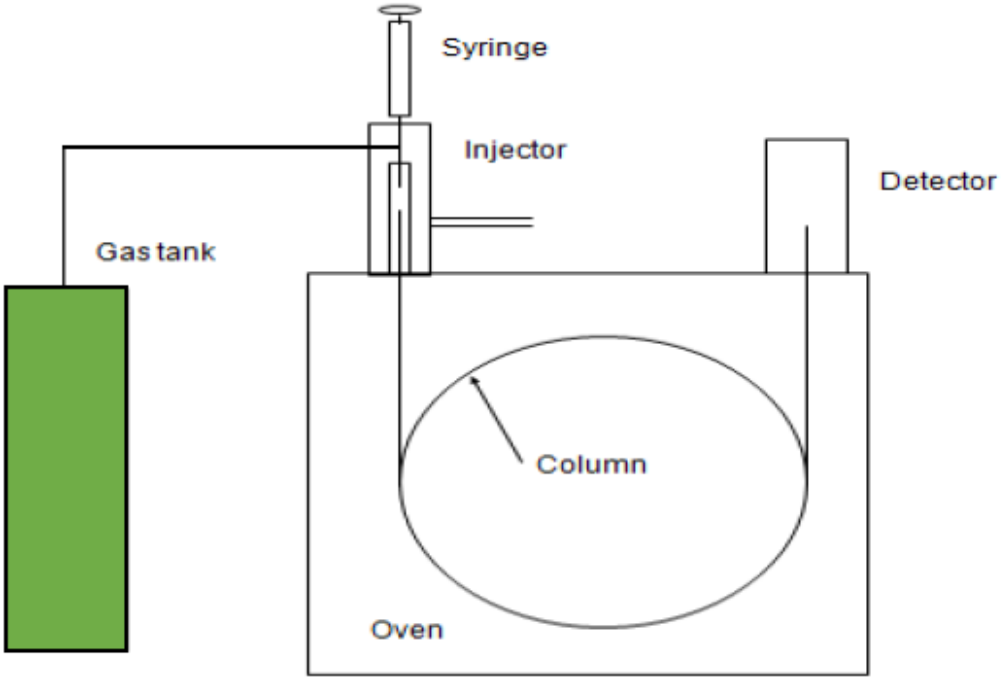


**Figure.4.4**. Illustration of various components of a Gas Chromatograph (GC).

***(A) Carrier Gas***

The Carrier gas (mobile phase) plays an important role in gas chromatography as it serves to push the sampling gas through the column and into the mass spectrometer or other detectors. Chemically inert and relatively inexpensive gases, like helium, are commonly used as the carrier gas. A high pressure gas cylinder is generally used as the carrier gas reservoir.

***(B) Injector***

The sampling gas is introduced directly into the carrier gas through the injector port. The injector is either in split mode or splitless mode. If only a small volume of the sample is required, one could use a split injector to remove excess gas. A splitless injector is generally used only if a limited amount of sampling gas is available. Figure 4.5 shows the split mode and splitless mode of the injector where the purge valve is open for the split injector and closed for the splitless

injector. A split injector with a split ratio (represents volume fraction of sample entering the column) of 100 was used in this study.

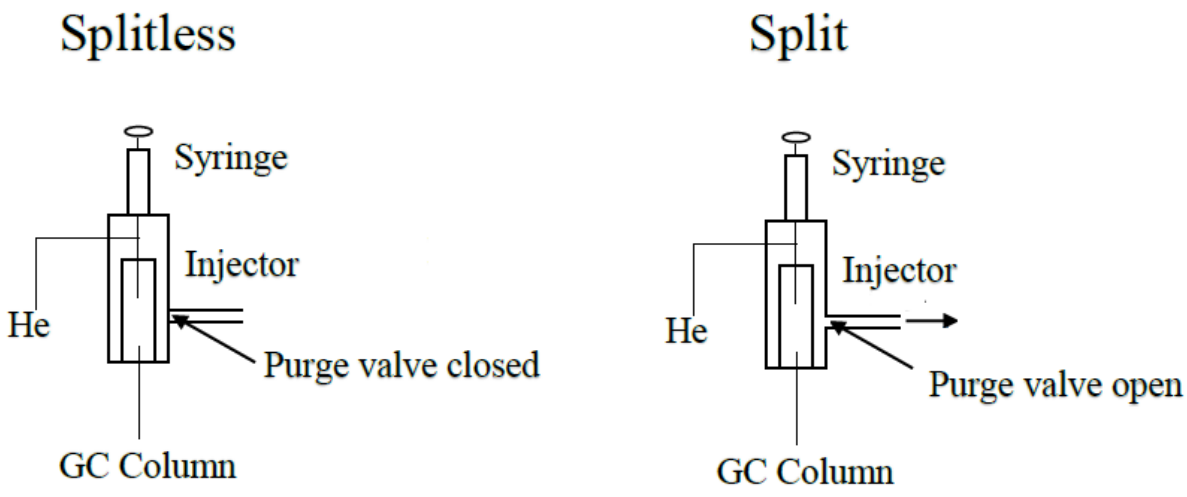


**Figure.4.5.** Schematic of Split and Splitless injectors

***(C) Oven***

The oven in the GC is programmable and can accurately control the temperature of the GC column to within a few tenths of a degree to ensure optimum gas mixture separation in the column. The temperature programming is done such that it starts at a lower temperature and slowly ramps to a higher temperature. A typical temperature profile is shown in figure 4.6.

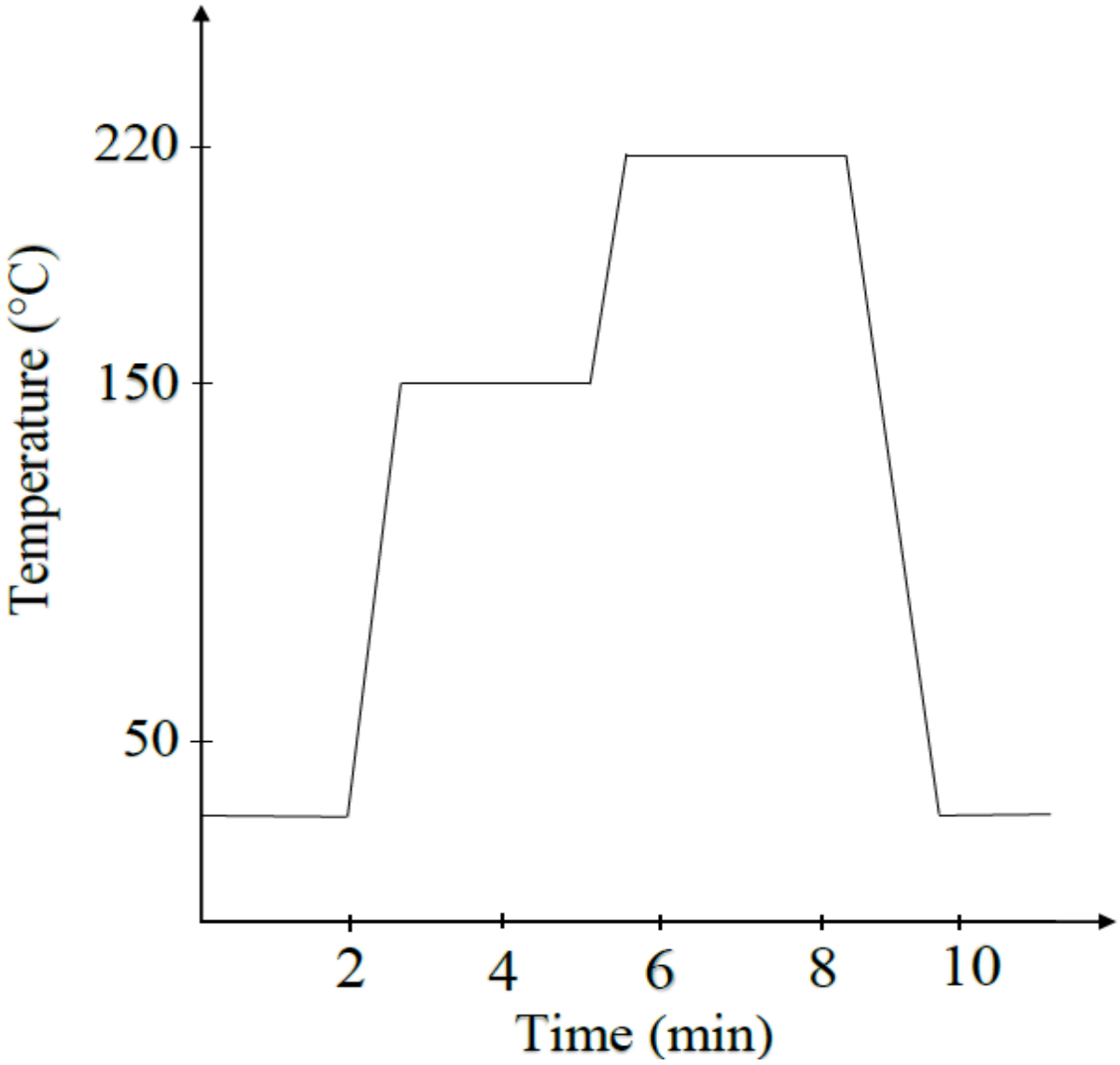


**Figure 4.6.** Thermal profile used for the GC oven temperature program.

***(D) Column***

The packing architecture in the GC column provides the basis for the gas mixture separation process. The column can be either stainless steel or copper tubes packed with either a solid substrate (gas solid chromatography) or a liquid coating on an inert solid (gas liquid chromatography). Glass tubes are frequently used for samples that react with copper or stainless

steel. The column is placed inside the GC oven. In gas solid chromatography, common solids are charcoal, a synthetic zeolite called "molecular sieve", or a combination of the two.[102]

In choosing the correct column for separation of a gas mixture, one needs to consider the stability of the column towards the components of the mixture. If the column undergoes a chemical reaction with the injected compound, it can then result in erroneous peaks. The adsorbents for gas solid chromatography usually have very large surface areas or high level of porosity.[102] Normally selection of a column for separation of a particular gas mixture is based on trial and error. However, recently the major consideration for selecting a column for gas mixture separation appears to be the polarity of the stationary phase and the nature of the mixture to be separated. Ideally they should be similar. The column used in this study is a zeolite column (polystyrene divinylbenzene) to ensure separation of $NH_3$ from $H_2O$.

***(E) Detector***

Detectors are located at the end of the column and provide a quantitative measurement of the sample compounds. Although there are many types of detectors available, mass spectrometer, thermal conductivity, flame ionization and electron capture detectors are the most commonly used. Detectors must have good sensitivity, stability, reasonable lifetime and a linear response characteristic over a range of sample concentrations, and most of the above mentioned detectors satisfy these requirements. A mass spectrometer is one of the most commonly used detectors and was used in this study. Further explanation of the advantages of using a mass spectrometer is provided in section 4.2.2.2.

***(F) Factors Affecting Separation***

The following are some of the factors that affect gas separation, and these parameters can be altered to improve efficiency in gas mixture separation.

1. Carrier gas flow rate: There is an optimum flow rate that gives maximum efficiency. If the flow rate is too fast, then the peaks will not be resolved, as the components of the mixture are pushed through the column and have very little time to interact with the stationary phase in the column.[134] If the flow rate is too slow, better separation can be obtained but then this will result in longer retention times (amount of time a compound spends in the column) than that observed for higher flow rates. Thus the optimum flow rate needs to be determined experimentally to ensure good separation and fast retention times.
2. Polarity of the stationary phase vs polarity of the compound: This is a key variable in determining efficiency of the column. Better separation takes place if the stationary phase and the gas compound have the same polarity. Therefore considerable care must be taken in choosing the correct polarity, or separation will not take place.
3. Column Length: As length increases, separation also improves but this will also result in increased gas retention times and increased peak broadening due to longitudinal diffusion.
4. Amount of gas mixture injected: If too much gas mixture is injected into the column, significant tailing will occur, which in turn results in poor gas separation. This is why mostly split injectors are used for gas separation in order to prevent column and detector overloading.[134]
5. Column Temperature: Vapor pressure of the stationary phase and the sample helps in determining the operable column temperature for efficient separation. The temperature

should not be too high as it will destroy the stationary phase, and it should not be too low as it needs to maintain the sample in the vapor state.[134]

#### 4.2.2.2 Mass Spectrometer (MS)

Mass Spectrometry is used to identify the molecular weight, elemental composition and structural information about the gaseous species separated by the GC. In order to measure the characteristics of individual molecules, a mass spectrometer converts them to ions so that they can be moved about and manipulated by external electric and magnetic fields.[136]

##### 4.2.2.2.1 Instrumentation

The general operation of a mass spectrometer involves creating gas phase ions (using an ion source), separating the ions in space or time based on their mass to charge ratio (m/z); and measuring the quantity of ions at each m/z.[136]

***(A) Ion Source***

Although there are several different types of ionization, Electron Impact Ionization (EI) was used in this study. In this ionization technique, a beam of electrons generated from a filament source passes through the gas phase sample and collides with neutral analyte molecules (M) to produce a positively charged ion.[136] This is the only commonly used ionization technique that produces a radical ion (which has unpaired valence electrons), and is the most commonly used method in GC/MS studies.[137]

***(B) Mass Analyzer***

A mass analyzer is a component of the mass spectrometer that takes ionized masses and separates them based on the m/z. The quadrupole mass analyzer (QMA) is the most common mass analyzer due to its low scan times, compact design, and low cost compared to other analyzers. The mass filter consists of four parallel rods which are arranged in a quadrupole

geometry. Two opposite rods have an applied potential of (U+Vcos(ωt)) and the other two rods have a potential of -(U+Vcos(ωt)), where U is a dc voltage and Vcos(ωt) is the variable RF ac voltage. Ions are accelerated between the rods and must keep a stable trajectory in the *xz* plane (high pass-mass filter) and the *yz* plane (low-pass mass filter) to get to the detector.[136] Changing the applied voltages will affect the trajectory of the ions down the flight path between the four rods. For a given ac and dc voltage, only ions with a certain mass to charge ratio (m/z) are allowed to pass through the filter while the rest of the ions are moved out from the original path. Thus the quadrupole acts as a narrow band mass filter. Figure 4.7 shows a schematic of the QMA.

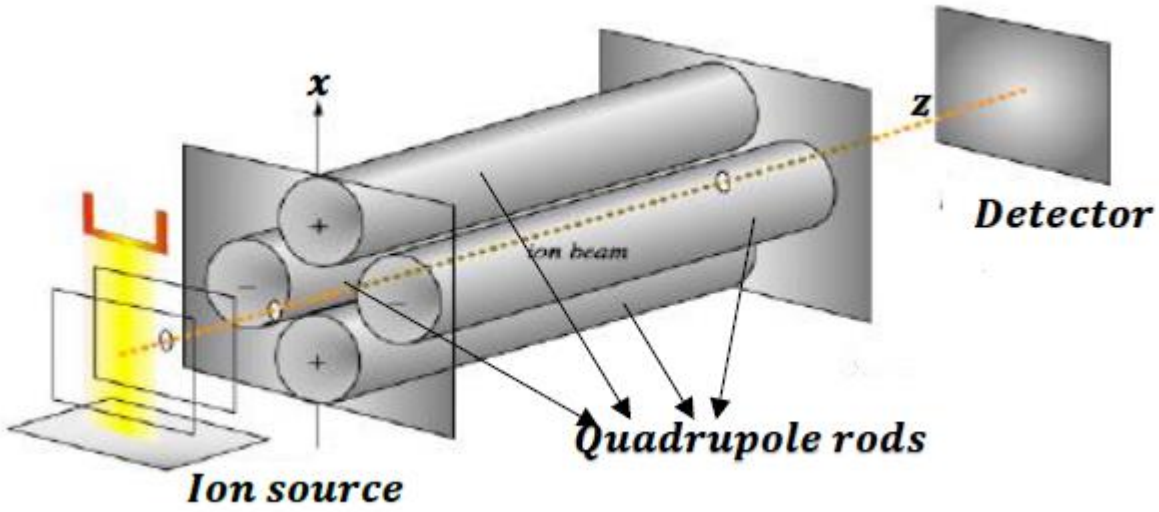


**Figure 4.7**. Illustration of a quadrupole mass analyzer.[136]

***(C) Detector***

Faraday cups and electron multipliers are the commonly used detectors. Figure 4.8 shows a schematic of an electron multiplier which was used in this study. An incident ion beam causes secondary electrons to be emitted from the first dynode.[137] These emitted electrons are

accelerated to the second dynode where each causes additional secondary electron emission. These in turn are accelerated to a third dynode and so on, eventually reaching the final dynode by which the incident ion beam is transformed into a cascade of electrons that are collected by the metal anode. An electron multiplier detects every ion emerging from the quadrupole mass analyzer and the overall system sensitivity depends on the efficiency of the electron multiplier.

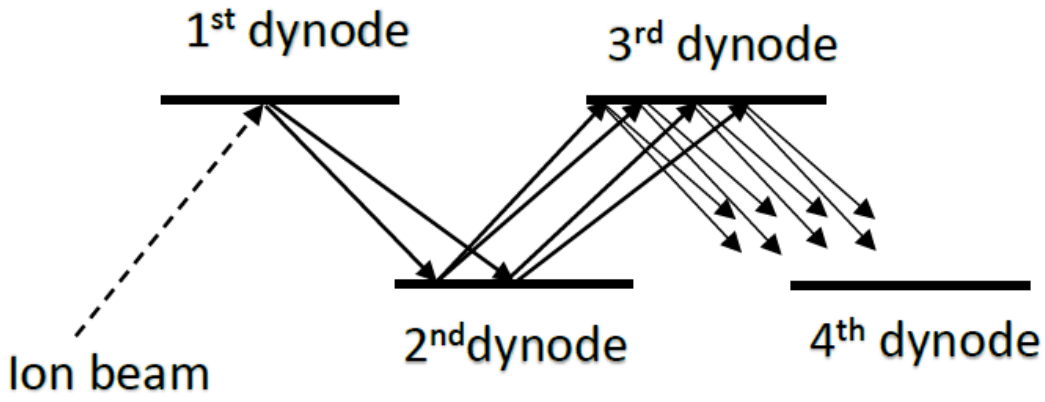


**Figure 4.8.** Signal amplification using an electron multiplier, where an incident ion beam transforms into a cascade of electrons due to secondary electrons ejected from the dynodes.

For this study, a Thermo Scientific ISQ single quadrupole GC/MS was used for the analysis. The Thermo Scientific ISQ GC/MS consists of a Thermo Scientific TRACE$^{TM}$ Ultra gas chromatograph and a Thermo Scientific single quadrupole mass spectrometer. Analysis was done in electron ionization mode, to determine the $NH_3$ reaction products, by scanning for atomic masses ranging from 12 – 100 amu. The sampled mixture from the micro reactor entered the GC through the split injector with a split ratio of 100. A $(30m, 0.25\ \mu m, 0.25mm\ ID)$ Agilent Plot Q column was chosen to separate $NH_3$ from $H_2O$. The oven temperature was set to 120 °C. A helium carrier flow rate of 1.7 ml/min was used for the study of $NH_3$ reaction on both the 0.1% w/w Au-loaded $WO_3$ catalyst and pure $WO_3$ catalyst.

### 4.2.3 Diffuse Reflectance Infrared Fourier Transform Spectroscopy (DRIFTS)

Diffuse Reflectance Spectroscopy (DRS) is a spectroscopic technique based on the reflection of light in the ultraviolet (UV), visible (VIS) and near-infrared (NIR) regions by a powdered sample.[112] DRIFTS (Diffuse Reflectance Infrared Fourier Transform Spectroscopy), which is a type of DRS, has been used in this study to determine $NH_3$ adsorption sites on 0.1% w/w Au-loaded and pure $WO_3$ powder catalysts as well as the chemical reactions and thermal behavior of the adsorbed $NH_3$ gas on the catalyst surface.

DRIFTS is an infrared spectroscopic method which is particularly useful for obtaining chemical and structural information of powder samples.[138] When a focused beam of infrared radiation reaches the sample surface, it can (i) be absorbed (ii) be reflected from the surface or (iii) penetrate the sample before being scattered.[139] The scattered light is collected in an integration sphere and relayed to the IR detector, where the absorption by the chemical groups is revealed.[139]

There are two types of reflected beams: specular and diffuse. The part of the beam that is scattered within a sample and reflected back to the surface is typically called diffuse reflectance. For diffuse reflection, the angle of incidence is not equal to the angle of reflection. Specular reflection occurs at the interface of two materials with different refractive indices and is characterized by the rule that the angle of incidence is equal to the angle of reflection.[139]

The powders that need to be sampled are mixed with a non-absorbing matrix like Potassium Bromide (KBr) where the ratio of sample to the matrix is between 1 and 5. Deeper penetration of infrared beams, due to dilution of the sample with the matrix, increases the contribution of the diffuse reflectance while minimizing the specular reflectance part.[140] The specular reflectance component in the reflectance spectra can cause changes in band shapes and

relative intensities, and can also cause band inversions; and thus sample dilution with KBr minimizes these effects.[140] The incident light is partially absorbed, partially scattered. In practice, DRIFT spectra can exhibit both absorbance and reflectance features due to contributions from transmission, internal and specular reflectance components.[112] Quality of DRIFT spectra are related to further factors like particle size, refractive index, homogeneity, packing and optical geometry effects, to name a few.

One of the main advantages of DRIFTS is that it can carried out under controlled conditions of temperature and ambient gases.[112] Other advantages include good sensitivity and very little preparation time.[139] The disadvantages of this technique are the need for consistent particle size for quantitative results, and limited depth penetration.[139] Figure 4.9 (a) shows a typical DRIFTS attachment for *in situ* measurements. Its construction with two ellipsoidal mirrors provides that mainly the diffuse component of the reflected light is captured.[112, 140] In conjunction with this attachment, a Praying Mantis™ (Harrick Scientific Production, IBC) high temperature reaction chamber (figure 4.9 (b)) with gas ports can be used for evacuating the chamber and/or for introducing gas.

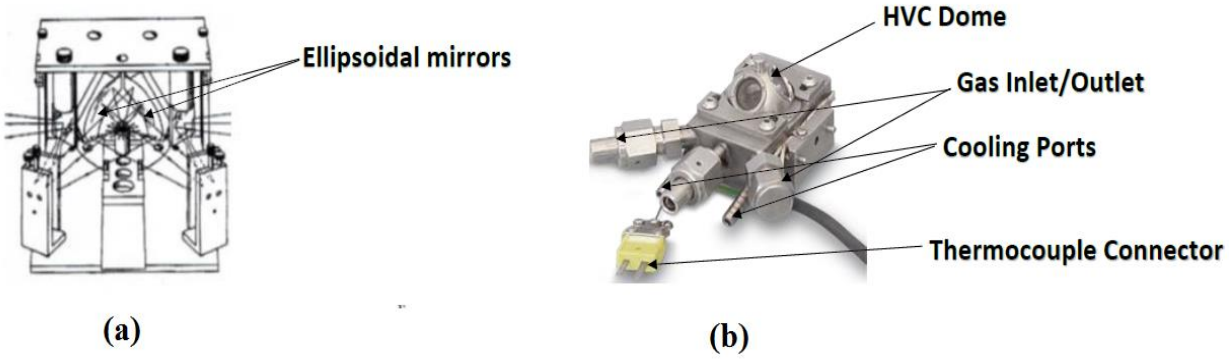


**Figure 4.9.** *In situ* DRIFTS cell: (a) diffuse reflection attachment and (b) Harrick Preying Mantis™ high temperature chamber.[112]

In this study, the DRIFT spectra were recorded using Nicolet 6700 Fourier Transform Infrared (FTIR) spectrometer equipped with the Praying Mantis$^{TM}$ (Harrick Scientific Production, IBC) accessory for Diffuse Reflectance Fourier Transform (DRIFT) applications. KBr powder was placed in the sample cup inside a classical Harrick Scientific high temperature reaction chamber (HVC). The sample cup in HVC is placed on a temperature-controlled sample stages equipped with a cartridge heater and a thermocouple. The temperature of the sample cup is controlled by a Harrick Scientific Automatic Temperature controller (ATC-024-1). The "soil" sample ($WO_3$ powder catalyst) was spread on the top of the KBr powder in the sample cup for DRIFT studies. Spectra were recorded at varying temperatures by accumulation of 64 scans at 4 $cm^{-1}$ resolution using DTGS (deuterated triglycine sulfate) detector. Before $NH_3$ adsorption studies, all the $WO_3$ samples were pretreated under synthetic air flow with 1000 sccm flow rate at 400 °C for more than 2 hours. After pretreatment, temperature was varied and single beams (spectrum of the sample surface under synthetic air flow before any $NH_3$ exposure) were recorded at these temperatures of interest. This was followed by the introduction of 10 % ammonia in argon ($NH_3$/Ar) into the chamber, for these different temperatures, through a flow system with 1000 sccm flow rate for 5 min and difference spectrum (spectrum of the surface after $NH_3$ adsorption subtracted from the single beam of the surface before adsorption at the same temperature) was recorded at these temperatures. The chamber was then purged with synthetic air for 10 minutes and difference spectrum is also recorded under these conditions as well.

In summary, the sequence was as follows: 1) pretreatment at 400 °C, 2) Temperature was changed to the desired value under synthetic air, 3) single beam was recorded at this temperature under synthetic air atmosphere, 4) 1000 sccm of 10% NH3/Ar was introduced into the chamber,

5) difference spectrum was recorded under 10% $NH_3$/Ar, 5) environment was switched to synthetic air, 6) difference spectrum was recorded under synthetic air.

### 4.3 Structural Characterization of Samples using X-ray Diffraction (XRD)

XRD is well known probe that allows identifying and studying crystalline materials by using the phenomenon of wave interference and diffraction. Diffraction occurs only when Bragg's law is satisfied:[141]

$$n\lambda = 2dsin\theta \quad (4.1)$$

where $d$ is the spacing between the atomic planes in a crystalline material, $\theta$ is the incident angle of the X-rays, $\lambda$ is the wavelength of the X-rays and n is an integer. Diffraction occurs when the penetrating X-ray radiation, enters a crystalline substance and is scattered.[141] The direction and intensity of the scattered (diffracted) beams depends on the atomic spacing and orientation of the crystal lattice with respect to the incident beam.[141] Figure 4.10 shows a simple diagram of the wave interference. The phase difference between adjacent scattered rays must be an integral number of wavelengths to get constructive interference.

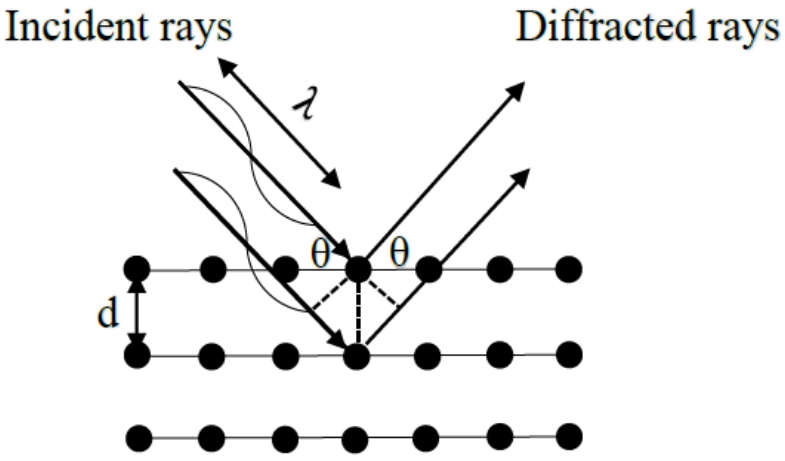


**Figure 4.10.** Simple Bragg's law model that shows the condition for constructive wave interference.

In addition to finding crystal lattice parameters, XRD can also reveal the orientation of a single crystallite or grain, the crystal structure of an unknown material, and the size, shape and internal stress of small crystalline regions. Determination of crystallite sizes is also of key importance in the field of metal oxide based gas sensors. The simplest method is to use the Scherrer equation and the full width half maximum (FWHM) of the peak. The Scherrer equation is given by:[142]

$$L = \frac{K\lambda}{\beta\cos(\theta)} \tag{4.2}$$

where $L$ is the average crystallite size measured in the direction of X-Ray scattering vector, $K$ is a constant related to crystalline shape normally taken to be 0.9, $\lambda$ is the X-ray wavelength , $\beta$ is the FWHM of the diffracted peak in radians, and $\theta$ is the Bragg angle. This analysis, however, only gives the lower bound of the crystallite size as it does not include other factors that contribute to peak broadening such as strain and instrument resolution.

For this study, powder X-ray diffraction (XRD) was done by mixing the pure and 0.1% w/w Au-loaded $WO_3$ powder catalysts with isopropanol and letting it dry on a zero background silica support. A Panalytical X'pert Pro Diffractometer using CuKα radiation (λ=1.5406 Å) in a Bragg-Brentano geometry was used for analysis. A pixcel multichannel detector was used as the detector. Powder diffraction patterns were obtained in a 2θ range of 16-60° with a divergence slit of 0.25°. Powder X-ray diffraction (XRD) was done on the pure and 0.1% w/w Au-loaded catalysts post $NH_3$ testing in order to determine whether or not any tungsten bronze was formed or whether any conversion to nitrides occurred.

**4.4 Fabrication of Metal Oxide Films on Chemiresistive Sensor Platform.**

$WO_3$ sensing films were fabricated using the thin film synthesis lab in the Laboratory of Surface Science and Technology (LASST) at the University of Maine. Chemiresistive sensor

devices consisting of a $WO_3$ semiconducting metal oxide thin film deposited over an interdigitated platinum electrode array were fabricated on a single crystal r-cut sapphire substrate. A 10 nm thick Zirconia layer was used as an adhesion layer to adhere the platinum electrodes firmly on the sapphire substrate.[114] R-cut sapphire was chosen as the substrate because (i) it is a good electrical insulator on which to deposit the semiconducting $WO_3$ gas sensor films, (ii) highly polished single crystal wafers are readily available, and (iii) the $WO_3/Al_2O_3$ interface remains unreactive at high temperatures.[26] Details of the chemiresistive sensing platform is shown in Figure 4.11. The back of the platform contains a serpentine heater and resistive temperature device (RTD). The platform is calibrated by heating the device in an oven with a calibrated RTD against which the internal RTD is compared. Even though the temperature of the platform can be controlled using the RTD, it has been observed that prolonged heating of the sensor leads to RTD calibration errors which can cause temperature variations.

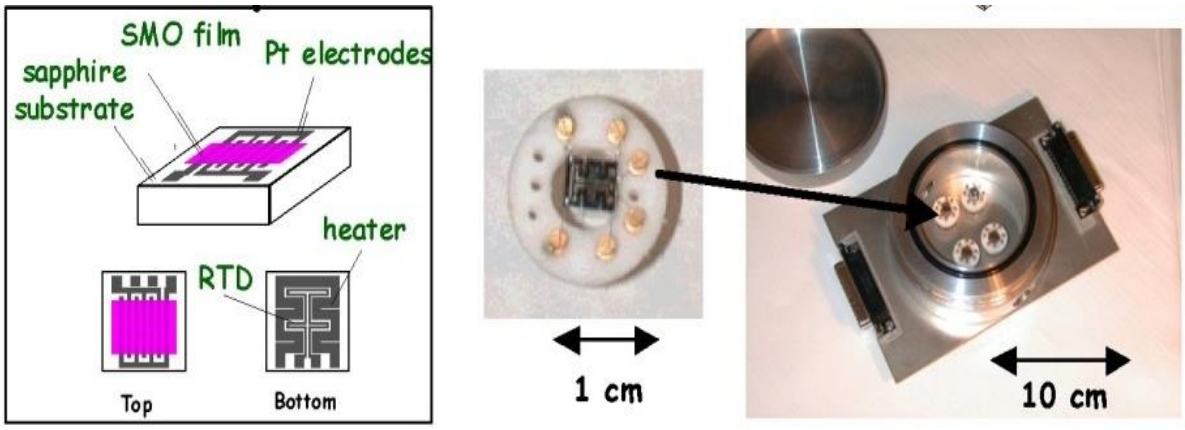


**Figure 4.11.** SMO chemiresistive thin film sensor device comprised of a SMO film deposited over a platinum electrode array. The reverse side of the device has a thin film heater and resistive temperature device (RTD). The sensor is wire-bonded into a TO-8 header that plugs into a gas-flow test cell.[114]

This section outlines the thin film fabrication process of GLAD and planar Au/$WO_3$ films. Emphasis has been placed on physical vapor deposition techniques, namely magnetron sputtering and e-beam evaporation.

### 4.4.1 Sputter Deposition

Sputtering is a physical vapor deposition (PVD) technique by which atoms are ejected from a solid target by bombardment of energetic particles. This process is driven by momentum exchange between ions and atoms in the target due to collisions.[135] Bombardment of the target with the incident $Ar^+$ ions results in the ejection of target atoms that traverse through the plasma and gets deposited onto the substrate.

In sputtering, both the target material and the substrate are placed in a vacuum chamber and a voltage is applied between them so that the target is the cathode and the substrate is the anode.[135] An $Ar^+$ plasma, under the presence of an electric field, bombards the target and sputters off the material that transverses through the plasma to the substrate surface. Figure 4.12 shows a schematic of the sputtering system configuration.

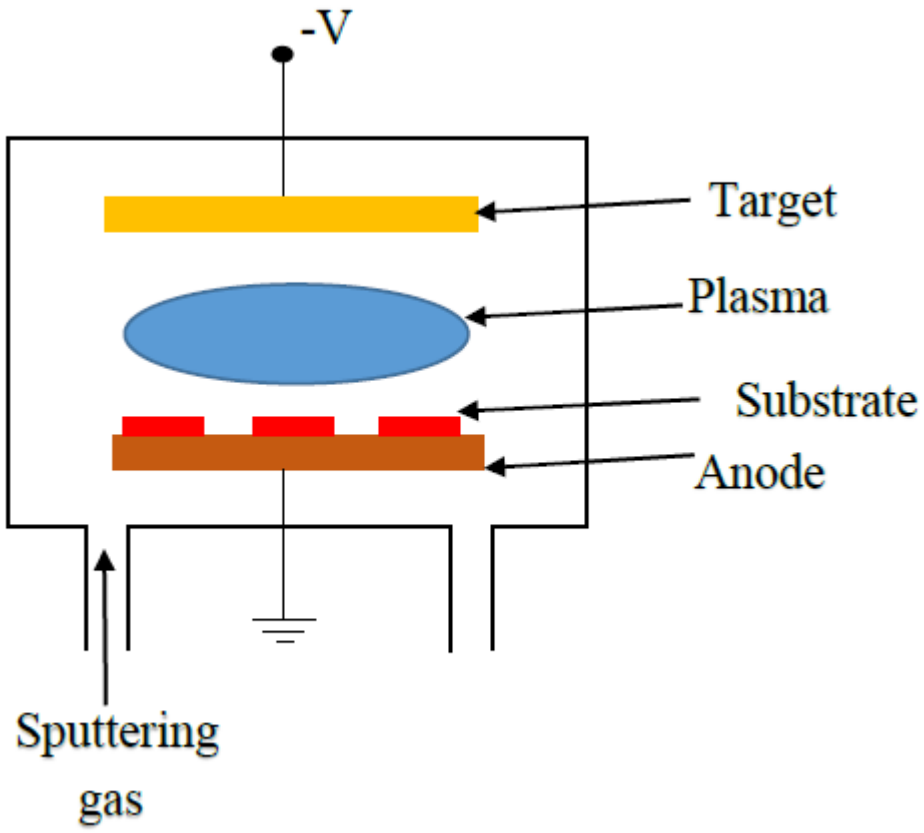


**Figure 4.12.** A general schematic of a sputtering system. An $Ar^+$ plasma sputters the target in the presence of an electric field and produces atomic species that are collected on the substrate.

#### 4.4.1.1 Plasma Generation

A plasma is generated when neutral atoms collide with high energy electrons. Stray electrons near the target accelerate towards the substrate and collide with the neutral gas atoms converting them into positively charged ions. This process gives two electrons per ion which ionizes more atoms creating a cascading process until a plasma is formed.[135]

$$e^- + A_r \rightarrow A_r^+ + 2e^- \quad (4.3)$$

The breakdown voltage at which the plasma is formed depends on the chamber pressure. At very low chamber pressure, there are not sufficient collisions to sustain a plasma, whereas at high

pressure there are too many collisions such that the electrons do not have sufficient energy to ionize atoms.

#### 4.4.1.2 Sputter Yield and Deposition Rate

Sputter yield is defined and can be expressed mathematically as:

$$Sputter\ Yield\ (S) = \frac{Number\ of\ sputtered\ atoms}{Number\ of\ incident\ ions} \quad (4.4)$$

The sputter yield depends on the type of target, the binding energy of target atoms, the relative mass of incident ions and the ion energy and angle of incidence.[135] S can vary in range from 0 to 1. Sputtered atoms from the target reach the substrate by diffusing through the plasma where additional chemical reactions can occur.[135] Ions and neutral gas atoms can also get embedded into a growing film as impurities. The deposition rate is proportional to sputter yield and depends on the argon partial pressure. Higher pressure means more collisions and less energy for the ions while lower pressure results in less scattering of Ar ions.

#### 4.4.1.3 Reactive Magnetron Sputtering

An electron in the presence of an electric and magnetic field undergoes a helical trajectory. In magnetron sputtering,[135] magnets with alternating polarity are attached to the back of the target (an elemental W target was used in this study). These magnets create curved magnetic field lines which confine the secondary electrons to be trapped near the target surface. The high concentration of electrons in the magnetic field region increases the ionization probability near the target, and this in turn creates a denser plasma at pressures much lower than that required for conventional sputtering. [135] The electron density and the number of generated ions are highest when the magnetic field is parallel to the substrate surface, and therefore the highest sputtering yield occurs on the target right below this region. One concern in using magnetron sputtering systems is the formation of an erosion ring on the target (due to stationary

magnetic field) which in turn could affect film uniformity. To avoid this, rotating magnetron rings are occasionally used.[135] In the case of reactive magnetron sputtering, a reactive gas ($O_2$) is added to the inert gas (Ar) to chemically react with the sputtered atoms in the plasma phase as well as the target and substrate surfaces. The reaction will take place on the substrate if the sputtering rate is faster than the chemical reaction rate. Thus, gas flow rates need to be adjusted to get the desired chemical composition. One major issue with reactive magnetron sputtering is that target oxidation can take place, which can reduce the sputtering yield.

### 4.4.2. E-beam Evaporation

Like sputtering, e-beam evaporation is also a PVD technique where the substrate is placed inside a vacuum chamber, in which a target (source) material to be deposited is also located. In this technique, a high kinetic energy beam of electrons is directed at the evaporation source. Upon impact, the high kinetic energy is converted into thermal energy, heating up and evaporating the target material. The rate of mass removal from the source material depends on the vapor pressure of the source material. Vapor pressures of $\sim 10^{-6}$ Torr are needed in order to achieve deposition rates of $\sim$ 1 monolayer/sec which is high enough for manufacturing purposes.

Some of the advantages of e-beam evaporation include: high film deposition rates, less substrate surface damage and substrate heating from impinging atoms during film growth since arriving atoms have lower energy than that for sputter deposition, and excellent purity of the film because of the ultra-high vacuum conditions used during evaporation. A disadvantage of this technique is that due to the low energy of the arriving atoms, the diffusion rate of these atoms on the substrate tends to be lower than for sputtering and this in turn can affect film composition.

### 4.4.3 Fabrication of GLAD Au/$WO_3$ and Planar Au/$WO_3$ Films

100 nm Au/$WO_3$ GLAD films were fabricated in a high vacuum chamber operating with a base pressure of $<1\times10^{-5}$ Pa. A home-made GLAD manipulator equipped with a DC motor maintained the azimuthal sample rotation at a speed of 5 rpm during each deposition. Films were deposited using magnetron sputtering at room temperature, and with a substrate tilt angle of 80° with respect to the normal. A 7.5 cm diameter W target with a purity of 99.95% was located 11 cm from centerline of the substrate and was presputtered in argon (Ar) for 10 min prior to film deposition. The deposition rate and film thickness were measured *in situ* by means of a quartz crystal oscillator calibrated against surface profilometry, X-ray reflectivity, and scanning electron microscopy (SEM) measurements. $WO_3$ films with a thickness of ~100 nm were grown in Ar and $O_2$ gas mixtures at a total pressure of 0.26 Pa using flow rates of 4 and 6 sccm, respectively. For this case, the DC power was 100W with a 685 V discharge voltage. The deposition rate for $WO_3$ films was approximately 3.0 nm/min. After $WO_3$ deposition, an equivalent thickness of 1.5 nm of Au was deposited on top of the GLAD $WO_3$ film using electron beam evaporation.[52] Films were characterized after post-deposition annealing treatments at 500 °C in air for 5 h.

Au/$WO_3$ planar films were deposited to a thickness of either 125 nm or 250 nm at room temperature using reactive RF magnetron sputtering. The films were grown at a rate of 5 nm/min using a substrate tilt angle of 17.6° with respect to the vapor flux, in an Ar and $O_2$ gas mixture at 3 mTorr using a flow rate of 6 and 4 sccm, respectively, and with a RF power of 300 W. Film thickness was measured *in situ* by means of a quartz crystal oscillator. Films were subjected to post-deposition annealing treatments at 500 °C in air for 5 h. To incorporate Au nanoparticles on the planar $WO_3$ film surface, the tungsten magnetron target was shuttered and 1.5 nm of Au was

deposited with a second magnetron source equipped with a Au target. The rate of deposition was approximately 0.15 nm/min.

### 4.5 Gas Delivery Systems (GDS) for Testing $NH_3$ Response of Chemiresistive Sensors

In this study two types of GDS systems were used for testing planar and GLAD film chemiresistive sensors. A schematic of the GDS used for testing planar films is shown in figure 4.13. The properties of the gas delivery system are very important as far as sensor testing is concerned. In order to get a reliable gas sensor one needs to be sure that the gas delivery system is functioning properly and that the required amount of gas is being pumped into the test cell, free of contaminations.

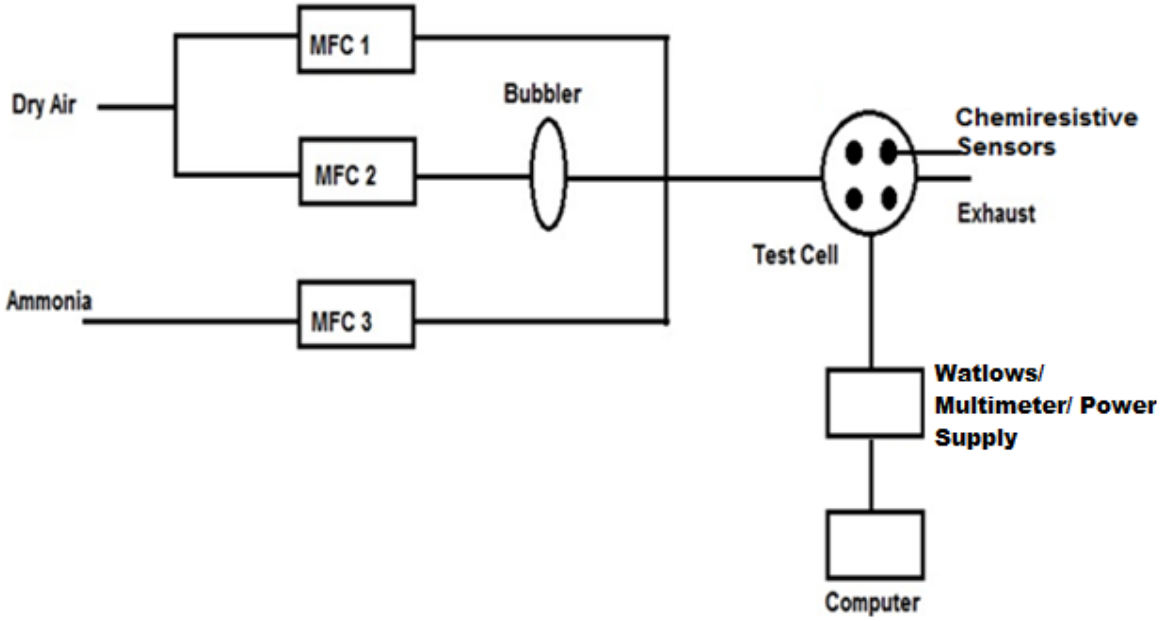


**Figure 4.13.** Schematic of the gas delivery system used for planar film sensors.

Since exposure to $NH_3$ is potentially harmful to humans, the gas delivery system was assembled inside a fume hood. The film resistance was recorded using a Keithley 2000 digital

multimeter. WATLOW temperature controllers were used to control the temperature using the internal RTD on the sensor. Tylan 2900 series mass flow controllers (MFC) were used to provide the desired flow rates through the test cell. Dry air was fed through an MFC into a bubbler to produce saturated air that was then mixed with dry air to achieve the desired humidity levels. Gas flow from a third channel with 5 ppm $NH_3$ in dry air was added to obtain the desired $NH_3$ concentrations in the test cell.

For this study, the planar sensors were set to a temperature of 450 °C and allowed to stabilize for 2 hours with 150 sccm of air flowing through the test cell of volume 100.6 $cm^3$, with 15% relative humidity. Both 125 and 250 nm planar $WO_3$ film sensors were then exposed to 600, 100, 500, and 200 ppb levels of $NH_3$ gas, respectively, with each exposure lasting 40 minutes. Once the exposures were completed, the $NH_3$ was turned off and the sensor was left to recover in 150 sccm flow of air. The sensor response determined from the experiment is in terms of resistance.

Gas delivery system used for testing GLAD films was slightly different from the system used for testing planar films. GLAD film were tested in a portable GDS which had the test cell and associated electronics (for heating the sensors to its operating temperature and measuring sensor resistance) such as power distribution board, microcontroller board, heater controller board, resistance measurement board and sensor carrier board housed in a tube (11.25 cm in diameter) made of stainless shim steel as shown in figure 4.14. 24 V DC power supply and laptop of sensor response measurements were placed externally. The main objective behind the development of this GDS was to do *in situ* measurements of $NH_3$ concentrations in remote locations which required a portable system as opposed to the system used for testing planar films which is bulky. In this study, tests were done similar to planar film tests, in controlled conditions

inside a fume hood. The test cell volume of this system was of similar dimensions (100.6 $cm^3$) to the one used for testing planar films. MFCs, bubbler, gas lines and $NH_3$ gas bottle concentration used in this system was similar to that used for testing planar films.

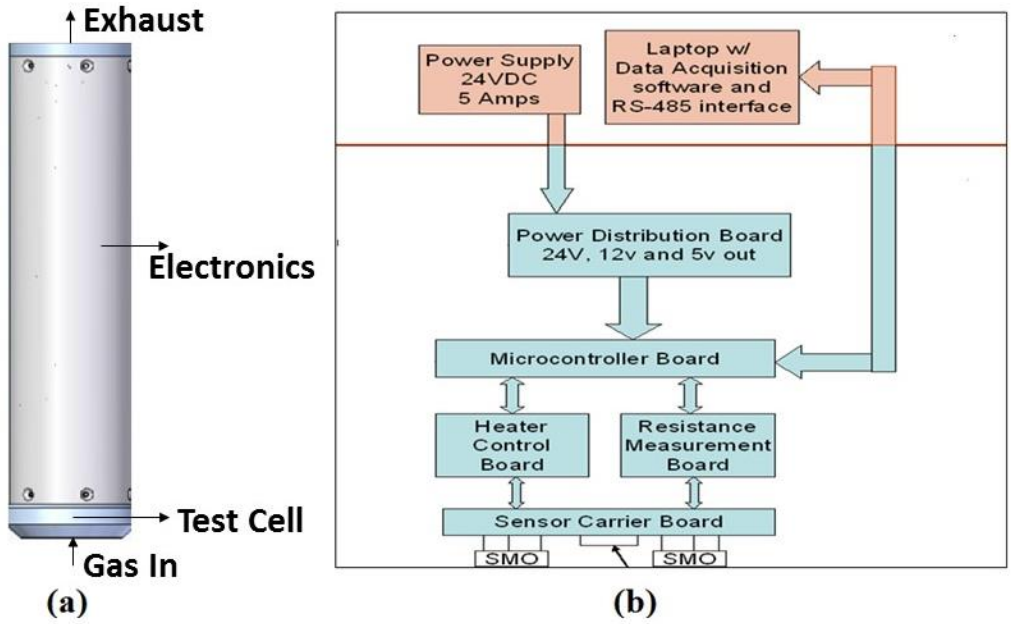


**Figure 4.14.** (a) Schematic of portable GDS system used for testing GLAD films. (b) Block diagram of the electronics housed in the portable system. Also shown is the external power supply and computer for measuring sensor response.

The GLAD sensor, like the planar film sensors, was also set to a temperature of 450 °C and allowed to stabilize for 2 hours with 150 sccm of air flowing through the test cell with 15% relative humidity. The sensor was then exposed to 200, 500, 100, and 600 ppb levels of $NH_3$ gas, respectively, with each exposure lasting 45 minutes. Once the exposures were completed, the $NH_3$ was turned off and the sensor was left to recover in 150 sccm flow of air. The effect of signal to noise ratio in measured resistance values (and in turn on conductivity) of planar and GLAD film sensors in the two gas delivery systems would be discussed in chapter 5.

### 4.5.1 Humidity Calibration

When performing gas testing, it was necessary to maintain a constant relative humidity in the test cell (at 15%) since the sensors responded to changes in humidity. A commercial humidity sensor was used for humidity calibration and to ensure the desired humidity level was maintained in the test cell of both systems. Figure 4.15 shows humidity calibration data with the actual humidity recorded by the commercial humidity sensor on the y axis against time on the x axis. The steps of 15, 20, 25 etc are the expected humidity percent values based on flow rates. If there was 100% saturation through the bubbler, the expected humidity would be closer to the actual value. But since this was not the case, the flow rates needed to be increased to get to the desired value of 15%.

Figure 4.16 shows the plot of expected humidity vs actual humidity. From this figure one can observe that the actual humidity was only 5% when the flow rates were adjusted for an expected humidity of 15%. Therefore to get humidity of 15% in the test cell, the flow rate was increased.

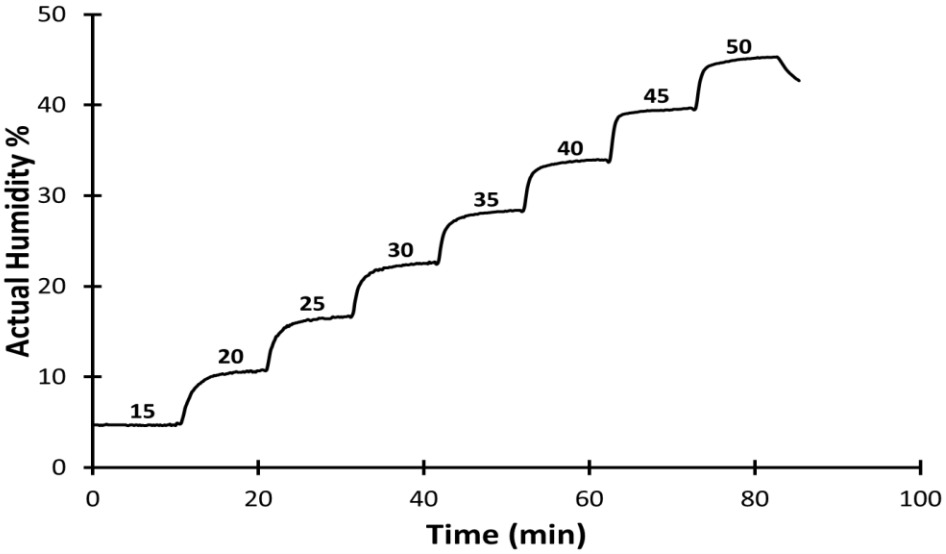


**Figure 4.15.** Humidity calibration data with actual humidity plotted against time. The number above each of the plateaus represent the calculated humidity levels based on flow rates.

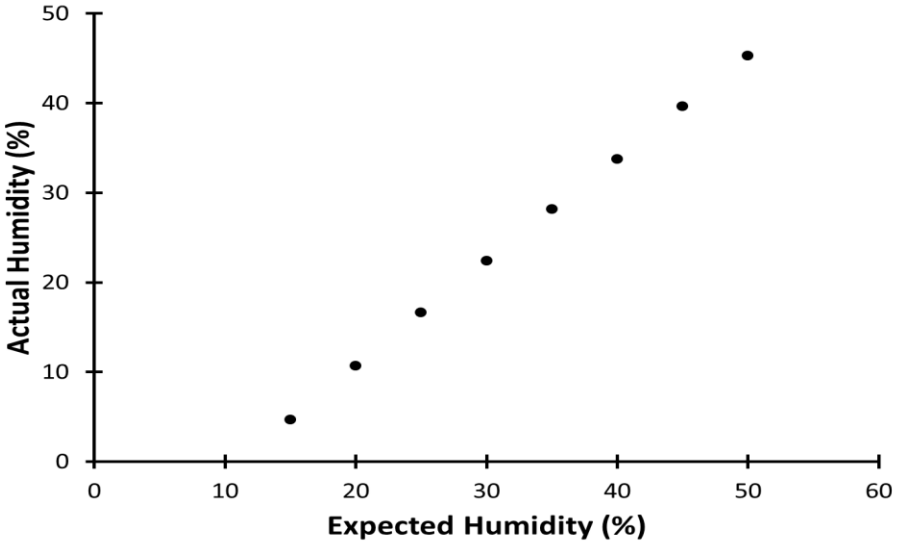


**Figure 4.16.** Plot of Expected Humidity based on flow rates vs Actual Humidity obtained using a commercial humidity sensor.

# 5. APPLICATION OF BULK CONDUCTIVITY MODELS TO $NH_3$ DETECTION USING $WO_3$ FILM GAS SENSORS

This chapter presents the gas chromatography/mass spectroscopy (GC/MS) and diffuse reflectance infrared fourier transform spectroscopy (DRIFTS) results of exposing both pure and 0.1% w/w Au loaded $WO_3$ powder catalyst to $NH_3$ gas in air at different temperatures. From the results, $H_2O$ and $N_2O$ were identified as possible reaction products. Based on this, balanced reaction equations are written for $NH_3$ gas interaction on Au doped planar and GLAD $WO_3$ film gas sensors. The experimental results for exposure of both Au doped $WO_3$ planar and GLAD film sensors to $NH_3$ gas at 450 °C were then compared to the bulk conductivity models, developed in chapter 3, to determine whether the sensor response was surface reaction limited or bulk diffusion limited.

## 5.1. Results of Powder Catalyst Characterization and Analytical Studies

### 5.1.1 Au loaded and Pure $WO_3$ Powder X-Ray Diffraction (XRD) Results

Figure 5.1 shows the XRD patterns of both 0.1% Au loaded and pure Aldrich 20μ $WO_3$ powder catalysts. The (122), (103), (310) and (131) monoclinic phase $WO_3$ peaks are clearly marked in the plot. We focus on a narrow 2θ range of 35-40° where the joint committee on powder diffraction standards (JCPDS) database indicates that Au (111) can be observed at a 2θ angle of 38.2°. From the plot, a weak peak at 38.2° is observed for the Au loaded sample but there is no visible peak at the same angle for the pure $WO_3$ sample. For monoclinic $WO_3$, from the JCPDS database, there are no observable peaks in the range of 37.4° to 38.8°. Therefore the peak at 38.2° is attributed to the presence of Au.

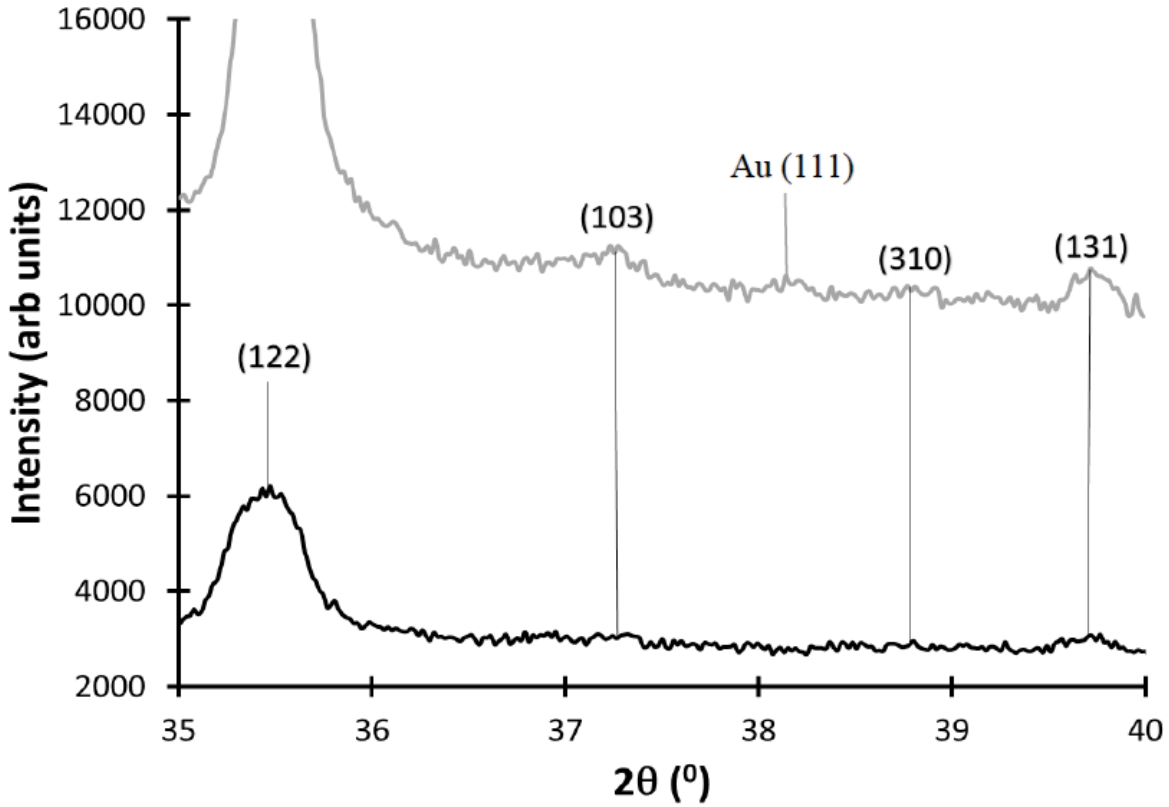


**Figure 5.1:** XRD diffraction pattern for Au loaded $WO_3$ (grey) and pure $WO_3$ (black) within a 2θ range of 35°- 40°.

The crystallite size of the Au particles in the catalyst was determined using the Scherrer equation, as described in chapter 4, where $\lambda$= 1.54 Å and $\theta$= 19.1°. The intensity of the Au peak is small as the loading is only 0.1% w/w and thus the signal to noise ratio is low. Therefore, to accurately determine the full width half maximum (FWHM), β, a Lorentzian fit was used within a 2θ range of 37.44° to 38.74°. Igor Pro 6.01 was used to determine the fit and figure 5.2 shows the XRD pattern of the Au loaded $WO_3$ along with the fit. β was estimated to be 0.0154 radians and using the Scherrer equation, we determined the crystallite size, *L*, to be approximately 9 nm.

LeGore et.al showed that Au deposited on $WO_3$ forms islands at lower temperatures and aggregates at temperatures above 400 °C and the growth mechanism is due to coalescence.[144]

Our XRD study was done on the Au loaded $WO_3$ catalyst after it was heated in the reactor at 450 °C with $NH_3$ gas flowing through it for a few hours. The actual size of the Au particles, prior to the temperature being increased in the microreactor, could have been much smaller than the determined 9 nm mentioned earlier.

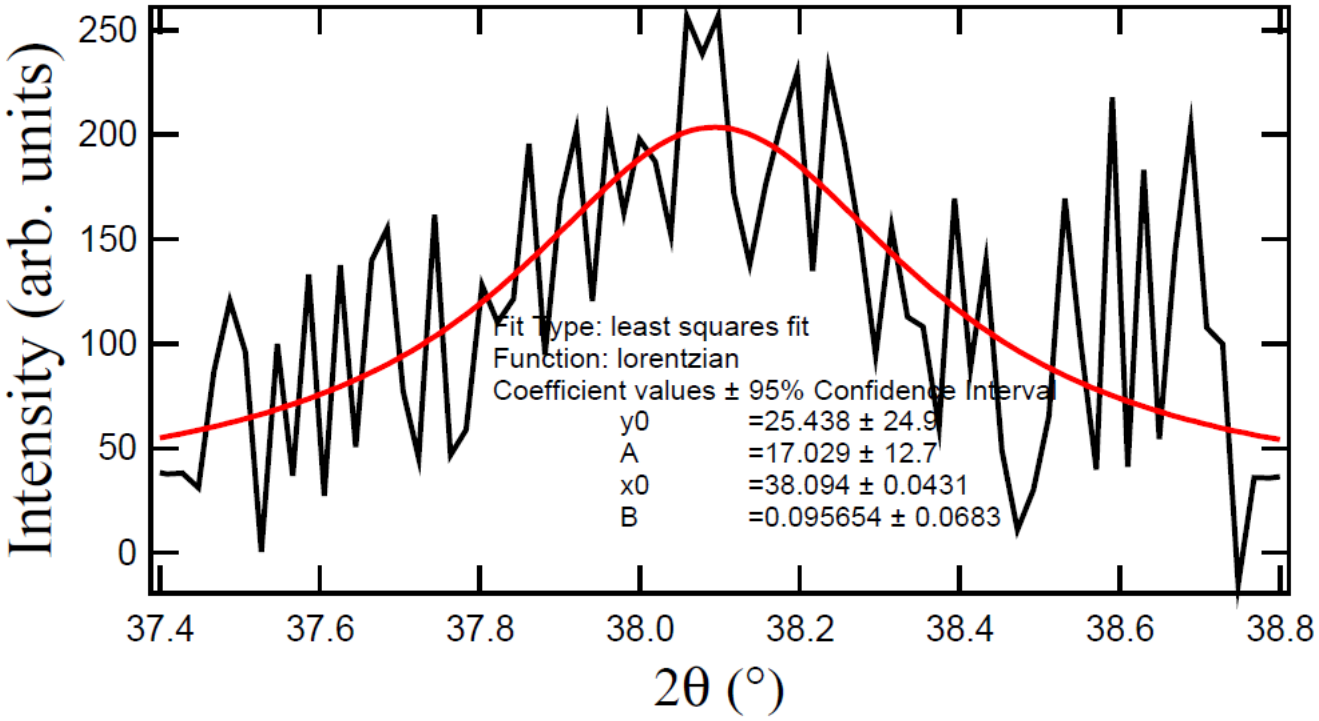


**Figure 5.2.** XRD pattern of the Au loaded $WO_3$ along with fit. The FWHM, β, was estimated to be approximately 0.0154 radians.

### 5.1.2 Results of GC/MS Study on Au loaded and Pure $WO_3$ Powder Catalysts to $NH_3$ gas at different temperatures

As mentioned in chapter 4, Au loaded and pure $WO_3$ catalysts were packed in separate glass tubes. $NH_3$ gas reaction on both samples was tested independently to obtain the reaction products, % conversion of $NH_3$ gas and % yield of the products.

At room temperature, the extracted ion chromatograms (EIC) for 17 ($NH_3$) and 18 ($H_2O$) m/z (mass to charge ratio) was examined for gas sampled downstream of the reactor packed with the $WO_3$ powder samples. The quantitation of the 17 m/z ion showed a peak with a retention time (RT) of 1.94 min while quantitation of the 18 m/z ion displayed two peaks where the second peak appeared on the tail of the $NH_3$ peak at 2.31 min. The fragmentation pattern (17, 16, 15) of the peak at 1.94 min was consistent with that of $NH_3$ and the fragmentation pattern (18, 17, 16) of the peak at 2.31 min was consistent with the fragmentation pattern of $H_2O$. The peak areas of the $NH_3$ and $H_2O$ peaks did not change between upstream and downstream sampling at room temperature (23 °C). The presence of small amounts of $H_2O$ upstream of the reactor was due to the presence of $H_2O$ in the airline. Nitrogen oxide (NO), nitrous oxide ($N_2O$) and nitrogen dioxide ($NO_2$) were not observed at this temperature.

The temperature in the reactor bed was then increased under a constant flow of 10 mol % of $NH_3$ gas in air and sampling was done both upstream and downstream of the reactor. Figure 5.3 (a) shows the variation of the $NH_3$ peak as a function of temperature. The area of the 17 m/z peak was used for quantification of $NH_3$. Although the peak area upstream of the reactor was constant, the ratio of the $NH_3$ peak area downstream to the peak area upstream of the reactor was plotted. From room temperature to about 150 °C, there is an increase in peak area ratio and then it starts to decrease. This being a continuous flow reactor, of the total $NH_3$ gas fed, a fraction of it adsorbs on the surface, decreasing the amount downstream at lower temperatures. The increase

in the peak area ratio at temperatures below 150 °C was attributed to desorption of $NH_3$ from Brønsted acid sites.[112] Ramis et al.[145] have reported that $NH_3$ is strongly adsorbed on Lewis acid sites on the $WO_3$ surface up to 400 °C. Figure 5.3 (b) shows the variation of the $H_2O$ peak area, relative to $NH_3$ fed, with respect to temperature. The area of 18 m/z peak was used for quantification of $H_2O$. From room temperature to 380 °C, the peak area remains relatively constant but once the temperature reaches 380 °C the peak increases gradually all the way to 450 °C. A peak was observed at 2.03 min for the 30 m/z ion at 380 °C which increased with reactor temperature. This peak was not observed in the blank air control experiments, where only air was passed over the catalyst at different temperatures, indicating that it was not produced in a gas phase reaction of $N_2$ and $O_2$. The fragmentation patterns of different $NO_x$ species, shown in table 5.1, were compared with the observed fragmentation pattern (44, 28, 30), which was consistent with the fragmentation pattern of $N_2O$.[143] The area of 30 m/z peak was used for quantification of $N_2O$ as the 28 m/z peak is also the molecular ion of $N_2$ and CO while 44 m/z peak corresponds to $CO_2$ gas if not separated chromatographically. Figure 5.3 (c) shows the variation of the 30 m/z peak area showing $N_2O$ yield with respect to temperature.

**Table 5.1.** Fragmentation patterns of NO, $N_2O$ and $NO_2$ along with relative peak intensity.[143]

| Gas | Fragmentation Pattern (relative peak intensity) | | | |
|---|---|---|---|---|
| NO | 30 m/z (100) | 14 m/z (90) | 15 m/z (20) | 16 m/z (10) |
| $N_2O$ | 44 m/z (100) | 30 m/z (30) | 28 m/z (10) | 16 m/z (6) |
| $NO_2$ | 30 m/z (100) | 46 m/z (38) | 16 m/z (22) | 14 m/z (6) |

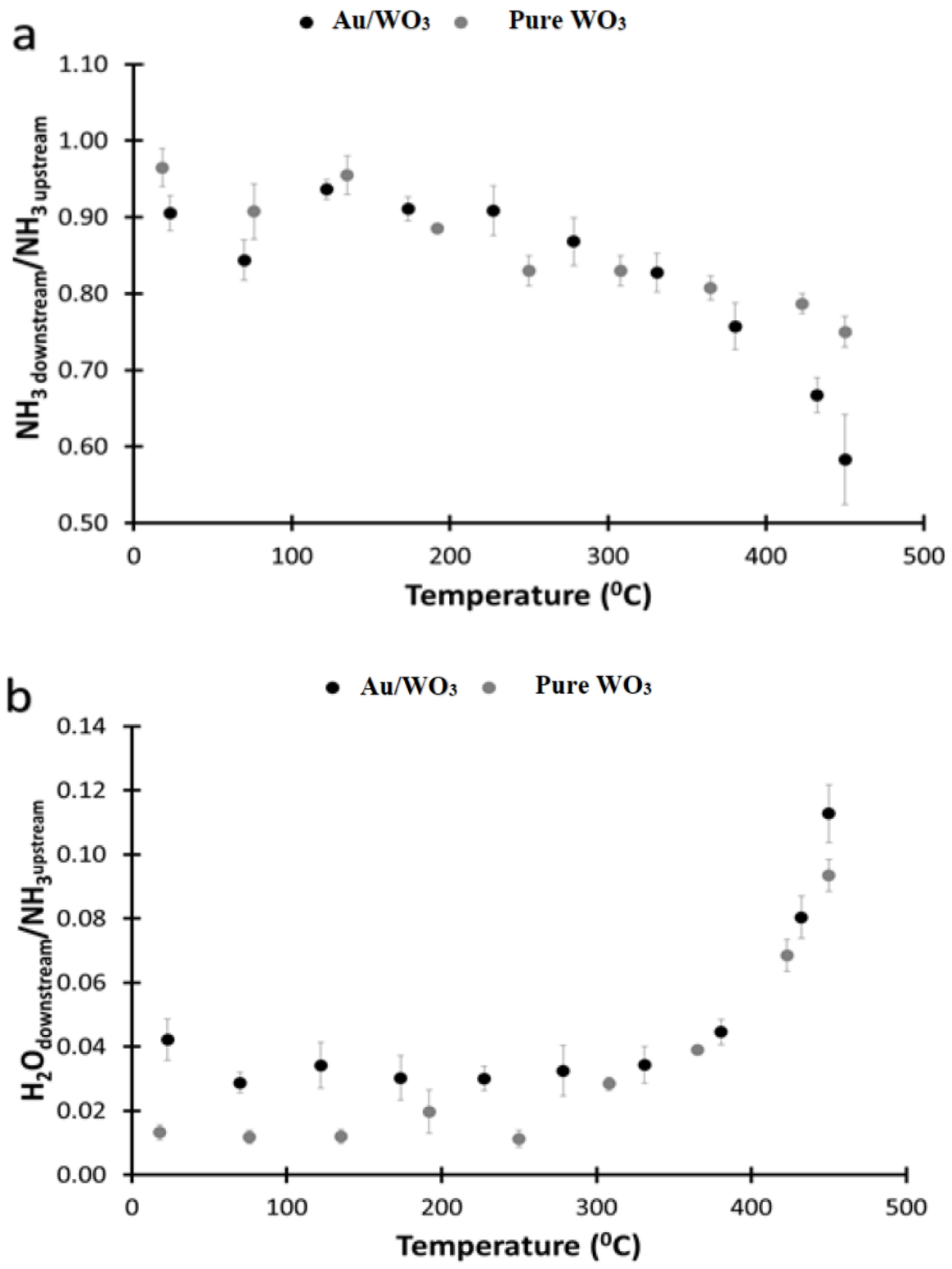


**Figure 5.3.** Ratio of downstream peak area to upstream $NH_3$ peak area of (a) $NH_3$ signal, (b) $H_2O$ signal

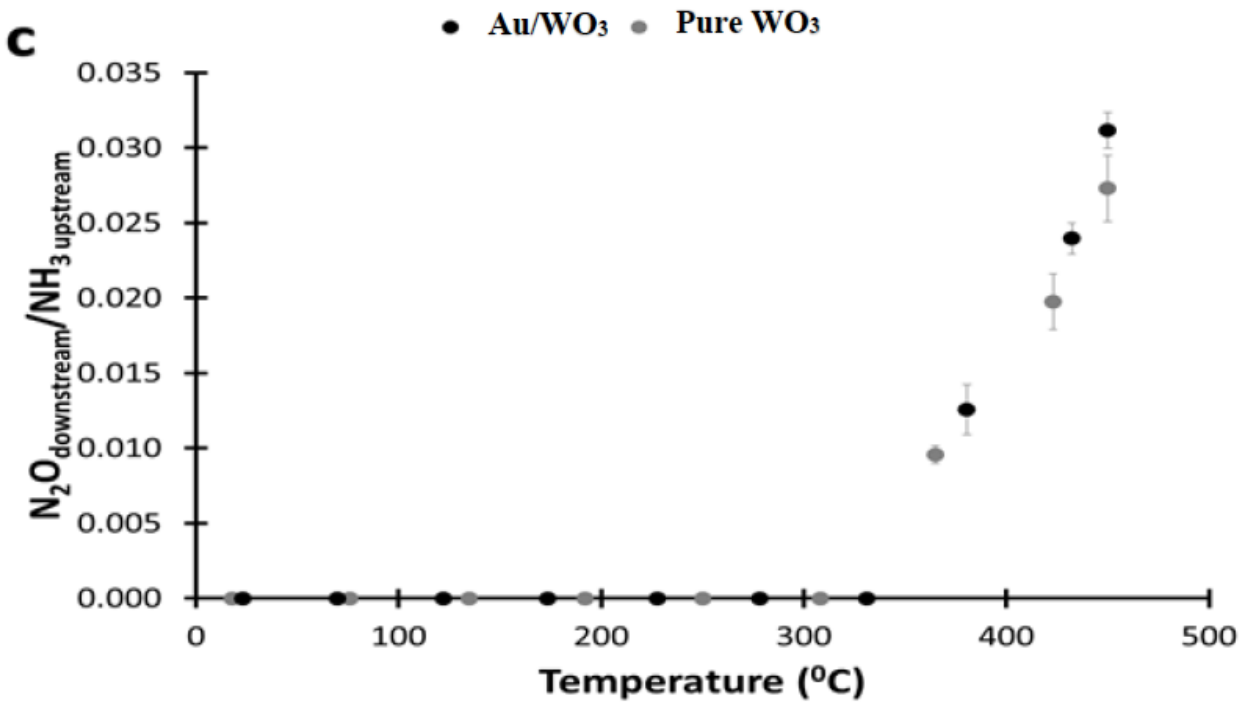


**Figure 5.3 continued.** and (c) $N_2O$ signal for Au loaded $WO_3$ and pure $WO_3$ powder catalysts. Error bars are also indicated.

Figure 5.3 illustrates how the $NH_3$ reaction on the $WO_3$ catalyst varied with temperature. The decrease in the ratio above 150 °C is attributed to a gradual increase in conversion ($\frac{Peak\ Area_{upstream} - Peak\ Area_{downstream}}{Peak\ Area_{upstream}} \times 100\%$) with temperature on both catalysts. Above 350 °C, the conversion on the Au loaded $WO_3$ became greater than for the pure $WO_3$ support. At 450 °C, the conversion of $NH_3$ was approximately $40 \pm 5\%$ for the Au loaded $WO_3$ catalyst and $23 \pm 2\%$ for the pure $WO_3$ catalyst. This indicates that the presence of Au played a role in the $NH_3$ reaction on the Au loaded $WO_3$ catalyst. Similarly, the yield of $H_2O$ and $N_2O$ was also slightly higher for the Au loaded $WO_3$ catalyst in the range $350\ °C \leq T \leq 450\ °C$. For the Au loaded $WO_3$ catalyst, at 450 °C, the yield of $H_2O$ is approximately 25% of the amount of $NH_3$ converted, while the $N_2O$ signal was only 7.5% of the $NH_3$ converted. This could be due to

difference in detector sensitivity to $N_2O$ and $H_2O$. However, there can also be other products formed as a result of $NH_3$ reaction on $WO_3$ surface. One possibility is that $NH_3$ could be reacting to form $N_2$ on the catalyst surface. Since air (78% $N_2$) is also fed into the catalyst bed along with $NH_3$, it is difficult to determine whether $N_2$ was produced from $NH_3$ gas as there was a high concentration of $N_2$ gas already present in the catalyst bed. Another possibility could be formation of an oxynitride, based on the work done by Volpe and Boudart,[146-147] where the reaction of $NH_3$ gas with $MoO_3$ at high temperatures (300 °C – 700 °C) resulted in $Mo_2N$ formation. Being a reducible metal oxide like $MoO_3$, a similar reaction can happen in $WO_3$ as a result of $NH_3$ interaction to form $W_2N$. Ruiz et al.[148] prepared $W_2N$ from $WO_3$ in a quartz tube under flowing ammonia by heating from ambient to 300 °C at 9.3°C/min, then to 500°C at 0.6 °C/min, and then to 700 °C at 2 °C/min and holding for 2 hours, yielding pure $W_2N$, as characterized by XRD. XRD, in this study, did not shown any nitride formation but this was done after the catalyst was cooled in air, which can cause the catalyst to revert back to being $WO_3$. Neither NO or $NO_2$ was observed as a product of the reaction, although it has been reported that NO desorption takes place at over 570 °C for $WO_3$ catalysts.[112]

Using the % conversion value, molar flow rate and surface area of the catalyst, the reaction rate and, in turn, reaction rate constant associated with $NH_3$ reaction on the catalyst can be estimated. Surface area for the 20 μ powder is $S_A = 1.7\ \frac{m^2}{g}$ and the total weight of catalyst used in the reactor is $W_{WO_3} = .5\ g$. Therefore total area $A = S_A \times W_{WO_3} = .85\ m^2 = .85 \times 10^{18}\ nm^2$. The molar flow rate, $F$ ($F = \left(\frac{n}{t}\right) = \frac{P}{RT}\frac{V}{t}$), was calculated to be $3.27 \times 10^{18}\ \frac{1}{s}$. Reaction rate, $r = \frac{1}{A} \times F \times C_P$, where $C_P = 0.35$ is the $NH_3$ conversion for the Au loaded $WO_3$ catalyst and $C_p = 0.25$ for the pure $WO_3$ catalyst at $450^0$C. The first order reaction rate was

calculated to be approximately 1.3 $\frac{1}{nm^2\ s}$ and 1.0 $\frac{1}{nm^2\ s}$ for the Au loaded and pure $WO_3$ catalysts respectively. However, these calculations did not take into account uncertainties due to variations in flow rates and upstream pressure. The uncertainty in flow rate due to the error (of about 10%) associated with the MFCs can affect reaction rate calculations. Another factor that influences rate calculations is the pressure measured upstream of the reactor. As the reactor temperature increases, the viscosity of the gas also increases and this results in a pressure build up at the base of the reactor. This could affect the total number of moles of $NH_3$ gas reaching the reactor bed and in turn affect the calculation of rate and rate constants.

The reaction products as well as approximate reaction rates were obtained from GC/MS results, but in order to better understand the adsorption sites and the thermal behavior of $NH_3$ molecules, DRIFTS was done on both the catalysts.

### 5.1.3 Results of DRIFTS Study on Au loaded and pure $WO_3$ Powder Catalysts to $NH_3$ gas at different temperatures

Figure 5.4 shows $NH_3$ adsorbed from a 1000 sccm 10% $NH_3$/Ar flow on the surface of the pure $WO_3$ at room temperature. Both Au loaded $WO_3$ and pure $WO_3$ were pretreated with 1000 sccm synthetic air flow at 400 °C for several hours before adsorption. Because this is a difference spectrum, positive going peaks show vibrational modes associated with adsorption of $NH_3$ on the catalyst surface and negative going peaks indicate vibrational modes that were removed, shifted or decreased in intensity after $NH_3$ adsorption. Two negative bands at 1871 $cm^{-1}$ and 2063 $cm^{-1}$ were assigned to the W=O overtones where the negative bands at these frequencies showed a decrease in their intensity.[112, 145, 149] This decrease in the intensity was because of the $WO_3$ reduction due to $NH_3$. After adsorption of $NH_3$ at room temperature over

pure $WO_3$ catalyst, positive bands appear at 3394, 3309, 3165,1610,1268, and 1222 (adsorbed $NH_3$ on Lewis acid sites), and at 3255,3203, 1473 and 1382 $cm^{-1}$ (adsorbed $NH_4^+$ on Brønsted acid sites).[112] Symmetric deformation of coordinated $NH_3$ caused 1268 $cm^{-1}$ and 1222 $cm^{-1}$ peaks. Similar peaks were observed for the Au loaded $WO_3$ catalyst as well. Peaks corresponding to the $NH_3$ oxidation products were not observed at this temperature.

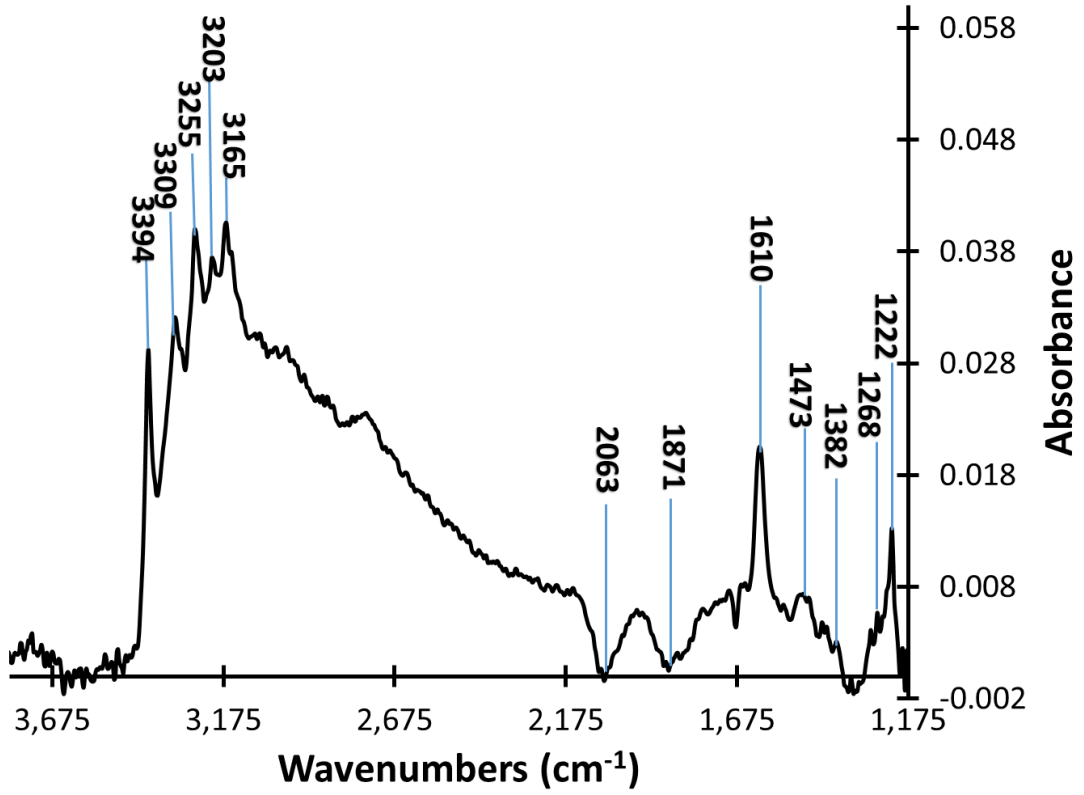


**Figure 5.4.** DRIFTS difference spectra of $NH_3$ adsorbed on the pure $WO_3$ surface (Spectrum of the surface after $NH_3$ adsorption subtracted from the spectrum of the surface before adsorption) recorded at the room temperature under synthetic air atmosphere.

Figure 5.5 shows spectra of $NH_3$ adsorbed at room temperature on the pure $WO_3$ sample and then the temperature was increased to 100 °C and 200 °C. All the spectra were referenced to the singe beam recorded at the same temperature to remove the thermal effect of the spectra. It was observed that the broad IR electronic signal (background) also increased with temperature as

a result of optical transitions of localized electrons to the conduction band, caused by n-doping of $WO_3$ due to $NH_3$.[150] It was also observed from the figure that as the temperature increased, intensity of negative bands at 1871 $cm^{-1}$ and 2063 $cm^{-1}$ assigned to the W=O overtones also increased.[145, 149] These changes are indicative of the increase in $WO_3$ surface reduction due to $NH_3$. Comparing the spectra at 25 °C, 100 °C, and 200 °C, it was observed that 3255, 3203, 1473 and 1382 $cm^{-1}$ peak intensities decreased at 100 °C and completely disappeared at 200 °C. This was due to the weak $NH_3$ interaction with Brønsted acid sites at this temperature.[112] At 200 °C, the intensity of most of the positive bands falls off as the number of adsorbed $NH_3$ molecules on the surface is lower.

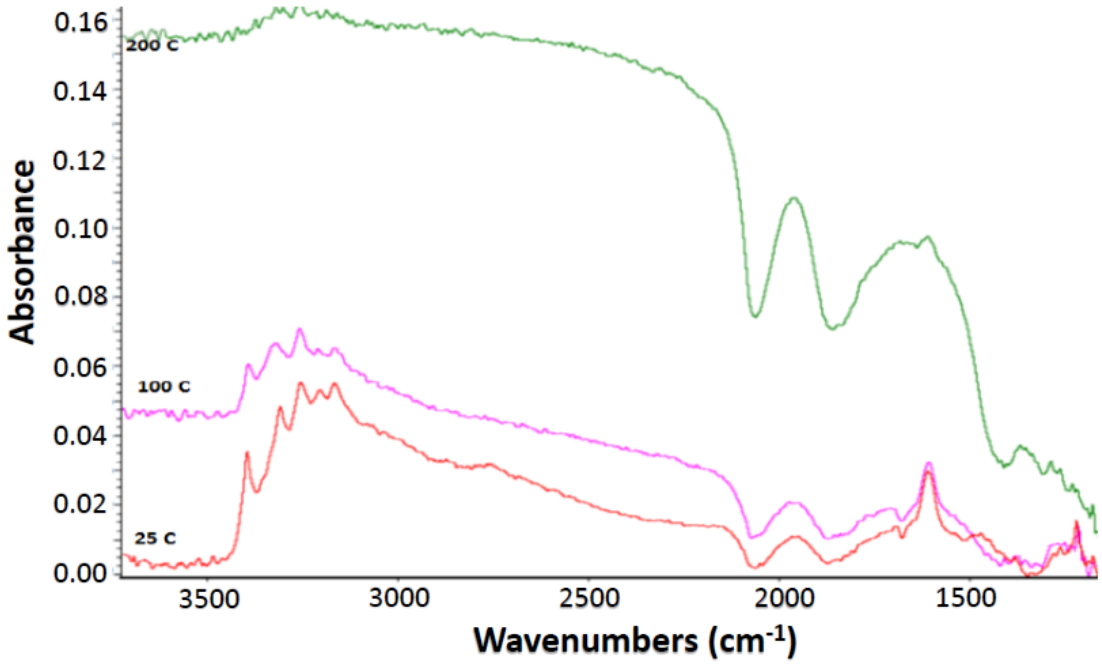


**Figure 5.5.** DRIFTS difference spectra of $NH_3$ on the $WO_3$ surface at 25 °C, 100 °C and 200 °C. Single beams were recorded at the corresponding temperatures in the air atmosphere. $NH_3$ was adsorbed on the $WO_3$ surface from a flow system, the gas was switched to air and after 10 min a spectrum was recorded at each temperature.

Figure 5.6 shows temperature effect on the reaction between pure $WO_3$ and $NH_3$ gas. The reaction chamber environment was switched back and forth between 10% $NH_3$/Ar atmosphere and synthetic air atmosphere, at 150 °C, 200 °C and 300 °C, and spectra were recorded immediately after changing the environment. The difference spectra was referenced to the single beam of pretreated pure $WO_3$ before exposure to $NH_3$. The negative bands at 1871 $cm^{-1}$ and 2063 $cm^{-1}$ were more intense and the background was higher for the $NH_3$ atmosphere compared to the air atmosphere. These differences became more significant as the temperature was increased. The gap between the backgrounds in the air atmosphere and the background in the $NH_3$ atmosphere was indicative of the degree of reduction of the surface by $NH_3$ and this gap increased with temperature. As the $WO_3$ was reduced to a lower oxidation state, there was an increase in the conductivity and a decrease in the optical transparency. Besides temperature, the time of exposure to $NH_3$ was another factor influencing the spectrum background and the intensity of the negative bands at 1871 $cm^{-1}$ and 2063 $cm^{-1}$. Figure 5.7 shows the difference spectra of the pure $WO_3$, at 300 °C, as a function of the exposure time to $NH_3$. All the spectra were referenced to the single beam spectrum of pure $WO_3$ in the air atmosphere. The background was increased and negative bands at 1871 $cm^{-1}$ and 2063 $cm^{-1}$ were more intense for the longer exposure time. Similar observations can be made for Au loaded $WO_3$. The difference between the recorded spectra shown in figure 5.7 and that observed at 300 °C shown in figure 5.6, was that signal to noise ratio was better for figure 5.6 and the peaks corresponding to $NH_3$ adsorbed on Lewis acid sites (3394, 3309, 3165 $cm^{-1}$) were not seen in figure 5.7. This could be possible since the two spectra were recorded with different $WO_3$ and KBr loading.

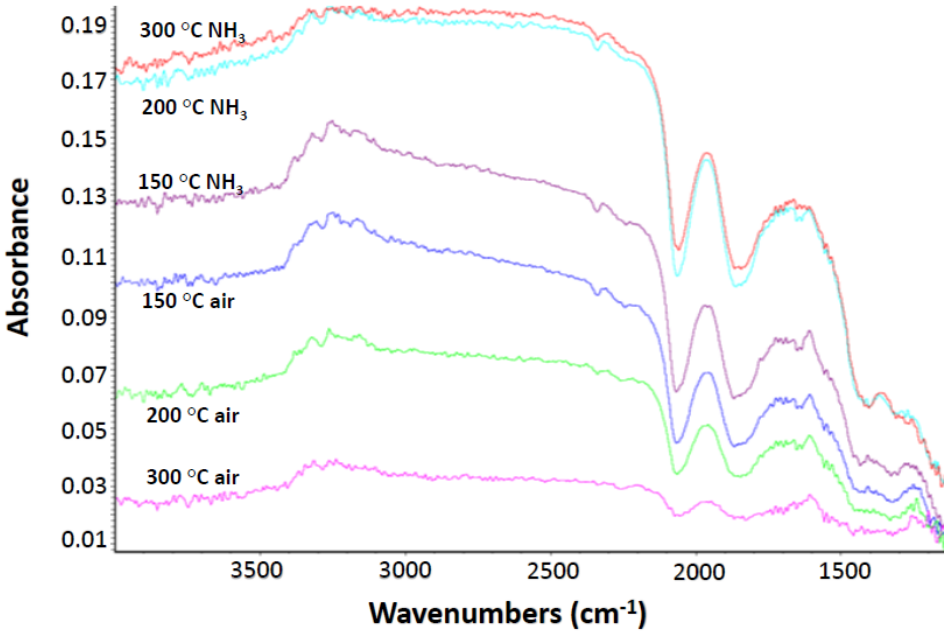


**Figure 5.6.** Spectra showing $NH_3$ atmosphere vs air atmosphere for pure $WO_3$ at 150 °C, 200 °C and 300 °C.

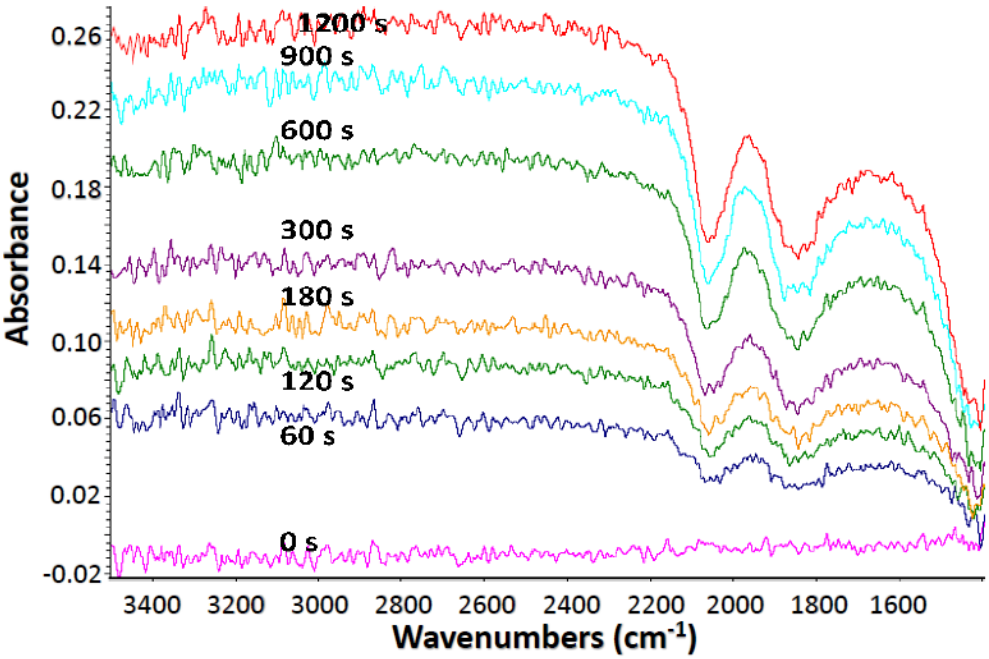


**Figure 5.7.** Spectra of $NH_3$ atmosphere from air atmosphere at 300 °C on the surface of pure $WO_3$ as a function of exposure time.

Figure 5.8 shows the peak area of the negative band at 2063 $cm^{-1}$ for pure $WO_3$ as a function of exposure time to $NH_3$. For the first 300 sec, the change in the intensity of the negative band at 2063 $cm^{-1}$ with respect to time is linear and the rate by which the peak area is changing as a function of time can be calculated from the slope of the graph. The change in peak area with time is an exponential decay, given by $0.3 - 0.3\ e^{-0.0018t}$, which is similar to a first order rate law.

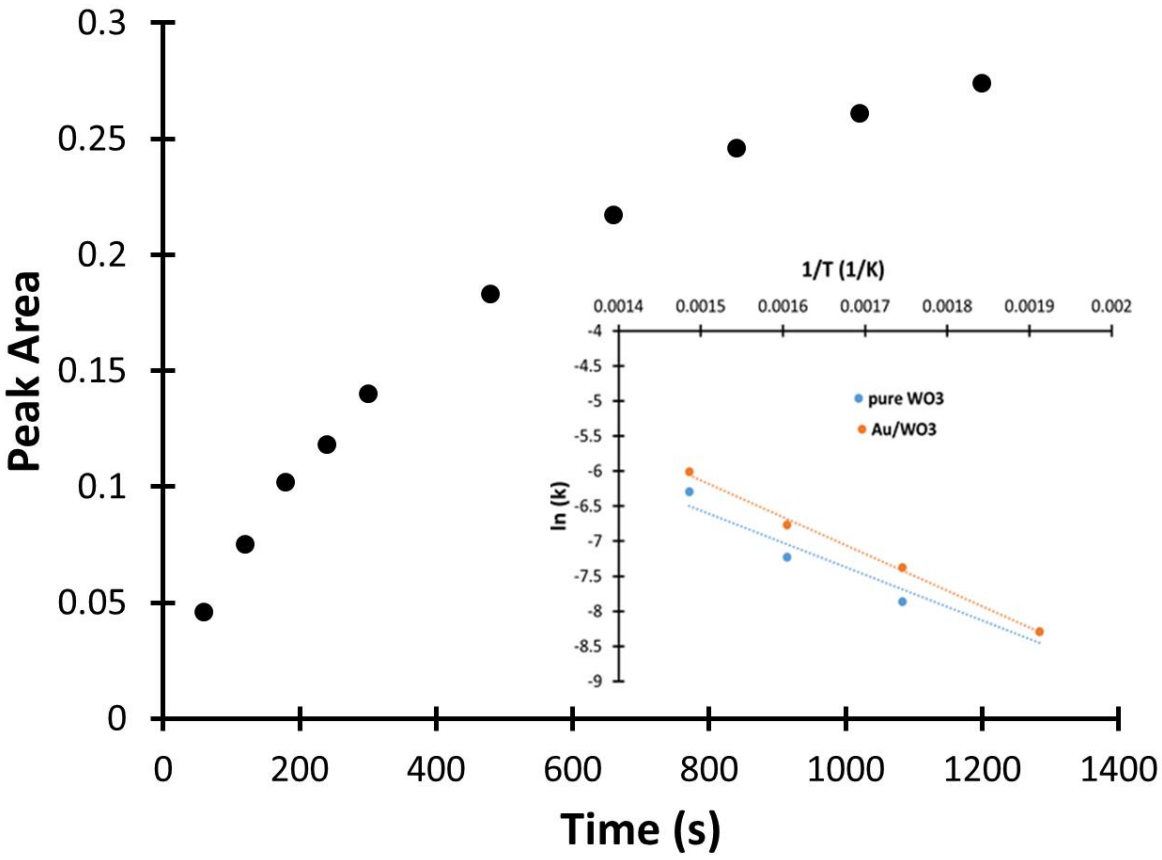


**Figure 5.8.** Peak area of the band at 2060 $cm^{-1}$ as a function of the exposure time of pure $WO_3$ to $NH_3$. Arrhenius plots for activation energy of Au loaded and pure $WO_3$ catalysts are also plotted.

Table 5.2 gives the initial slope of the data plotted in figure 5.8 which is proportional to the $NH_3$ reaction rate for both pure $WO_3$ and Au loaded $WO_3$ at different temperatures. At 250 °C the reaction rate for both pure $WO_3$ and Au loaded $WO_3$ was found to be the same but as the temperature was increased to 300 °C and above, the reaction rate of the Au loaded $WO_3$ was found to be higher than that of the pure $WO_3$ catalyst. The activation energy for the Au loaded $WO_3$ catalyst was calculated to be about $43\frac{KJ}{mol}$ while that of the pure catalyst was calculated to be about $38\frac{KJ}{mol}$ as shown in figure 5.8.

**Table 5.2.** Initial slope of peak area of the band at 2060 $cm^{-1}$ vs temperature. This is proportional to reduction rate constant at which peak area of the band at 2060 $cm^{-1}$ is changing with respect to exposure time for both pure $WO_3$ and Au loaded $WO_3$ to $NH_3$ flow.

| | 250 °C | 300 °C | 350 °C | 400 °C |
|---|---|---|---|---|
| Pure $WO_3$ | $2.50 \times 10^{-4}\ \frac{area}{time}$ | $3.85 \times 10^{-4}\ \frac{area}{time}$ | $7.25 \times 10^{-4}\ \frac{area}{time}$ | $1.85 \times 10^{-3}\ \frac{area}{time}$ |
| Au/$WO_3$ | $2.50 \times 10^{-4}\ \frac{area}{time}$ | $6.25 \times 10^{-4}\ \frac{area}{time}$ | $1.15 \times 10^{-3}\ \frac{area}{time}$ | $2.45 \times 10^{-3}\ \frac{area}{time}$ |

From the GC/MS study, $N_2O$ and $H_2O$ were determined to be the reaction products formed as a result of $NH_3$ reaction on Au loaded and pure $WO_3$ powder catalysts at temperatures greater than 350 °C. % conversion of $NH_3$ gas and % yield of $N_2O$ and $H_2O$ were also determined from the experimental results. It was observed that % conversion on Au loaded $WO_3$ powder catalyst was higher than on pure $WO_3$ powder catalyst. Based on the % conversion of $NH_3$ gas, reduction rate constants as a result of $NH_3$ reaction on both Au loaded and pure $WO_3$ samples at 450 °C (sensor operating temperature) were mathematically determined to be 1.3

$\frac{1}{nm^2\ s}$ and 1.0 $\frac{1}{nm^2\ s}$. Drifts data complemented the results of the GC/MS data, as it also indicated that $NH_3$ reacts faster on Au loaded $WO_3$ powder catalyst at temperatures greater than 300 °C than on pure $WO_3$ powder catalyst. Also from the DRIFTS study, by plotting the peak area of the band at 2063 $cm^{-1}$ as function of time, it was determined that $NH_3$ reaction on $WO_3$ powders is a first order reaction.

### 5.2. Application of Bulk Conductivity Models

In this section, the behavior of the models are utilized to distinguish between bulk conductivity from the band bending mechanism and also differentiate between surface reaction limited and bulk vacancy diffusion limited cases using actual experimental data. The roles of the various parameters in determining gas sensing mechanism of SMO film sensors are also determined. As an example, gold (Au) doped planar and GLAD tungsten trioxide ($Au/WO_3$) film sensors were tested against ppb concentrations of $NH_3$ gas.

#### 5.2.1. Response of Planar $WO_3$ film sensors to ppb Level Concentrations of $NH_3$ Gas

The film conductivity, σ,

$$\sigma = \frac{X}{6wLR}, \tag{5.1}$$

where $X$ is the distance between the electrodes (.3 mm), $w$, is the width of the film (3 mm), $L$, is the thickness of the film and $R$ is the film resistance. The sensor platform was designed with an interdigitated electrode structure and therefore a factor of 6 arises from the equivalent circuit involving 6 sensing film segments in parallel.[151]

Both 125 nm and 250 nm $Au/WO_3$ planar film sensors had a significant amount of baseline drift even after hours of equilibration at operating conditions. This was also observed in

a 250 nm planar film. The baseline conductivity drift affects the calculation of $\Delta\sigma$. For calculating the steady state baseline conductivity values in both 125 nm and 250 nm films, an exponential function was used to fit a curve to the sensor response data. The steady state baseline conductivity for 125 nm and 250 nm films were approximately $5\times 10^{-3}\ \frac{1}{\Omega\ cm}$ at 450 °C. The baseline fit was then subtracted from the measured values to more accurately estimate $\Delta\sigma$. Figure 5.9 shows magnitude of conductivity, Δσ, of the 125 nm planar film sensor, to ppb levels of $NH_3$ gas. The ppb dose levels of $NH_3$ gas, as a function of time, is also illustrated in the figure. Although the $NH_3$ dose curve is shown as a step response, previous characterization of the test cell response has shown that the concentration in the test cell varied slower due to the effects of dead volume, which will be discussed later in the chapter. Similarly figure 5.10 shows the Δσ calculations for the 250 nm planar film.

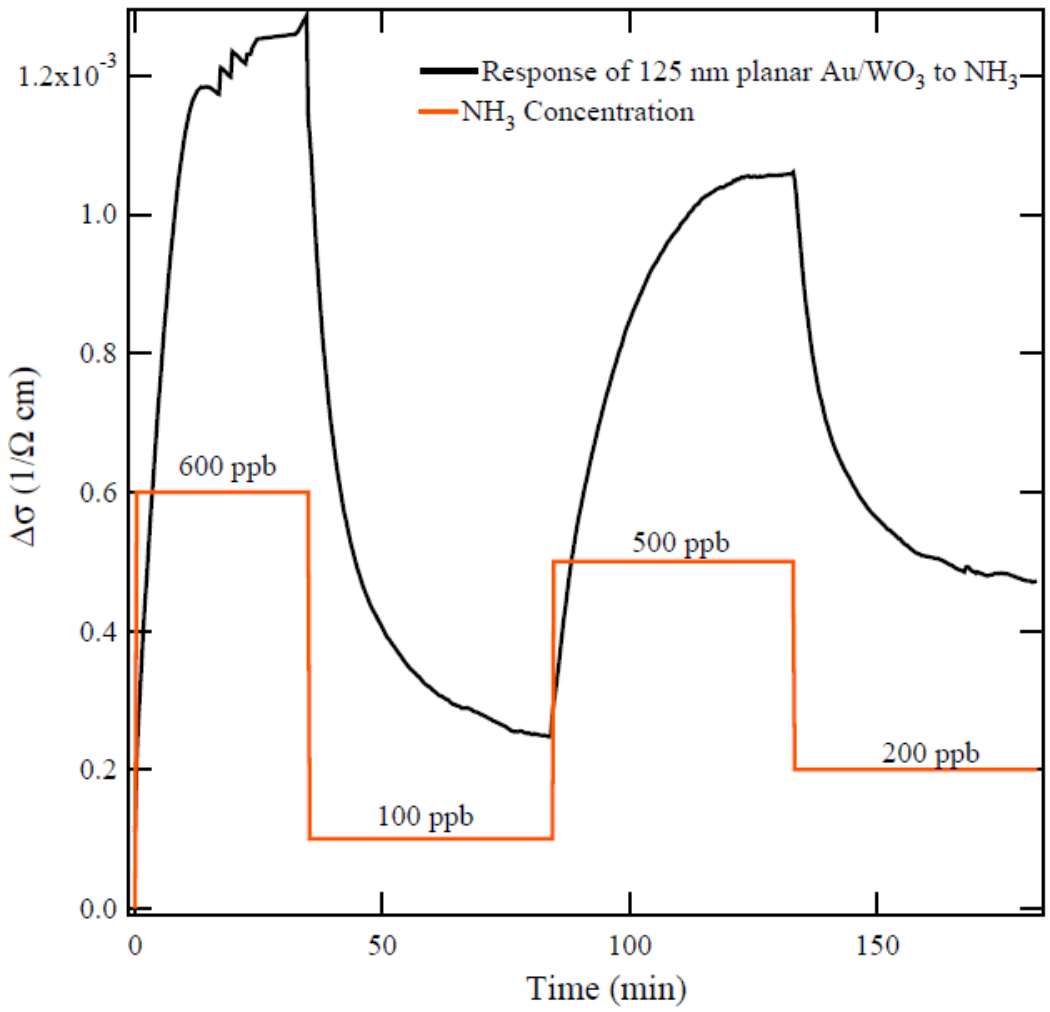


**Figure 5.9.** Δσ of 125 nm $Au/WO_3$ planar film to ppb levels of $NH_3$ gas.

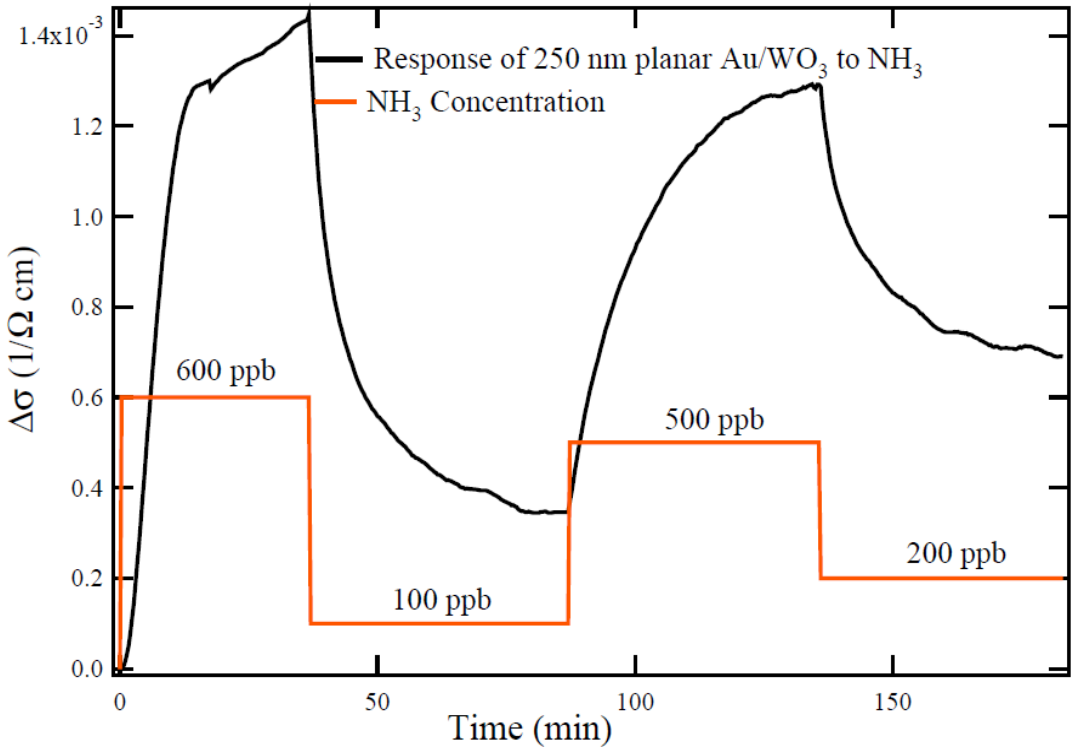


**Figure 5.10.** Δσ for the 250 nm $Au/WO_3$ planar film to ppb concentrations of $NH_3$ gas.

Note that fabricating uniform continuous films becomes increasingly difficult for thinner films, as reported by Legore et.al.[26] Their SEM images of thin $WO_3$ films grown with the same system showed that as film thickness decreases, it becomes highly discontinuous and therefore, the baseline conductivity in very thin films should be anomalously low even if the transduction mechanism in these films are similar to that of thicker films. A 50 nm $Au/WO_3$ planar film was also tested along with the 125 nm and 250 nm $Au/WO_3$ planar films to the same ppb concentrations of $NH_3$ gas. But since the 50 nm $Au/WO_3$ planar film had an apparent baseline conductivity which was lower than the baseline conductivity of 125 nm and 250 nm planar films by about 90% due to discontinuities in the film, reproducibility of sensor response becomes a major issue in these films and thus would not be used for modeling in this thesis.

### 5.2.2. Response of $WO_3$ GLAD Film Sensor to ppb Level Concentrations of $NH_3$ Gas

Steeves et al.[123] showed using Van der Pauw and Hall Effect measurements that conductivity in GLAD films was dominated by a thin polycrystalline layer underneath the nanorods. The thickness of the polycrystalline layer for the GLAD film shown here was determined from equation 5.1 using the baseline conductivity of the planar films ($5\times 10^{-3}\ \frac{1}{\Omega\ cm}$) under the assumption that the baseline conductivity was the same irrespective of film thickness. The polycrystalline layer film thickness was calculated to be approximately 6.4 $nm$. Figure 5.11 shows the time dependence of Δσ of the 100 nm GLAD Au/$WO_3$ film sensor on ppb levels of $NH_3$ gas after adjusting for baseline drift.

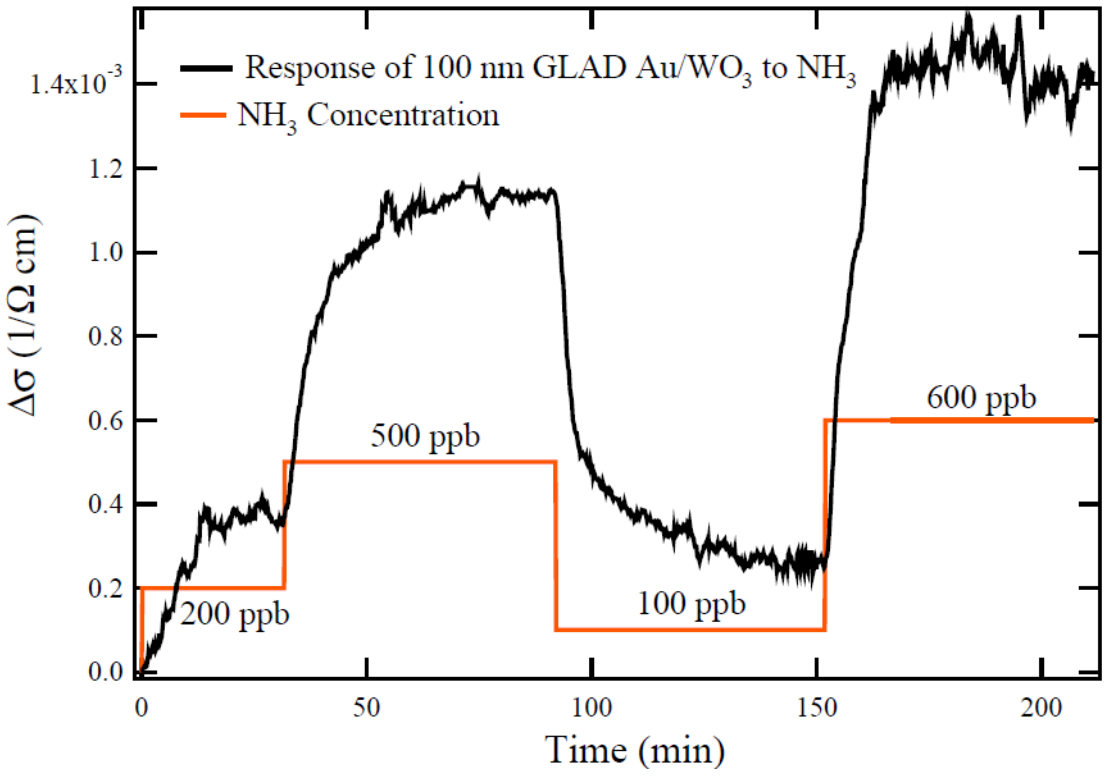


**Figure 5.11.** Change in Δσ of 100 nm GLAD $WO_3$ film to ppb levels of $NH_3$ gas.

### 5.2.3. Distinction between Band Bending Mechanism and Bulk Conduction Mechanism

The qualitative characteristics predicted by the model described in chapter 3, and summarized in Table 5.3, provide factors to differentiate experimentally between the bulk conduction and band bending transduction mechanisms.

**Table 5.3.** Characteristic behavior of the Band Bending vs. Bulk Conduction models.

| Characteristic | Band Bending | Bulk Conduction | |
|---|---|---|---|
| | | Surface Reaction Limited | Diffusion Limited |
| Magnitude of response vs. concentration of target gas. | Depends on analyte; $\frac{\sigma}{\sigma_0} \propto P^z$, where z = 0.3-0.6 have been shown, and z is less than order of reaction in target gas. | Depends on analyte; $\Delta\sigma \propto P^b$, where b is order of the rate in target gas or 3b/2. | |
| Magnitude of response vs. film thickness | $\Delta\sigma$ decreases with increasing thickness if depletion layer width is too thin to modulate entire film. | Magnitude of $\Delta\sigma$ is independent of film thickness. | |
| Functional dependence of step response to target gas vs. time | Transient response of surface reactions and effect of surface potential barrier on rate of adsorption of ionic species gives $\Delta\sigma \propto (1 - e^{-t/\tau})$ | Psuedo-first order reaction in lattice oxygen gives exponential behavior $\Delta\sigma \propto (1 - e^{-t/\tau})$ | Determined by solution to diffusion in finite film. $\Delta\sigma \propto t^{1/2}$ for $t \leq .3\frac{D}{L^2}$, then saturates. |
| Response time, $\tau$, vs. film thickness | $\tau$ is independent of film thickness | $\tau$ increases proportional to volume/area ratio (e.g. film thickness). | Increases proportional to square of film thickness. |

The magnitude of the response to $P\ (NH_3)$ in air at 450 °C as a function of $NH_3$ concentration is shown for three different sensors in figure 5.12. The dependence on $NH_3$ concentration, $\Delta\sigma = SP^b$, was determined from a weighted non-linear least squares fit to be $b$ = *0.91, 0.96,* and *1.1* for the 125 nm planar, 250 nm planar, and 100 nm GLAD films, within 95% confidence intervals based on the individual sensor uncertainties in $\Delta\sigma$ and $P(NH_3)$. The sensitivity, *S*, is the slope, $d(\Delta\sigma)/dP$, which is not significantly dependent of the *V/A* ratio. For these conditions, where $K_t < K$, $b$ corresponds to a rate law that is 1st order in $NH_3$ within the bulk conduction model. Within the band bending model, the exponent typically varies between 0.3-0.6,[31] so a value of $b = 1$ suggests that the band bending mechanism is not likely. Conversely, ½ order dependence on target gases, such as dissociative adsorption of $H_2$, could result in $b = 0.5$ within the bulk conduction model and therefore the order is not a definitive indication of the mechanism. The data is re-plotted in the inset of figure 5.12 vs. the volume to area ratio, where the error bars represent an estimate of the sensor to sensor reproducibility. Within the uncertainty, there is no dependence of $\Delta\sigma$ on V/A, which is consistent with the bulk conduction model. For the band bending model, the magnitude of $\Delta\sigma$ depends on the Debye length (estimated to be 50 nm) relative to the film thickness. The variation in film thickness from the GLAD film, in which the base layer is 6.4 nm, to the 250 nm planar film indicates that there should be a substantial decrease in $\Delta\sigma$ over this range if band bending were important.

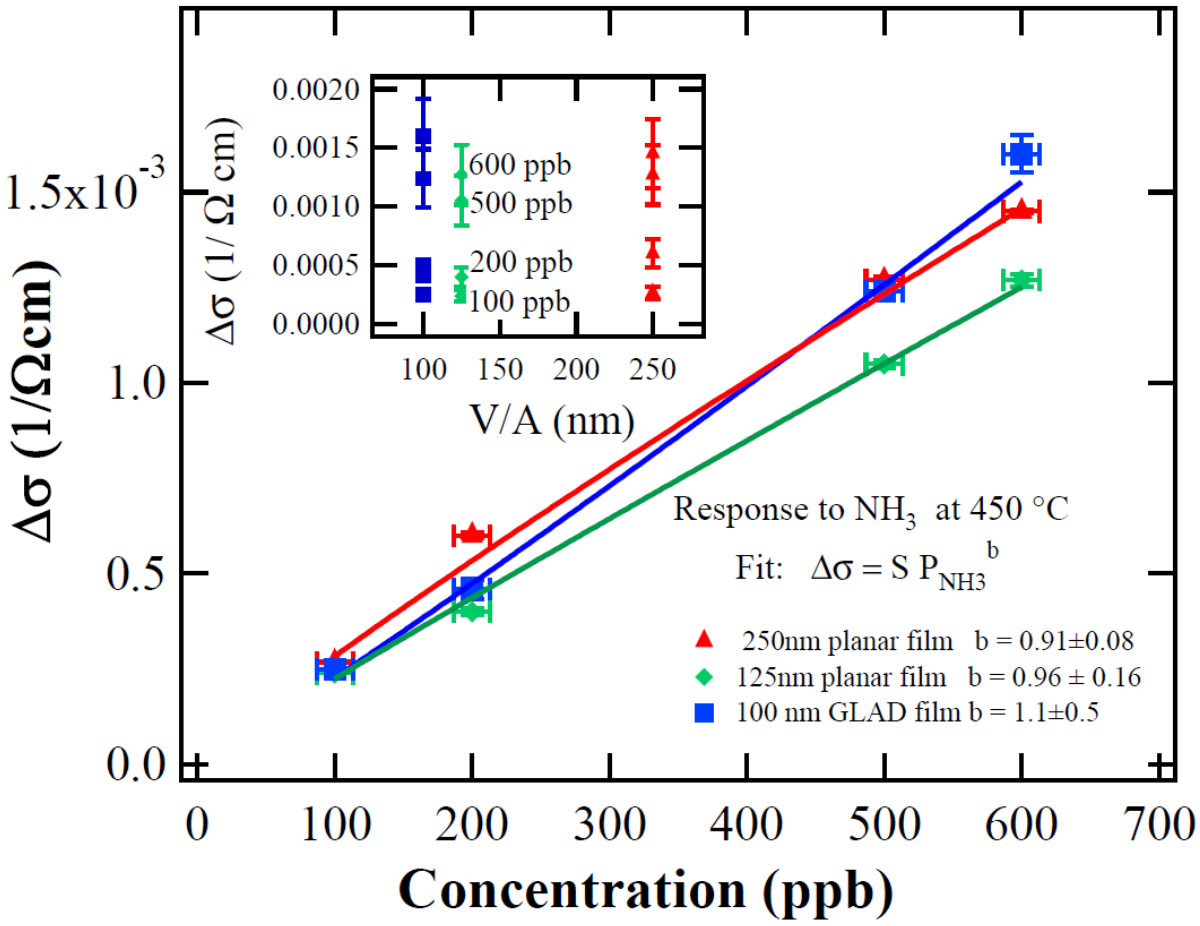


**Figure 5.12.** Power law fit of response of Au/$WO_3$ films vs. $NH_3$ concentration showing 1st order dependence. Inset: Data replotted as $\Delta\sigma$ vs. volume/surface area ratio showing that, within sensor-to-sensor reproducibility, $\Delta\sigma$ is independent of V/A.

### 5.2.4. Distinction between Surface Reaction Limited and Bulk Diffusion Limited Case

One of the major difference between the two models is regarding the response time dependence on film thickness. For a surface reaction limited case, the response time is proportional to film thickness, $L$, while for a bulk vacancy diffusion limited case, the response time is proportional to $L^2$ (table 5.3). Figure 5.13 shows the response time of the planar film sensors to 200 ppb of $NH_3$ gas as a function of film thickness. The response time of the 50 nm $Au/WO_3$ film is also given to graphically determine the dependence of $\tau$ on film thickness $L$, even though there are discontinuities in the film leading to difference in baseline conductivity values with respect to 125 nm and 250 nm planar films. One important characteristic that stands out from the plot is that $\tau$ varies linearly with film thickness ($\tau \propto L$). This is only true for the surface reaction limited case.

Another factor that stands out is that $\tau$ does not approach 0 as film thickness becomes 0 nm as given in equations 3.24 and 3.25. This is because, the bulk conduction model was developed by assuming a step change in target gas partial pressure, and did not include the response time of the test cell. Ideally, the test cell response should also be considered while solving the differential equation (3.17), to get an accurate estimate of the sensor response time. Further details will be given in section 5.2.5.

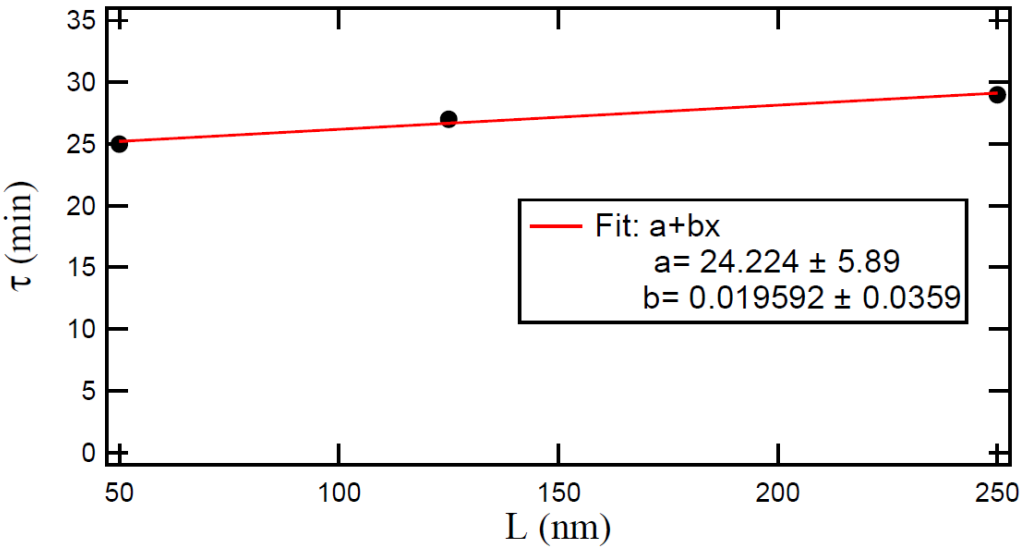


**Figure 5.13.** Linear dependence of response time, τ, of planar film sensors on film thickness, L, to 200 ppb of $NH_3$ gas.

Another distinction between the two models is the shape of the response curve. The ln-ln behavior of sensor response for surface reaction limited case is linear with a slope of 1, while in the diffusion limited case, the slope should be 0.5. Figure 5.14 illustrates the ln-ln behavior of the 100 nm GLAD film sensor response to 200 ppb of $NH_3$ gas as a function of time. The slope, was determined from a weighted non-linear least squares fit to be 0.98. This again indicates that sensor response is surface reaction limited.

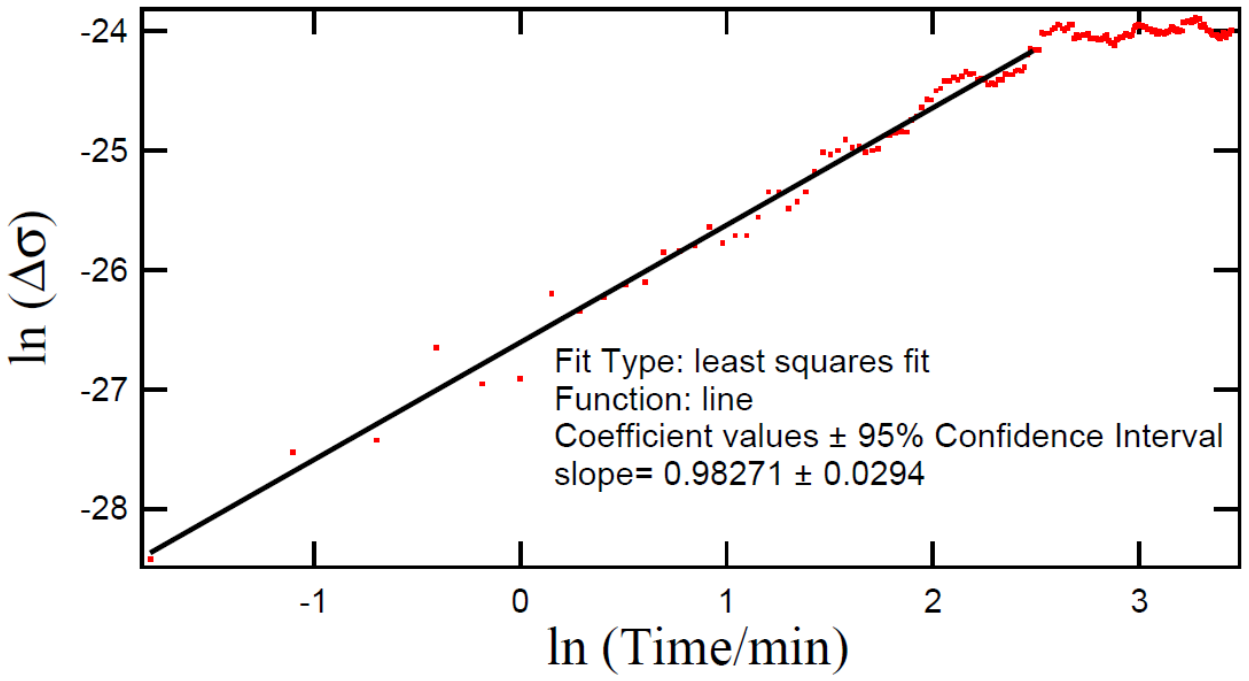


**Figure 5.14.** Ln-ln plot illustrating surface reaction limited behavior (slope 1) of 100 nm GLAD sensor response to 200 ppb of $NH_3$ gas at 450 °C.

Another method to determine whether the sensor response is surface reaction limited or diffusion limited is by using the response time equation for both surface reaction and bulk diffusion limited models. The slower process is the one that limits sensor response. Calculation of τ for the surface reaction limited case will be discussed first followed by the diffusion limited case. The baseline conductivity for the planar and GLAD films in air has already been calculated to be about $5 \times 10^{-3} \frac{1}{\Omega\, cm}$. Using this value, $[V_{ob}]_{air}$ was calculated and using equation 3.19 to get $\sim 1.26 \times 10^{16} \frac{1}{cm^3}$, $K$ was estimated to be approximately $7.0 \times 10^{-5}$. For a 125 nm film, the conductivity under exposure to 600 ppb $NH_3$ gas was calculated by adding the Δσ value obtained from figure 5.12 to the baseline conductivity value and from this $[V_{ob}]_t$ was calculated to be $\sim 1.6 \times 10^{16} \frac{1}{cm^3}$. Using equation 3.20, a value for $K_t$ was estimated to be $\sim 1.07 \times 10^{-5}$.

From figures 3.3 and 3.4, expressions for τ has already been calculated for the different pressure regimes and for this particular concentration, since $K_t < K$, equation 3.24 can be used to estimate τ. It will be shown later from the modeling that $\kappa_{ox}^{air} \cong .015\ \frac{1}{s}$ for the 125 nm planar film and using this value, τ value was calculated to be ~ 11.0 minutes for a surface reaction limited case. For the diffusion limited case, diffusion coefficient for $WO_3$ films of similar thickness were calculated (Appendix B) to be about $800\ \frac{nm^2}{s}$ at 450 °C. Using the same value of diffusion coefficient and using the relation $\tau = .85\frac{L^2}{D_0}$, τ was estimated to be about 20 seconds. These calculations not only indicate the validity of the models but also affirms that the sensor response is indeed surface reaction limited and not bulk diffusion limited.

### 5.2.5. Analysis of Sensor Response

We now demonstrate that the response of the $Au/WO_3$ sensors to $NH_3$ can be predicted semi-quantitatively from the surface reaction limit solution, equation 3.17, for a range of pressures, using independent experimental measurements of the mobility, V/A ratio, and rate constant for the reaction of $NH_3$ in air on $Au/WO_3$ catalysts. The model parameters are given in Table 5.4 and the time-dependent solution to equation 3.17 is compared to data for a planar film and a GLAD film in figure 5.15. Electron mobility (μ), surface oxygen vacancy coverage ($N_{ml}$), film thickness (L), Volume to area ratio (V/A) and reduction rate constant ($k_3$) are constants.

**Table 5.4.** Parameters in surface reaction limited model.

| Parameter | 100nm GLAD | Planar | Method |
|---|---|---|---|
| $\mu(\boldsymbol{cm^2V^{-1}s^{-1}})$ | 1.2 | 1.2 | Hall Effect |
| $\boldsymbol{N_{ml}(nm^2s^{-1})}$ | 7.716 | 7.716 | XRD |
| L/(nm) | 6.4 | 125 | SEM |
| $\boldsymbol{V/A\,(nm)}$ | 90 | 125 | SEM |
| $\boldsymbol{\kappa_{red}^{air}(s^{-1})}$ | $8.15 \times 10^{-7}$ | $1.07 \times 10^{-6}$ | $\frac{\kappa_{red}^{air}}{\kappa_{ox}^{air}} = 7x10^{-5}$ from $\sigma_{air} = 5\text{x}10^{-3}\Omega^{-1}cm^{-1}$ |
| $\boldsymbol{\kappa_{ox}^{air}(s^{-1})}$ | 0.012 | 0.015 | |
| $\boldsymbol{k_3\ (atm^{-1}s^{-1})}$ | 0.143 | 0.143 | k/N =1.05 from microreactor |

The mobility was determined previously[82] as a function of temperature using the Hall effect. The number of adsorption sites, $N_{ml}$ taken to be the number of terminal oxygens (or W ions) per unit area on the $WO_3$ (100) surface based on the monoclinic x-ray crystal structure.[152] The thickness of the films was determined by quartz crystal oscillator measurements during film deposition, calibrated against profilometry for the planar films. The baseline conductivity in air was relatively constant at 450 °C for film thicknesses greater than 20 nm. For the GLAD film, SEM measurements show that there is a continuous base layer of $WO_3$ that determines the baseline conductivity with rods extending 100 nm; the estimated layer thickness of 6.4 nm, calculated from the known conductivity at 450 °C. The conversion of $NH_3$ in air was measured in a packed bed microreactor as a function of temperature. The only reaction product identified by mass spectrometry was $N_2O$. The overall rate constant for the reaction, $k_{NH_3}$= 8.1 $atm^{-1}nm^{-1}$ $s^{-}$

[1], was calculated from 35% conversion at 450 °C. The ratio of $\frac{\kappa_{red}}{\kappa_{ox}}$, was constrained by the value of $K$ determined from $N_{ml}$, μ, and the baseline conductivity at 450 °C using equation 3.19.

Figures 5.15 a and 5.15 b shows that the simplified surface reaction model accounts for both the magnitude of the conductivity change and the response time for step increases and decreases in $NH_3$ concentration. The variation in the thickness of the continuous film, $L$, from 6.4 to 125 nm, is accounted for by the model, demonstrating that the bulk conductivity is independent of film thickness. The small value of $L$ in the GLAD film results in a higher resistance, and consequently poorer signal to noise ratio. The V/A ratio of the GLAD film is about 70% that of the 125 nm planar film, accounting for the slightly faster response. The red curves include the response time of the test cell, which has been measured to be approximately twice the volume/flow rate ratio for NO.[51] Because $NH_3$ is quite sticky, the test cell response times required to fit the sensor data were approximately 200 s and probably accounts for the slower measured response during decreases in $NH_3$ concentration. The ideal sensor response can be estimated from the dashed blue curves, which change faster than the sensor response.

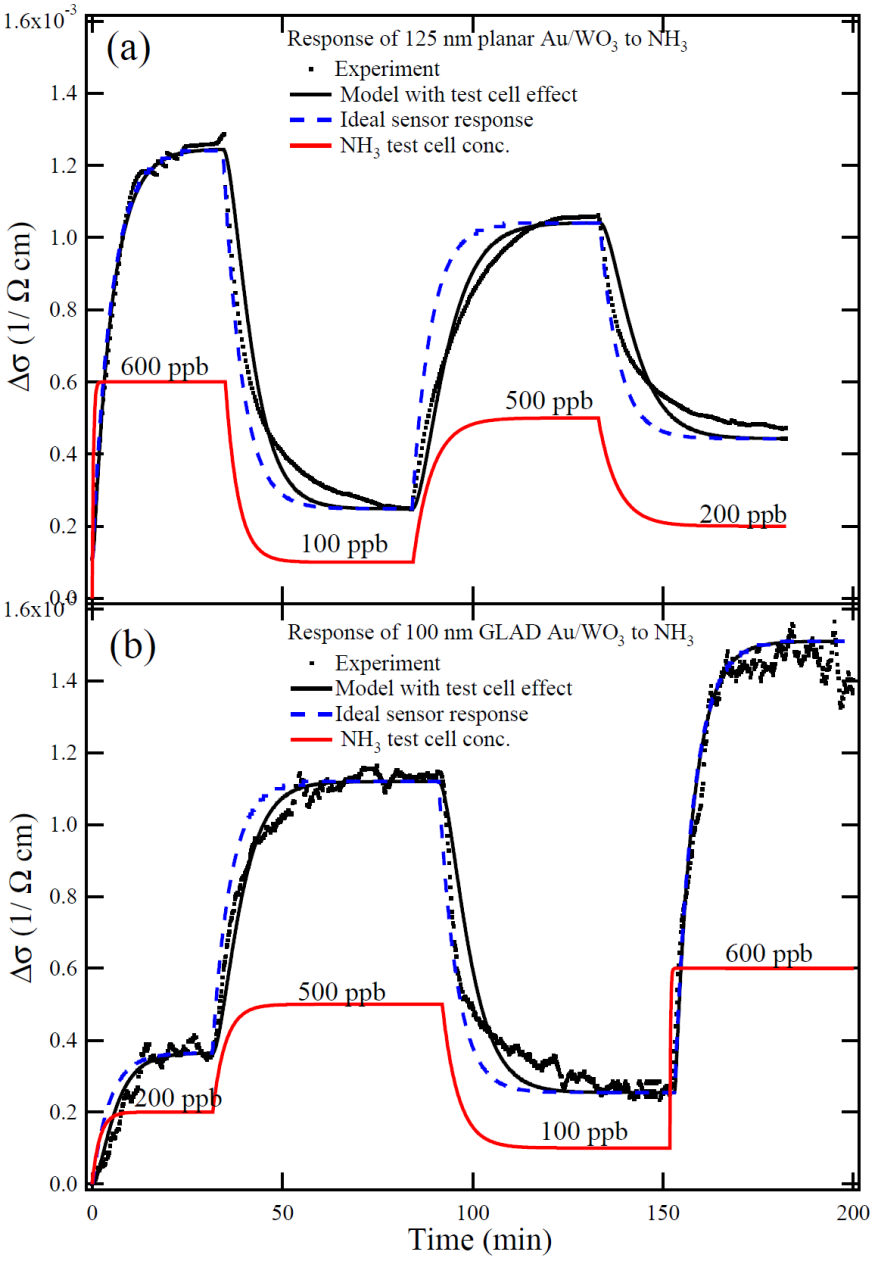


**Figure 5.15.** Comparison of experimentally measured and predicted Δσ as a function of time for (a) 125 nm planar $Au/WO_3$ film and (b) 100 nm GLAD $Au/WO_3$ film using the surface reaction-limited model to 100,200,500 and 600 ppb of $NH_3$ in air at 450 °C.

### 5.2.6. Sensor Optimization

For single component chemical detection purposes, the primary performance specifications are $\Delta\sigma$ and response time, which depend on temperature and target gas pressure. This section illustrates the use of the bulk conduction model to predict sensor performance, given temperature and pressure dependence of reaction rates and the diffusion coefficient, $D(T)$. Values of the kinetic parameters, described in section 3.5.2, chosen to give values of $K$ and $K_t$ at 450 °C and 600 ppb $NH_3$ are given in Table 5.5.

**Table 5.5.** Parameters chosen to give values of $\boldsymbol{K}$ and $\boldsymbol{K_t}$ at 450 °C and 600 ppb $NH_3$.

| | | |
|---|---|---|
| Vacancy creation | $A_2 = 3.8\text{x}10^2\ s^{-1}$ | $E_{vac}$=120 kJ/mol |
| Oxidation | $s = 2.6\text{x}10^{-10}$ | |
| $NH_3$ desorption | $A_{des} = 2\text{x}10^{11}\ s^{-1}$ | $E_{des}$ = 100 kJ/mol |
| $NH_3$ reaction | $A_3 = 390\ s^{-1}$ | $E_{rxn}$ = 115 kJ/mol |

The model predicts that the surface reaction rate increases with temperature, as shown in figure 5.16 a. Using Campbell's criterion for rate control, it is determined that the surface reaction is rate controlling, consistent with relatively high $NH_3$ coverages.[153] The predicted response, $\Delta\sigma$, increases continuously with temperature, shown in figure 5.16 c, qualitatively similar to experimental measurements. This behavior can be understood qualitatively from the bulk vacancy concentrations in air and 10 ppm $NH_3$, shown in figure 5.16 b, in that both the surface reaction and intrinsic vacancy creation reaction increase with temperature while the oxidation rate is relatively constant. From the predicted temperature dependence of the intrinsic vacancy creation and oxidation reaction, $K(T)$ was calculated, while the ratio of the surface

reaction to oxidation rates determined $K_t(T)$. The value of $\Delta\sigma$, for several $NH_3$ concentrations was calculated from equation 3.21 and plotted in figure 5.16 c. Note that the response increases proportional to $NH_3$ pressure, but does not depend on the V/A ratio. The response time depends on film thickness and temperature, as shown in figure 5.16 d. At lower temperatures for thicker films, the response time is diffusion controlled, given by $\tau = 0.85\frac{L^2}{D}$. Note the $L^2$ dependence in the low temperature regime. At higher temperatures, the response time increases with surface reaction rates, but because the rate of reduction by $NH_3$ is less than the intrinsic reduction rate (i.e. $K_t < K$), the response time is not strongly dependent on $NH_3$ concentration. However, the response time increases linearly with $L$. Therefore, the ability to fabricate nanowires, could dramatically decrease response times in the diffusion limited regime, and significantly reduce response time in the surface reaction limit. In summary, the general predictions of the model are that the magnitude of the response increases with temperature, but there is a minimum in response time that depends on the film thickness. For target gas reactions that decrease at higher temperatures, for example due to decreasing coverage of less strongly bound intermediates or due to endothermic reactions,[154] the response may go through a maximum.

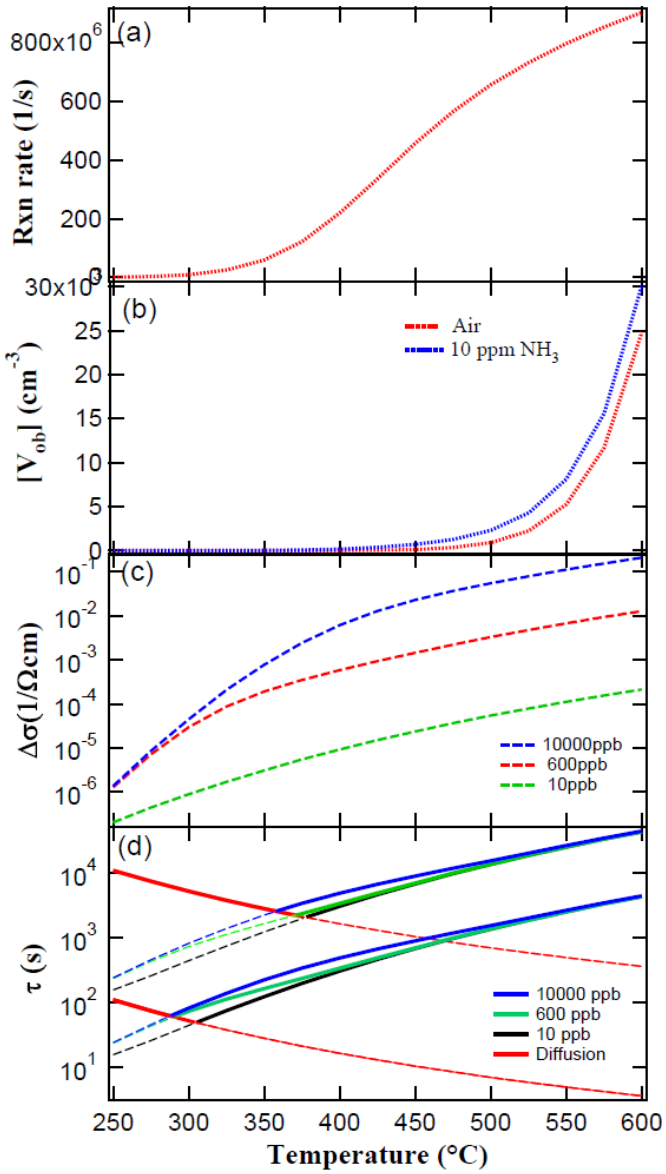


**Figure 5.16.** Bulk conduction model illustrating temperature dependence of surface reaction rates, bulk vacancy concentration, magnitude of response and response time. a) $NH_3$ surface reaction rate in air on $WO_3$, b) bulk vacancy concentration in air (red) and 10 ppm $NH_3$ (dashed blue), c) response for indicated $NH_3$ concentrations, and d) contributions to response time from diffusion (black) and surface reaction (colors for indicated $NH_3$ concentrations) for planar films of 1000 nm (solid curves) and 100 nm (dashed curves).

## 5.3. Chapter Summary

From the GC/MS and DRIFTS, reaction products as well as reaction rates due to $NH_3$ reaction on Au loaded $WO_3$ and as received $WO_3$ powders were determined. Kinetic models were applied to experimental data in order to determine the transduction mechanism associated with planar and GLAD Au/$WO_3$ film sensors to ppb concentration of $NH_3$ gas at 450 °C. From the response characteristics of planar and GLAD Au/$WO_3$ sensors to $NH_3$ gas, the transduction mechanism was determined to be due to bulk conduction mechanism. The response of all the sensors were surface reaction limited.

Sensor performance as a function of temperature was determined and suggestions were made for sensor optimization. Both reaction rate and $\Delta\sigma$ increased with temperature but response time decreased for a diffusion limited case and increased for a surface reaction limited case with temperature. Thus response time goes through a minimum and this is determined by the film thickness. At higher temperatures, the sensors are surface reaction limited but at lower temperatures, they are diffusion limited. Therefore fabricating thinner nanowires, nanorods or planar films will result in better sensor response.

# 6. SUMMARY, CONCLUSIONS AND FUTURE WORK

## 6.1 Summary

Two models commonly used to describe the transduction mechanism associated with SMO sensors are (1) the *Band Bending Model* and (2) the *Bulk Conduction Model*. The transduction mechanism in the band bending model has been studied extensively and is due to the target gas reacting with surface ionosorbed oxygen, which ultimately results in a change in film resistance**.** However, the bulk conduction model, in which the target gas reacts with surface lattice oxygen to change the surface oxygen vacancy concentration along with significant vacancy diffusion into the film resulting in a change in film resistance, has not been studied in detail. Assuming the wrong transduction mechanism would most likely result in an incorrect interpretation of the sensor response data. This highlights the need for a comprehensive kinetic model to describe the response characteristics of SMO film sensors, due to bulk conduction model, in order to elucidate the differences between the two sensor transduction mechanisms.

This thesis reports on a bulk conductivity sensor model for two limiting cases, where the sensor response is either limited by (i) surface reaction rates or (ii) bulk vacancy diffusion rates. The conduction models were developed for both planar and GLAD SMO film sensor morphologies. For the surface reaction model, kinetic equations for gas film interaction was developed to relate how chemical reaction kinetics can affect the change in film conductivity ($\Delta\sigma$) and mathematical expressions were derived to relate parameters like rate constants, target gas partial pressure and surface area to volume ratio to $\Delta\sigma$ and response time ($\tau$). The temperature and pressure dependence of reaction rates and $\Delta\sigma$ was also studied for sensor optimization purposes. The bulk diffusion model was developed to determine how diffusion

kinetics can affect sensor response time and mathematical expressions were derived to relate parameters like diffusion coefficient and film thickness to $\tau$. Bulk diffusion rate does not affect $\Delta\sigma$ as its magnitude is determined only by surface reaction kinetics. From the models, key characteristics are identified which could help to differentiate a sensor response due to band bending mechanism from that due to bulk conduction mechanism. The models can also be used to differentiate a surface reaction limited response from a bulk diffusion limited one. Once the limiting step is identified, the performance can be optimized for a particular target gas through appropriate parameter choices.

The practical usability of the models is highlighted by comparing the results of the models to experimental data obtained from 100 nm GLAD Au/$WO_3$ film, 125 nm planar Au/$WO_3$ film and 250 nm planar Au/$WO_3$ film chemiresistive sensors exposed to ppb levels of $NH_3$ gas at 450 °C. In order to compare the model with the experimental data, GC/MS and DRIFTS studies were done on pure $WO_3$ powder catalyst (20 $\mu m$) and 0.1% Au loaded $WO_3$ catalyst (20 $\mu m$) under a flow of $NH_3$ gas while the catalyst was subjected to a temperature ramp to determine the reaction products, order of the reaction and the $NH_3$ reaction rates at different temperatures, as a result of gas/catalyst interaction. Based on the results obtained from the GC/MS study, $NH_3$ reaction rates were determined for different temperatures, which was used for surface reaction modeling of Au doped planar and GLAD $WO_3$ film gas sensor response to ppb concentrations of $NH_3$ gas at 450 °C. The dependence of $\Delta\sigma$ on target gas partial pressure was a key characteristic obtained from the model and this was used to determine whether the experimental sensor response was due to band bending mechanism or due to bulk conduction mechanism. Once it was determined that the sensor response was due to bulk conduction mechanism, it needed to be determined whether the response was surface reaction limited or bulk

vacancy diffusion limited. The dependence of $\tau$ on film thickness, shape of $\Delta\sigma$ as a function of time and equations for $\tau$ were used to determine whether the sensor response limiting case. Based on the limiting case, suggestions were made, to changes in film morphology, to develop sensors with improved response characteristics.

## 6.2 Conclusions

### 6.2.1 Conclusions – Surface Reaction Model

For the surface reaction model, bulk diffusion was assumed to be fast such that the vacancies are uniformly spatially distributed in the film such that there is no concentration gradient in the film. For this case, by solving the differential equation, the shape of the sensor response curve as a function of time (t) was determined to be of the form, $y\ (1 - e^{-xt})$, where $y$ and $x$ are constants. Moreover, at steady state, $\Delta\sigma$ is independent of film surface area to volume ratio ( $\frac{A}{V}$ ) ratio and depends only on surface reaction kinetics. However, $\tau$ varies proportionally to $\frac{V}{A}$ ratio. Thus, for planar films, fast responding sensors can be developed by fabricating thinner films. For the GLAD films, if the response is surface reaction limited, fast responding sensors can be developed by fabricating thinner nanorods that are well spaced to offer a smaller $\frac{V}{A}$ ratio.

In order to relate $\Delta\sigma$ and $\tau$ to both rate constants and target gas concentration, two dimensionless factors are considered in the model, namely, target gas concentration factor and oxide reducibility factor. Since rate constants have an Arrhenius relation with temperature, the sensors are assumed to be at constant temperature. Partial pressure of oxygen was also assumed to be constant. In the low pressure regime, both $\Delta\sigma$ and $\tau$ depends on oxide reducibility, $K$. Therefore, for sensors operating in the low pressure regime there is a tradeoff between

magnitude and speed of response when choosing the oxide for the sensor. For quick detection of toxic gases, in this regime, a less reducible oxide need to be used. On the other hand if the objective is to detect low concentration gases for environmental monitoring, where $\tau$ may not be a factor, more reducible oxides can be used for improved $\Delta\sigma$. In the intermediate pressure regime, both $\Delta\sigma$ and $\tau$ depends on target gas partial pressure and reducibility of the oxide is not a factor in this pressure regime. Thus, for sensors operating in the intermediate pressure regime there is a tradeoff between magnitude and speed of response while changing target gas concentration. If oxide reducibility factor $\geq 1$, then the oxide is completely reduced to a metal, and sensor response becomes independent of target gas pressure.

Temperature and pressure dependence of reaction rates and $\Delta\sigma$ were determined for sensor optimization processes. $\Delta\sigma$ increases with $NH_3$ pressure but does not depend on $\frac{V}{A}$ ratio. Both reaction rate and $\Delta\sigma$ increased with temperature, but response time decreased for a diffusion limited case and increased for a surface reaction limited case with temperature. Thus response time goes through a minimum and this is determined by the film thickness. At higher temperatures, the sensors are surface reaction limited but at lower temperatures, they are diffusion limited. Therefore fabricating thinner nanowires, nanorods or planar films will result in better sensor response.

### 6.2.2 Conclusions – Bulk Diffusion Model

For the diffusion limited case, the surface reaction rate is assumed to be sufficiently fast to maintain a constant coverage of vacancies at the film surface (planar films) or exposed nanorod surface (GLAD films), which can then diffuse into the bulk of the oxide film. Response time, $\tau$, of the sensor depends on the time taken for the vacancies to diffuse into and equilibrate

within the bulk of the film. In planar polycrystalline films, vacancy diffusion, can take place along the grain boundaries as well as through the lattice. Two models are considered for calculating vacancy diffusion effects namely (i) Crank's 1-D diffusion model [124] for lattice diffusion and (ii) the Gilmer Farrell model [41] for grain boundary diffusion in polycrystalline planar films. Both these models help in identifying the conditions in which grain boundary diffusion effects dominate the planar sensor response as well as identifying the conditions in which grain boundary effects are minimal compared to lattice diffusion. In cylindrical nanorods, diffusion can take place along the length of the cylinder as well as radially. The target gas can react on the sides of the nanorods to form surface vacancies which then causes a radial vacancy concentration gradient that drives radial diffusion. The mathematical expression for radial diffusion into a cylindrical rod, developed by Crank, was used with an effective diffusion coefficient. The solution for vacancy diffusion along the length of the cylinder (no reactions on the cylindrical sides) is similar to the planar film case.

The shape of the sensor response curve as a function of time for the planar sensor response obtained from both Crank's 1-D and Gilmer Farrell models as well as the nanorod film sensor response obtained from the radial diffusion model, have an initial $t^{\frac{1}{2}}$ response characteristic that approaches saturation. This is an important characteristic which can differentiate a surface reaction limited response ($y\ (1 - e^{-xt})$) from a bulk diffusion limited sensor response. The mathematical expression for response time, $\tau$, was determined for both film structures. For planar films, $\tau \propto \frac{L^2}{D_0}$, where $L$ is the film thickness and $D_0$is the lattice diffusion coefficient and for nanorod films, $\tau \propto \frac{R^2}{D_{eff}}$, where $R$ is the nanorod radius and $D_{eff}$ is the effective diffusion coefficient. This is another significant characteristic of the response that can

distinguish this limiting case from the surface reaction-limited case, where $\tau \propto L$. Also, for the same kinetic and geometric parameters, radial diffusion in nanorod films is much faster than diffusion in planar films, suggesting that nanorod film geometry may be ideal for sensors whose response is diffusion limited. Diffusion coefficients of some common oxides as a function of temperature is illustrated to show the effects of material choices and operating temperature in a diffusion-limited sensor response. From the expressions for $\tau$, it is apparent that developing sensors with thinner films or thinner nanorods results in faster response.

### 6.2.3 Conclusions- GC/MS and DRIFTS

From the GC/MS study, no visible reaction product was observed under 350 °C, but at higher temperatures, $N_2O$ and $H_2O$ desorption took place for $NH_3$ reaction on both Au loaded and pure $WO_3$ catalysts. From $NH_3$ conversion data, $N_2$ formation was also likely but identifying $N_2$ gas was difficult since air was also fed into the catalyst bed. From the study, $NH_3$ conversion rate was determined to be higher for the Au loaded catalyst than for the pure one, indicating that Au additive plays a role in increasing the $NH_3$ reaction rate on the catalyst surface. DRIFTS study indicated that $NH_3$ adsorbs on the Lewis and Brønsted acid sites. The study also showed that reaction rate was faster in Au loaded catalyst than for the pure one, thus corroborating the findings from the GC/MS study. From the DRIFTS data, it was determined that $NH_3$ reaction on $WO_3$ catalyst surface was a $1^{st}$ order reaction.

### 6.2.4 Conclusions –Transduction Mechanism and the Response Limiting Case

The transduction mechanism for 100 nm Au/$WO_3$ GLAD film, 125 nm Au/$WO_3$ planar film and 250 nm Au/$WO_3$ planar film sensors to ppb levels of $NH_3$ gas at 450 °C were determined by observing the power law dependence of the sensor response versus $NH_3$ gas

partial pressure. The linear dependence of $\Delta\sigma$ on gas concentration for all three films indicates that the transduction mechanism is dominated by bulk conduction rather than band bending. Moreover, the response of all three films were independent of $\frac{V}{A}$ ratio, indicating that the transduction mechanism is due to bulk conduction. Once the transduction mechanism was identified, the response limiting case was also determined. The dependence of $\tau$ on film thickness can differentiate surface reaction limited response from a bulk diffusion limited response. Response time to 200 ppb of $NH_3$ gas exposure plotted as a function of film thickness was linear, indicating a surface reaction limited response. Another difference between the two limiting cases is the shape of the response curve. The ln-ln behavior of the 100 nm GLAD film sensor response to 200 ppb of $NH_3$ gas as a function of time, was linear with slope = 1, indicating again that the sensor response is surface reaction limited. The response time equations developed for both models was also used to determine the response limiting case. For a 125 nm planar Au/$WO_3$ film, response time was determined to be much slower for the surface reaction-limited case than for the bulk diffusion-limited case. Thus, comparison of the models with the experimental Au/$WO_3$ film sensor response, under the test conditions discussed above, shows evidence of a surface reaction-limited case for this SMO sensor.

### 6.2.5 Conclusions –Application of Surface Reaction Model to GLAD and Planar Film Sensors

Application of surface reaction-limited model to the 100 nm GLAD Au/$WO_3$ film and 125 nm planar Au/$WO_3$ film sensors indicate time-dependent changes in the $NH_3$ partial pressure. Variations in $\Delta\sigma$ and $\tau$ between the models and the experimental data can be attributed to uncertainties associated with temperature calibration data and test cell response time. The

predicted $\frac{A}{V}$ ratio is lower for the planar films and they have a slower response time compared to GLAD film sensors. Both sensors are operating in the low pressure regime, and therefore both $\Delta\sigma$ and $\tau$ depend on oxide reducibility. For environmental detection of ppb levels of $NH_3$ gas, $WO_3$ film based sensor operating at 450 °C are suitable. However for medical applications which may require quick detection, less reducible oxides can be more suited but this requires further experimental study. For higher concentrations of $NH_3$ gas, the sensors will be operating in the intermediate pressure regime and both $\Delta\sigma$ and $\tau$ would be independent of oxide reducibility. In this pressure regime, where safety is of concern, sensor operating temperature becomes a major factor.

## 6.3 Future Work

### 6.3.1 Determining Peak Sensitivity as a Function of Operating Temperature.

For the bulk conduction mechanism, as sensor operating temperature changes, reaction rate also changes and this affects overall reaction kinetics. Based on the bulk conduction model, developed in this thesis, $\Delta\sigma$ and reaction rates increases in a temperature range of 200 °C -500 °C. A maximum in sensitivity as a function of temperature could not be identified for $NH_3$ reaction on $WO_3$. But for certain gas-film reactions (having different activation energies and pre-exponential factors), sensitivity may go through a maximum at a particular temperature. Identifying this operating temperature can be useful for different gas sensing applications.

### 6.3.2 Vacancy Diffusion Effects in Other Complex Nanostructures.

In this study, vacancy diffusion effects have been extensively studied in cylindrical nanostructures but the diffusion equations developed in this study may not be applicable to other types of nanostructures like nanospheres and nanocubes which are also gaining prominence for

gas sensing applications. Thus developing vacancy diffusion models to take into account the different nanostructure geometries can give a wider reach for these models.

### 6.3.3 Thermodynamic Effects in Surface Reaction Model.

The energy of vacancy formation at the surface ($\Delta G_f^{\circ}$) (terminal oxygen species), which characterizes the equilibrium vacancy concentration at a particular temperature, is lower than that for the bulk oxygen species. The model developed in this study does not take into account the difference in thermodynamics of vacancy formation at the surface to that in the bulk. In future, for metal oxide films, a mathematical model that includes surface reaction rates that takes into account the creation of oxygen vacancies can help in improving the accuracy of the model.

## BIBLIOGRAPHY


1. Liu, X.; Cheng, S.; Liu, H.; Hu, S.; Zhang, D.; Ning, H., A Survey on Gas Sensing Technology. *Sensors* **2012,** *12* (7), 9635-9665.

2. Kohl, D., Function and Application of Gas Sensor. *Jounal of Physics D: Applied Physics* **2001,** *34*, R125-R149.

3. Korotcenkov, G.; Brinzari, V.; Cho, B. K., Conductometric gas sensors based on metal oxides modified with gold nanoparticles: a review. *Microchimica Acta* **2016**, 1033-1054.

4. Timmer, B.; Olthuis, W.; Berg, A. V. D., Ammonia sensors and their applications—a review. *Sensors and Actuators B: Chemical* **2005,** *107* (2), 666-677.

5. Sensitron. Catalytic Sensors. (accessed 07/07/**2010**). <http://www.sensitron.it/wp-content/uploads/2010/07/CatalyticSensors.pdf>

6. Lahdesmaki, I.; Kubiak, W. W.; Lewenstam, A.; Ivaska, A., Interference in a polypyrrole-based amperometric ammonia sensor. *Talanta* **2000,** *52*, 269-275.

7. Kanan, S. M.; El-Kadri, O. M.; Abu-Yousef, I. a.; Kanan, M. C., Semiconducting metal oxide based sensors for selective gas pollutant detection. *Sensors (Basel, Switzerland)* **2009,** *9* (10), 8158-96.

8. Seiyama, T.; Fujiishi, K.; Nagatani, M.; Kato, A., A New Detector for Gaseous Components Using Zinc Oxide Thin Films. *The Journal of the Society of Chemical Industry, Japan* **1963,** *66* (5), 652-655.

9. Vetelino, J. F.; Reghu, A., *Introduction to Sensors*. CRC Press: 2009.

10. Bardeen, J., Surface states and rectification at a metal semi-conductor contact. *Physical Review* **1947,** *71* (10), 717-727.

11. Seiyama, T.; Seiyama, T.; Kagawa, S.; Kagawa, S.; Co-investigator, N., Study on a detector for gaseous components using semiconductive thin films. *Analytical Chemistry* **1966,** *38* (8), 1069-1073.

12. Lalauze, R.; Pijolat, C., A new approach to selective detection of gas by an SnO2 solid-state sensor. *Sensors and Actuators* **1984,** *5* (1), 55-63.

13. Watson, J., The tin oxide gas sensor and its applications. *Sensors and Actuators* **1984,** *5* (1), 29-42.

14. Xu, Z.; Vetelino, J. F.; Lec, R.; Parker, D. C., Electrical properties of tungsten trioxide films. *Journal of Vacuum Science & Technology A: Vacuum, Surfaces, and Films* **1990,** *8* (4), 3634-3638.

15. Ishihara, T.; Arai, H.; Eguchi, K., The Mixed oxide $Al_2O_3$-$V_2O_5$ as a Semiconductor Gas Sensor for NO and $NO_2$. *Sensors and Actuators* **1989,** *19*, 259-265.

16. Taguchi, N. U.S. Patent 36235756. 1970.

17. Baresel, D.; Gellert, W.; Sarholz, W.; Scharner, P., Influence of Catalytic Activity on Semiconducting Metal Oxide Sensors. *Sensors and Actuators* **1984,** *6*, 35-50.

18. Srivastava, V.; Jain, K., Highly sensitive $NH_3$ sensor using Pt catalyzed silica coating over $WO_3$ thick films. *Sensors and Actuators B: Chemical* **2008,** *133* (1), 46-52.

19. Luh, N.; Septiani, W.; Yuliarto, B., Review-The Development of Gas Sensor Based on Carbon. *Journal of Electrochemical Society* **2016,** *163* (3), 97-106.

20. Frattodi, I.; Venditti, I.; Cametti, C.; Russo, M. V., Chemiresisitive polyanaline-based gas sensors: A mini Review. *Sensors and Actuators B: Chemical* **2015,** *220*, 534-548.

21. Kim, F. S.; Ren, G.; Jenekhe, S. A., One-dimensional nanostructures of π-conjugated molecular systems: Assembly, properties, and applications from photovoltaics, sensors, and nanophotonics to nanoelectronics. *Chemistry of Materials* **2011,** *23* (3), 682-732.

22. Briglin, S. M.; Lewis, N. S., Characterization of the Temporal Response Profile of Carbon Black-Polymer Composite Detectors to Volatile Organic Vapors. *Journal of Physical Chemistry B* **2003,** *107*, 11031-11042.

23. Collins, P. G.; Bradley, K.; Ishigami, M.; Zettl, A., Extreme Oxygen Sensitivity of Electronic Properties of Carbon Nanotubes Published by : American Association for the Advancement of Science. *Science* **2016,** *287* (5459), 1801-1804.

24. Liu, H.; Czaplewski, A.; Craighead, H. G., Polymeric Nanowire Chemical Sensor. *Nano Letters* **2004,** *4* (671-675).

25. Sayago, I.; Santos, H.; Horrillo, M. C.; Aleixandre, M.; Fernandez, M. J.; Terrado, E.; Tacchini, I.; Aroz, R.; Maser, W. K.; Benito, a. M.; Martinez, M. T.; Gutierrez, J.; Munoz, E., Carbon nanotube networks as gas sensors for $NO_2$ detection. *Talanta* **2008,** *77* (2), 758-764.

26. LeGore, L. J.; Lad, R. J.; Moulzolf, S. C.; Vetelino, J. F.; Frederick, B. G.; Kenik, E. a., Defects and morphology of tungsten trioxide thin films. *Thin Solid Films* **2002,** *406* (1-2), 79-86.

27. Che, M.; Tench, A. J., *Characterization of Reactivity of Molecular Oxygen Species on Oxide Surfaces*. Academic Press: 1982; Vol. 31.

28. Che, M.; Tench, A. J., *Characterization and Reactivity of Mononuclear Oxygen Species on Oxide Surfaces*. Academic Press: 1983; Vol. 32.

29. Schvets, V. A.; Kazansky, V. B., Oxygen anion-radicals adsorbed on supported oxide catalysts containing Ti, V and Mo ions. *Journal of Catalysis* **1972,** *25* (1), 123-130.

30. Schvets, V. A.; Sapozhnikov, V. B.; Chuvylkin, N. D.; Kazansky, V. B., EPR study of $O^-$ anion radicals and their reaction with ethylene on$WO_3/SiO_2$ catalyst. *Journal of Catalysis* **1978,** *52* (3), 459-461.

31. Barsan, N.; Weimar, U., Conduction model of metal oxide gas sensors. *Journal of Electroceramics* **2001,** *7*, 143-167.

32. Iwamoto, M.; Yoda, Y.; Yamazoe, N.; Seiyama, T., Study of metal oxide catalysts by temperature programmed desorption. 4. Oxygen adsorption on various metal oxides. *The Journal of Physical Chemistry* **1978,** *82* (24), 2564-2570.

33. Jimenez, I.; Vila, A. M.; Calveras, A. C.; Morante, J. R., Gas-sensing properties of catalytically modified $WO_3$ with copper and vanadium for $NH_3$ detection. *IEEE Sensors* **2005,** *5* (3), 385-391.

34. Galstyan, V.; Comini, E.; Baratto, C.; Faglia, G.;Sberveglieri, G., Nanostructured ZnO chemical gas sensors. *Cermaics International* **2015,** *41*, 14239-14244.

35. Tamaki, J.; Zhang, Z.; Fujimori, K.; Akiyama, M.; Harada, T.; Miura, N.; Yamazoe, N., Grain-Size Effects in Tungsten Oxide-Based Sensor for Nitrogen Oxides. *Journal of Electrochemical Society* **1994,** *141* (8), 2207-2210.

36. Shen, Y.; Yamazaki, T.; Liu, Z.; Meng, D.; Kikuta, T.; Nakatani, N., Influence of effective surface area on gas sensing properties of $WO_3$ sputtered thin films. *Thin Solid Films* **2009,** *517* (6), 2069-2072.

37. Li, G.; Zhang, X.; Kawi, S., Relationships between sensitivity , catalytic activity , and surface areas of $SnO_2$ gas sensors. *Sensors and Actuators B: Chemical* **1999,** *60*, 64-70.

38. Yamazoe, N.; Shimanoe, K., Theory of power laws for semiconductor gas sensors. **2008,** *128* (2), 566-573.

39. Weisz, P. B., Effects of Electronic Charge Transfer between Adsorbate and Solid on Chemisorption and Catalysis. *The Journal of Chemical Physics* **1953,** *21* (9), 1531-1531.

40. Kim, H.; Han, C., Barrier Height from V-I Characteritics of Semiconductor Contact: Reaction of Adsorbed Oxygen with Carbon Monoxide on ZnO. *Bulletin of Korean Chemical Society* **1997,** *18* (2), 149-151.

41. Ahlers, S.; Müller, G.; Doll, T., A rate equation approach to the gas sensitivity of thin film metal oxide materials. *Sensors and Actuators B: Chemical* **2005,** *107* (2), 587-599.

42. Vuong, N. M.; Kim, D.; Kim, H., Surface gas sensing kinetics of a $WO_3$ nanowire sensor: Part 1 - oxidizing gases. *Sensors and Actuators B: Chemical* **2015,** *220*, 932-941.

43. Vuong, N. M.; Kim, D.; Kim, H., Surface gas sensing kinetics of a $WO_3$ nanowire sensor: Part 2 - Reducing gases. *Sensors and Actuators B: Chemical* **2016,** *224*, 425-433.

44. Fisher, J. C., Calculation of Diffusion Penetration Curves for Surface and Grain Boundary Diffusion. *Journal of Applied Physics* **1951,** *2* (1), 74-77.

45. Whipple, R. T. P., Concentration contours in hrain boundary diffusion. *Philosophical Magazine* **1954,** *45*, 1225-1237.

46. Suzuoka, T., Lattice and Grain Boundary in Polycrystals. *Trans Jpn Inst Metals* **1961,** *2*, 25-33.

47. Roe, G. M.; Stark, R. H., Numerical Solutions of the Diffusion Equation in Cylindrical Geometries. *96* **1954,** *3* (820-821).

48. Levine, H. S.; MacCallum, C. J., Grain Boundary and Lattice Diffusion in Polycrystalline Bodies *Journal of Applied Physics* **1960,** *31*, 595.

49. Gilmer, G. H.; Farrell, H. H., Grain-boundary diffusion in thin films: I. the isolated grain boundary. *Journal of Applied Physics* **1976,** *47* (9), 3792-3798.

50. LeGore, L. J. Microstructure, Kinetics and Diffusion in Tungsten Trioxide Thin Film Sensors. PhD, University of Maine, 2000.

51. Pilling, R. S.; Bernhardt, G.; Kim, C. S.; Duncan, J.; Crothers, C. B. H.; Kleinschmidt, D.; Frankel, D. J.; Lad, R. J.; Frederick, B. G., Quantifying gas sensor and delivery system response time using GC/MS. *Sensors and Actuators B: Chemical* **2003,** *96* (1-2), 200-214.

52. Deniz, D.; Frankel, D. J.; Lad, R. J., Nanostructured tungsten and tungsten trioxide films prepared by glancing angle deposition. *Thin Solid Films* **2010,** *518* (15), 4095-4099.

53. Guérin, J.; Aguir, K.; Bendahan, M., Modeling of the conduction in a WO3 thin film as ozone sensor. *Sensors and Actuators B: Chemical* **2006,** *119* (1), 327-334.

54. Chen, D.; Hou, X.; Wen, H.; Wang, Y.; Wang, H.; Li, X.; Zhang, R.; Lu, H.; Xu, H.; Guan, S.; Sun, J.; Gao, L., The enhanced alcohol-sensing response of ultrathin $WO_3$ nanoplates. *Nanotechnology* **2010,** *21* (3), 035501-035501.

55. Li, F.; Qin, Q.; Zhang, N.; Chen, C.; Sun, L.; Liu, X.; Chen, Y.; Li, C.; Ruan, S., Improved gas sensing performance with Pd-doped $WO_3 \cdot H_2O$ nanomaterials for the detection of xylene. *Sensors and Actuators B: Chemical* **2017,** *244*, 837-848.

56. Schönauer, D.; Sichert, I.; Moos, R., Vanadia doped tungsten–titania SCR catalysts as functional materials for exhaust gas sensor applications`. *Sensors and Actuators B: Chemical* **2011,** *155* (1), 199-205.

57. Freer, R., Self-diffusion and impurity diffusion in oxides. *Journal of Materials Science* **1980,** *15*, 803-824.

58. Williams, D. E., Semiconducting oxides as gas-sensitive resistors. *Sensors and Actuators B: Chemical* **1999,** *57*, 1-16.

59. Schilling, O.; Colbow, K., A mechanism for sensing reducing gases with vanadium pentoxide films. *Sensors and Actuators B: Chemical* **1994,** *21*, 151-157.

60. Thibodeau, T. J.; Canney, A. S.; DeSisto, W. J.; Wheeler, M. C.; Amar, F. G.; Frederick, B. G., Composition of tungsten oxide bronzes active for hydrodeoxygenation. *Applied Catalysis A: General* **2010,** *388* (1-2), 86-95.

61. Yang, J.; Lim, H.; Han, S., Influence of binders on the sensing and electrical characteristics of $WO_3$-based gas sensors. *Sensors and Actuators B: Chemical* **1999,** *60*, 71-77.

62. Ament, W.; Hiuzenga, J. R.; Kort, E.; Mark, T. W. v. d.; R.G., G.; Verkerke, G. J., Respiratory ammonia output and blood ammonia concentration during incremental excercise. *International Journal of Sports Medicine* **1999,** *20*, 71-77.

63. De la Hoz, R. E.; Scheuter, D. P.; Rom, W. N., Chronic lung disease secondary to ammonia inhalation injury: a report on three cases. *American Journal of Industrial Medicine* **1996,** *29* (2), 624-629.

64. Mayewski, P.; Legrand, M., Glaciochemistry of Polar Ice Cores: A Review *Reviews of Geophysics* **1997,** *35* (3), 219-243.

65. Wang, S. C.; Shaikh, M. O., A Room Temperature $H_2$ Sensor Fabricated Using High Performance Pt-Loaded $SnO_2$ Nanoparticles. *Sensors* **2015,** *15* (6), 14286-14297.

66. Bettuzzi, S., Introduction. *Advances in Cancer Research* **2009,** *104* (1), 1-8.

67. Moberg, D. R.; Thibodeau, T. J.; Amar, F. G.; Frederick, B. G., Mechanism of hydrodeoxygenation of acrolein on a cluster model of $MoO_3$. *Journal of Physical Chemistry C* **2010,** *114* (32), 13782-13795.

68. Barsan, N.; Koziej, D.; Weimar, U., Metal oxide-based gas sensor research: How to? *Sensors and Actuators B: Chemical* **2007,** *121* (1), 18-35.

69. Henrich, V. E.; P.A., C., *The Surface Science of Metal Oxides*. Cambridge University Press: 1994.

70. Cora, F.; Stachiotti, M. G.; Catlow, C. R. A.; Rodriguez, C. O., Transition metal oxide chemistry: Electronic structure study of $WO_3$, $ReO_3$, and $NaWO_3$. *Journal of Physical Chemistry B* **1997,** *101* (20), 3945-3952.

71. Boccuzzi, F.; Chiorino, A.; Ghiotti, G.; Guglielminotti, E., Metal/n-zinc oxide interaction: effect of the surrounding atmosphere on IR transparency. *Langmuir* **1989,** *5* (1), 66-70.

72. Boccuzzi, F.; Ghiotti, G.; Chiorino, A., Optical Properties of Microcrystalline Zinc Oxide. *Journal of the Chemical Society, Faraday Transactions* **1983,** *79*, 1779-1789.

73. Wang, F.; Di Valentin, C.; Pacchioni, G., Semiconductor-to-metal transition in $WO_{3-x}$: Nature of the oxygen vacancy. *Physical Review B* **2011,** *84* (7), 1-5.

74. Wang, F.; Di Valentin, C.; Pacchioni, G., Electronic and Structural Properties of $WO_3$: A Systematic Hybrid DFT Study. *Journal of Physical Chemistry C* **2011,** *115* (6), 8345-8353.

75. Tsukada, M.; Adachi, H.; Satoko, C., Theory of electronic structure of oxide surfaces. *Progress in Surface Science* **1983,** *14*, 113-174.

76. Wang, W.; Janotti, A.; Van de Walle, C. G., Role of oxygen vacancies in crystalline $WO_3$. *Journal of Materials Chemistry C* **2016,** *4*, 6641-6648.

77. Levine, J. D.; Mark, P., Theory and Observation of Intrinsic Surface States on Ionic Crystals. *Physical Review* **1966,** *144* (2), 751-763.

78. Bube, R. H., Pulse Excitation Studies of Gain and Trapping in Photoconductors. *Journal of Applied Physics* **1963,** *34* (11), 3309-3314.

79. Madou, M. J.; Morrison, S. R., *Chemical Sensing with Solid State Devices*. Academic Press Inc: 1989.

80. Göpel, W.; Lampe, U., Influence of defects on the electronic structure of zinc oxide surfaces. *Physical Review B* **1980,** *22* (12), 6447-6462.

81. Berak, J. M.; Sienko, M. J., Effect of Oxygen-Deficiency on Electrical Transport Properties of Tungsten Trioxide Crystals. *Journal of Solid State Chemistry* **1970,** *133*, 109-133.

82. Moulzolf, S. C.; Frankel, D. J.; Lad, R. J., In situ four-point conductivity and Hall effect apparatus for vacuum and controlled atmosphere measurements of thin film materials. *Review of Scientific Instruments* **2002,** *73* (6), 2325-2325.

83. Gillet, M.; Aguir, K.; Lemire, C.; Gillet, E.; Schierbaum, K., The structure and electrical conductivity of vacuum-annealed $WO_3$ thin films. *Thin Solid Films* **2004,** *467* (1-2), 239-246.

84. Gulati, S.; Mehan, N.; Goyal, D. P.; Mansingh, A., Electrical equivalent model for $SnO_2$ bulk sensors. *Sensors and Actuators B: Chemical* **2002,** *87*, 309-320.

85. Dutta, P. K.; Ginwalla, A.; Hogg, B.; Patton, B. R.; Chwieroth, B., Interaction of Carbon Monoxide with Anatase Surfaces at High Temperatures : Optimization of a Carbon Monoxide Sensor. *Journal of Physical Chemistry B* **1999,** *103*, 4412-4422.

86. Comini, E.; Faglia, G.; Sberveglieri, G., *Solid State Gas Sensing*. Springer: 2009.

87. Mars, P.; van Krevelen, D. W., Oxidation carried out by means of vanadium oxide catalysts. *Chemical Engineering Science* **1954,** *3* (1), 41-59.

88. Liu, H. F., *Environmental Engineers Handbook*. CRC Press: 1997.

89. Grasselli, R. K., Fundamental principles of selective heterogeneous oxidation catalysis. *Topics in Catalysis* **2002,** *21* (1-3), 79-88.

90. Pérez-Ramírez, J.; Kondratenko, E. V., Mechanism of ammonia oxidation over oxides studied by temporal analysis of products. *Journal of Catalysis* **2007,** *250* (2), 240-246.

91. Pestman, R.; Koster, R. M.; Pieterse, J. A. Z.; Ponec, V.; van Duijne, A., Reactions of Carboxylic Acids on Oxides. *Journal of Catalysis* **1997,** *168* (2), 255-264.

92. Scanlon, D. O.; Morgan, B. J.; Watson, G. W.; Walsh, A., Acceptor Levels in p-Type $Cu_2O$ : Rationalizing Theory and Experiment. *Physical Review Letters* **2009,** *096405*, 1-4.

93. Shao, F.; Hernández-ramírez, F.; Prades, J. D.; Fàbrega, C.; Andreu, T.; Morante, J. R., Applied Surface Science Copper ( II ) oxide nanowires for p-type conductometric $NH_3$ sensing. *Applied Surface Science* **2014,** *311*, 177-181.

94. Kofstad, P., Defects and transport properties of metal oxides. *Oxidation of Metals* **1995,** *44* (1-2), 3-27.

95. Pudar, S.; Oxgaard, J.; Goddard, W. a., Mechanism of selective ammoxidation of propene to acrylonitrile on bismuth molybdates from quantum mechanical calculations. *Journal of Physical Chemistry C* **2010,** *114* (37), 15678-15694.

96. Carrasco, J.; Lopez, N.; Illas, F., First Principles Analysis of the Stability and Diffusion of Oxygen Vacancies in Metal Oxides. *Physical Review Letters* **2004,** *93* (22), 225502-225502.

97. Putnis, A., *Introduction to Mineral Sciences*. Cambridge University Press: 1992.

98. Catlow, C. R. A., *Defect Clustering in Nonstoichiometric Oxides*. Academic Press: 1981.

99. Ressler, T.; Wienold, J.; Jentoft, R. E.; Neisius, T., Bulk Structural Investigation of the Reduction of $MoO_3$ with Propene and the Oxidation of $MoO_2$ with Oxygen. *Journal of Catalysis* **2002,** *210* (1), 67-83.

100. Stoneham, A. M.; Durham, P. J., The ordering of crystallographic shear planes: theory of regular arrays. *Journal of Physics and Chemistry of Solids* **1973,** *34*, 2127-2135.

101. Ingham, B.; Hendy, S. C.; Chong, S. V.; Tallon, J. L., Density-functional studies of tungsten trioxide, tungsten bronzes, and related systems. *Physical Review B - Condensed Matter and Materials Physics* **2005,** *72* (7), 3-6.

102. Center, N. R. Linear Defects-Dislocations. (accessed 01/08/**2016**). < https://www.nde-ed.org/ EducationResources/ CommunityCollege/ Materials/Structure/ linear_defects.htm>.

103. Hart, E. W., On the role of dislocations in bulk diffusion. *Acta Metallurgica* **1957,** *5* (10), 597.

104. Love, G. R., Dislocation pipe diffusion. *Acta Metallurgica* **1964,** *12* (6), 731-737.

105. Hoffman, R. E.; Turnbull, D., Lattice and Grain Boundary Self Diffusion in Silver. *Journal of Applied Physics* **1951,** *22* (5), 634-639.

106. Shewmon, P.; Love, G. R., Self Diffusivity of Silver in Twist Boundaries. *Acta Metallurgica* **1963,** *11* (8), 899-906.

107. Ohring, M., *Materials science of thin films*. Academic Press: 1992.

108. Atkinson, A., Grain Boundary Diffusion: A historical perspective. *Journal of the Chemical Society, Faraday Transactions* **1990,** *86*, 1307-1310.

109. Peterson, N. L., Diffusion mechanisms and structural effects in grain boundaries. *Journal of Vacuum Science & Technology A: Vacuum, Surfaces, and Films* **1986,** *4* (6), 3066-3070.

110. Slifkin, L.; Lazarus, D.; Tomizuka, T., Self-Diffusion in Pure Polycrystalline Silver. *Journal of Applied Physics* **1952,** *23* (9), 1032-1034.

111. Oishi, Y.; Kingery, W. D., Self-diffusion of oxygen in single crystal and polycrystalline aluminum oxide. *The Journal of Chemical Physics* **1960,** *10* (2), 480-486.

112. Gallardo, I. J. Tungsten oxide nanocrystalline powders for gas sensing applications Universitat de Barcelona, Spain, 2003.

113. Salje, E., The Orthorhombic Phase of $WO_3$. *Acta Crystallographica B* **1977,** *33* (1), 574-577.

114. Moulzolf, S. C.; LeGore, L. J.; Lad, R. J., Heteroepitaxial growth of tungsten oxide films on sapphire for chemical gas sensors. *Thin Solid Films* **2001,** *400* (1-2), 56-63.

115. Nanba, T.; Yasui, I., X-ray diffraction study of microstructure of amorphous tungsten trioxide films prepared by electron beam vacuum evaporation. *Journal of Solid State Chemistry* **1989,** *83* (2), 305-315.

116. Kuzmin, A.; Purans, J.; Cazzanelli, E.; Vinegoni, C.; Mariotto, G., X-ray diffraction, extended x-ray absorption fine structures and Raman spectroscopy studies of $WO_3$ powders and (1-x) $WO_{3-y}$· $xReO_2$ mixtures. *Journal of Applied Physics* **1998,** *84*, 5515-5524.

117. Fierro, J. L. G., *Metal Oxide: Chemistry and Applications*. CRC Press: 2007.

118. Horsley, J. A.; Wachs, E.; Brown, J. M.; Via, G. H.; Hardcastlex, F. D., Structure of Surface Tungsten Oxide Species in the $WO_3/AI_2O_3$ Supported Oxide System from X-ray Absorption Near-Edge Spectroscopy and Raman Spectroscopy. *Journal of Physical Chemistry* **1987,** *91* (15), 4014-4020.

119. Altman, E. I.; Tanner, R. E., Using scanning tunneling microscopy to characterize adsorbates and reactive intermediates on transition metal oxide surfaces. *Catalysis Today* **2003,** *85* (2-4), 101-111.

120. Moulzolf, S. C.; Lad, R. J. In *Electronic Transport Mechanism in $WO_3$-Based Ultra-Thin Film Chemiresitive Sensor*, Transducers'01 Eurosensors XV, Germany, Germany, 2001.

121. Roy, R.; Guo, R.; Bhalla, A. S.; Cross, L. E., ‘‘Oriented film growth’’ not ‘‘epitaxy’’ in HTSC film growth *Journal of Vacuum Science and Technology A* **1994,** *12* (2), 269-273.

122. Ou, J. Z.; Yaacob, M. H.; Breedon, M.; Zheng, H. D.; Campbell, J. L.; Latham, K.; du Plessis, J.; Wlodarski, W.; Kalantar-Zadeh, K., In situ Raman spectroscopy of H2 interaction with $WO_3$ films. *Physical chemistry chemical physics : PCCP* **2011,** *13*, 7330-7339.

123. Steeves, M. M.; Deniz, D.; Lad, R. J., Charge transport in flat and nanorod structured ruthenium thin films. *Applied Physics Letters* **2010,** *96* (14), 142103-142103.

124. Vick, D.; Friedrich, L. J.; Dew, S. K.; Brett, M. J.; Robbie, K.; Seto, M.; Smy, T., Self-shadowing and surface diffusion effects in obliquely deposited thin films. *Thin Solid Films* **1999,** *339* (1), 88-94.

125. Robbie, K.; Sit, J. C.; Brett, M. J., Advanced techniques for glancing angle deposition. *Journal of Vacuum Science and Technology B* **1998,** *16* (3), 1115-1122.

126. Horprathum, M.; Limwichean, K.; Wisitsoraat, A.; Eiamchai, P.; Aiempanakit, K.; Limnonthakul, P.; Nuntawong, N.; Pattantsetakul, V.; Tuantranont, A.; Chindaudom, P., $NO_2$-sensing properties of $WO_3$ nanorods prepared by glancing angle DC magnetron sputtering. *Sensors and Actuators, B: Chemical* **2013,** *176* (2), 685-691.

127. Auroux, A.; Gervasini, A., Microcalorimetric Study of the Acidity and Basicity of Metal Oxide Surfaces. *Journal of Physical Chemistry* **1990,** *94* (16), 6371-6379.

128. Mahdavi-Shakib, A.; Clark, J. R.; Amar, F. G.; Frederick, B. G. In *Surface Acidity of Tungsten Oxide Bronzes in the Hydrodeoxygenation Mechanism*, 40th Northeast Regional Meeting of the American Chemical Society, Ithaca College, Ithaca, NY, 2015, Ithaca College, Ithaca, NY, 2015, 2015.

129. Crank, J., *The mathematics of diffusion*. 2nd ed.; Oxford University Press: 1975.

130. Hashin, Z.; Shtrikman, S., A Variational Approach to Theory of Effective Magnetic Permeability of Multiphase Materials. *Journal of Applied Physics* **1962,** *33* (10), 3125.

131. Kirkpatrick, S., Percolation and Conduction. *Reviews of Modern Physics* **1973,** *45* (4), 574.

132. Moghadam, M. M.; Rickman, J. M.; Harmer, M. P.; Chan, H. M., The role of boundary variability in polycrystalline grain-boundary diffusion. *Journal of Applied Physics* **2015,** *117* (4), 1-10.

133. Pietrzyk, D. J.; Frank, C. W., *Analytical Chemistry*. Academic Press: 1979.

134. Gas Chromatography. University of California Davis. Lecture Notes. (accessed 08/01/**2016**).
< http://www.chem.ucla.edu/~bacher/General/30BL/gc/theory.html>

135. Sputtering. Wake Forest University. Lecture Notes. (accessed 08/01/**2016**).
<http://users.wfu.edu/ucerkb/Nan242/L07-Sputtering_a.pdf>
<http://users.wfu.edu/ucerkb/Nan242/L08-Sputtering_b.pdf>

136. Lee, S. Modern Mass Spectroscopy. (accessed 08/01/**2016**).
< https://www.princeton.edu/chemistry/macmillan/group-meetings/SL-mass%20spect.pdf>

137. Mass Spectrometry Ionization Methods. Emory College of Arts and Science. (accessed 01/08/**2016**).
< http://chemistry.emory.edu/msc/tutorial/mass-spectrometry-ionization.html>

138. Mitchell, M. B., *Structure-Property Relations in Polymers*. American Chemical Society: 1993; Vol. 236.

139. Accardo, G.; Cioffi, R.; Colangelo, F.; D'Angelo, R.; De Stefano, L.; Paglietti, F., Diffuse Reflectance Infrared Fourier Transform Spectroscopy for the Determination of Asbestos Species in Bulk Building Materials. *Materials* **2014,** *7*, 457-470.

140. Pike Technologies. Diffuse Reflectance –Theory and Applications. Application Note. (accessed 01/08/**2016**).
< http://www.piketech.com/files/pdfs/DiffuseAN611.pdf>

141. Bragg's Law and Diffraction. Mineral Physics Institute. Stony brook (accessed 01/08/2016).
< http://www.eserc.stonybrook.edu/ProjectJava/Bragg/>

142. Scherrer, P., Bestimmung der Größe und der inneren Struktur von Kolloidteilchen mittels Röntgenstrahlen. *Nachrichten von der Gesellschaft der Wissenschaften zu Göttingen, Mathematisch-Physikalische Klasse* **1918,** *1918*, 98-100.

143. NIST Mass Spec Data Center, S., S.E., "Mass Spectra" in NIST Chemistry WebBook, NIST Standard Reference Database Number 69. NIST Standard Reference Database Number 69 ed.; National Institute of Standards and Technology, Gaithersburg MD: Gaithersburg MD, 2016.

144. LeGore, L. J.; Lad, R. J.; Vetelino, J. F.; Frederick, B. G.; Kenik, E. a., Aggregation and sticking probability of gold on tungsten trioxide films. *Sensors and Actuators, B: Chemical* **2001,** *76* (1-3), 373-379.

145. Ramis, G.; Yi, L.; Busca, G., Ammonia activation over catalysts for the selective catalytic reduction of $NO_x$, and the selective catalytic oxidation of $NH_3$ . An FT-IR study. *Catalysis Today* **1996,** *28*, 373-380.

146. Volpe, L. E. O.; Boudart, M., Compounds of Molybdenum and Tungsten With High Specific Surface-Area .1. Nitrides. *Journal of Solid State Chemistry* **1985,** *59* (3), 332-347.

147. Ghampson, I. T. Synthesis and Characterization of Catalysts for the Selective Transformation of Biomass-Derived Materials. Univerity of Maine, Maine, 2011.

148. Ruiz, P. E.; Frederick, B. G.; Wheeler, M. C.; Desisto, W. J. In *Activity and Selectivity over tungsten oxide catalysts*, Symposium on Alternate Energy and Fuel Chemistry, 38th Northeast Regional Meeting of the Americal Chemical Society, Rochester, NY, American Chemical Society: Rochester, NY, 2012.

149. Kanan, S. M.; Tripp, C. P., Synthesis, FTIR studies and sensor properties of $WO_3$ powders. *Current Opinion in Solid State and Materials Science* **2007,** *11* (1-2), 19-27.

150. Panayotov, D.; Ivanova, E.; Mihaylov, M.; Chakarova, K.; Spassov, T.; Hadjiivanov, K., Hydrogen spillover on $Rh/TiO_2$ : the FTIR study of donated electrons, co-adsorbed CO and H/D exchange. *Physical Chemistry Chemical Physics* **2015,** *17* (32), 20563-20573.

151. Moulzolf, S. C.; Ding, S. a.; Lad, R. J., Stoichiometry and microstructure effects on tungsten oxide chemiresistive films. *Sensors and Actuators, B: Chemical* **2001,** *77* (1-2), 375-382.

152. Loopstra, B. O.; Boldrini, P., Neutron Investigation of $WO_3$. *Acta Crystallographica* **1966,** *21*, 158-162.

153. Campbell, C. T., Finding the Rate-Determining Step in a Mechanism: Comparing DeDonder Relations with the "Degree of Rate Control". *Journal of Catalysis* **2001,** *204* (2), 520-524.

154. Fruhberger, B.; Stirling, N.; Grillo, F. G.; Ma, S.; Ruthven, D.; Lad, R. J.; Frederick, B. G., Detection and quantification of nitric oxide in human breath using a semiconducting oxide based chemiresistive microsensor. *Sensors and Actuators, B: Chemical* **2001,** *76* (1-3), 226-234.

## APPENDIX A

### Surface Barrier Potential

Using Poisson equation,

$$\frac{d^2E(x)}{dx^2} = -\frac{\rho(x)}{\varepsilon} \quad \text{A.1}$$

where $E(x)$ is the potential, $\rho(x)$ is the charge density in the space charge region and $\varepsilon$ is the dielectric constant of the metal oxide. The total charge density can be expressed as

$$\rho(x) = q\left(n_D - n(x)\right) \quad \text{A.2}$$

$n_D$ is the donor density, assumed to be uniform, due to fixed oxygen vacancies and $n(x)$ is the electron density in the space region. $n(x)$ can be expressed as

$$n(x) = n_b e^{\frac{qE(x)}{kT}} \quad \text{A.3}$$

where $n_b$is the charge density in the quasi neutral bulk. In the quasi neutral region

$$n_D = n_b \quad \text{A.4}$$

Using A.2, A.3 and A.4 in A.1 we obtain

$$\frac{d^2E(x)}{dx^2} = \frac{q}{\varepsilon}\left(n_b\left(e^{\frac{qE}{kT}} - 1\right)\right) \quad \text{A.5}$$

Without approximation, one cannot find a solution to this expression. On neglecting free carrier concentration in the space charge region, A.5 becomes

$$\frac{d^2E(x)}{dx^2} = -\frac{q\, n_D}{\varepsilon} \quad \text{A.6}$$

If $E_b$ is the potential in the metal oxide bulk, then using a parameter V, one can express

$$V(x) = E(x) - E_b \quad \text{A.7}$$

Using A.7 in A.6

$$\frac{dV}{dx} = -\int_x^{x_0} \frac{q\, n_D}{\varepsilon}\, dx \quad \text{A.8}$$

$x_0$ is the width of the depletion layer and at $x = x_0$, the space charge region contains a net charge of zero, therefore $\frac{dV}{dx} = 0$ at $x = x_0$. Thus A.8 becomes

$$\frac{dV}{dx} = \frac{q\, n_D}{\varepsilon}(x\text{-}x_0) \qquad \text{A.9}$$

Thus integrating A.9

The surface barrier potential can be expressed as

$$V = \frac{q\, n_D}{2\varepsilon}(x\text{-}x_0)^2 \qquad \text{A.10}$$

The surface barrier potential ($V_s$ at $x = 0$) can be expressed as

$$V_s = \frac{q\, n_D}{2\varepsilon} x_0^2 \qquad \text{A.11}$$

## APPENDIX B

## Temperature Dependence of Diffusion Coefficients for Single Crystal and Polycrystalline Oxides

Plot B1 shows that oxygen vacancy diffusion in $WO_3$, $V_2O_5$, and $MoO_3$ is many orders of magnitude faster than in pure $SnO_2$, ZnO, and $TiO_2$, but diffusivities in polycrystalline materials can be much higher than single crystals.

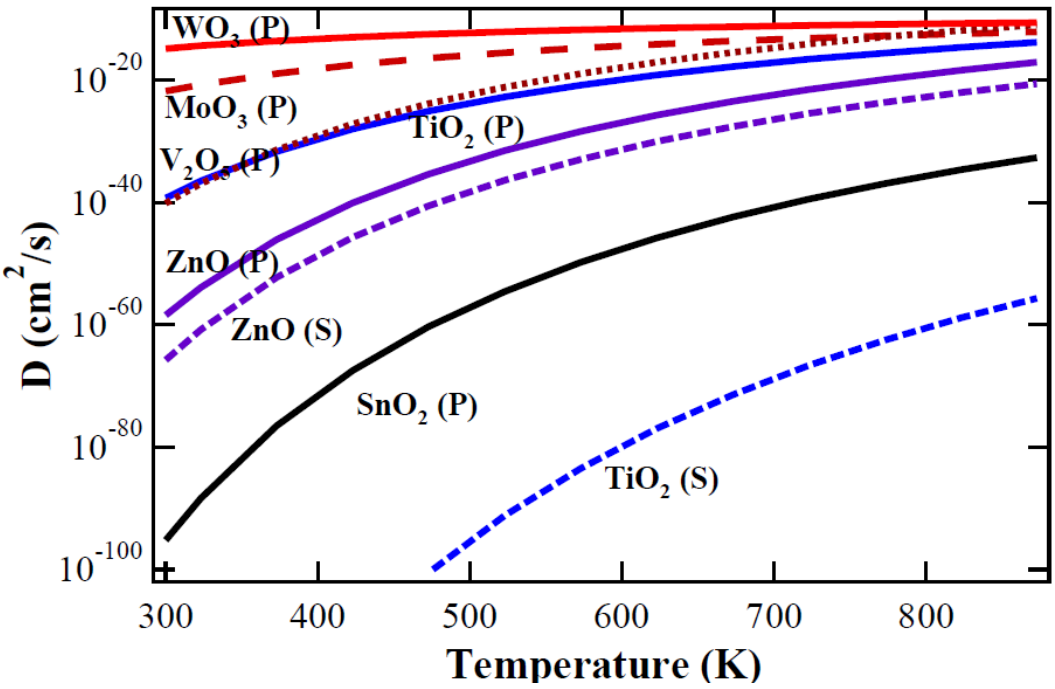


**Figure B1**. Temperature dependence of diffusion coefficients for single crystal (---S) and polycrystalline (—P) oxides. Plot shows that oxygen vacancy diffusion in $WO_3$, $V_2O_5$, and $MoO_3$ is many orders of magnitude faster than in pure $SnO_2$, ZnO, and $TiO_2$, but diffusivities in polycrystalline materials can be much higher than single crystals.

## APPENDIX C

## Dependence of Response Time, if Diffusion Limited, as a Function of Temperature for Planar Films of $WO_3$ to Other Oxides.

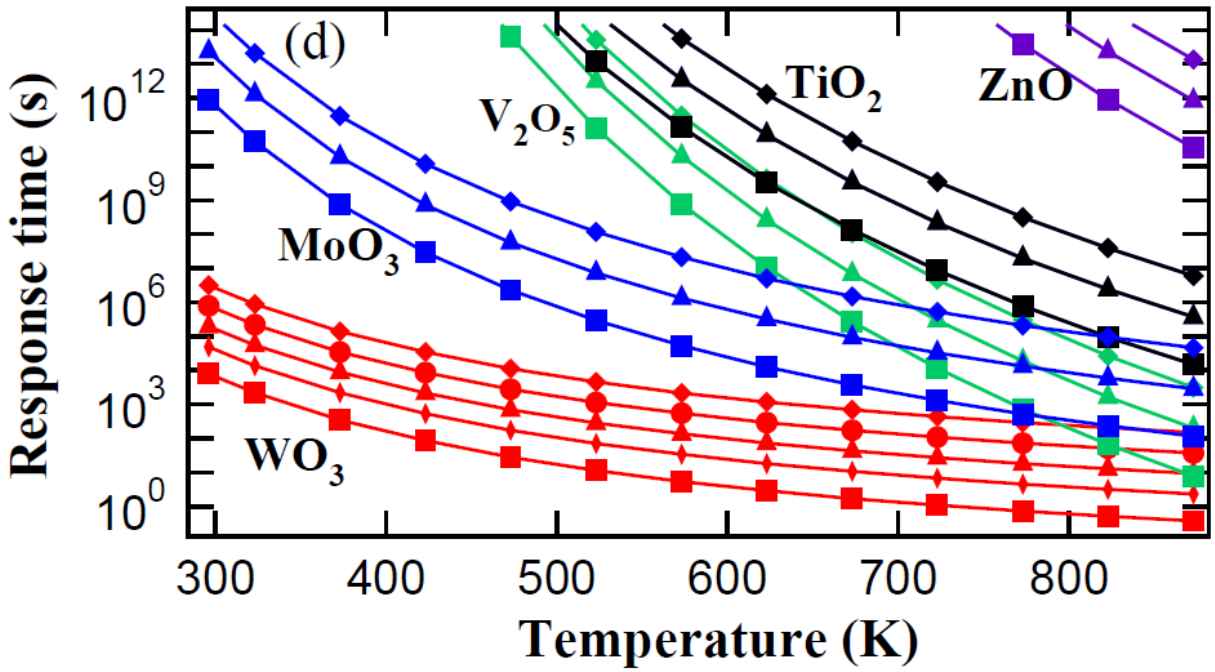


**Figure C1**. Comparison of the 90% response times for films of $WO_3$, $MoO_3$, $V_2O_5$, $TiO_2$ and ZnO, illustrating the strong temperature dependence. Curves of thickness, *L,* are marked as follows: (■) 50 nm, (♦) 125 nm, (▲) 250 nm, (●) 500 nm and (◆) 1000 nm.

## APPENDIX D

### Gold Loading Calculations

Calculations showing the mass of $HAuCl_4.3H_2O$ salt used to get 0.1% w/w Au-loading is given below,

Molecular weight of gold (Au) = $196.96 \frac{g}{mol}$, C.1

Molecular weight of $HAuCl_4.3H_2O$ = $393.83 \frac{g}{mol}$, C.2

Total ratio of salt required = $\left(\frac{\%\ \text{of metal}}{\text{mass of support}}\right) \times \left(\frac{1}{\text{molecular weight of metal}}\right) \times$

$(\text{molecular weight of salt}) \times \left(\frac{1}{\%\ \text{purity of salt}}\right)$, C.3

Therefore for 1.0 g of support ($WO_3$), total salt ratio required =

$$\left(\frac{0.001}{1.0}\right) \times \left(\frac{1}{196.96}\right) \times 393.83 \times \left(\frac{1}{100\%}\right) = \frac{0.002\ \text{g of salt}}{1.0\ \text{g of support}} = 0.2\%\ .$$ C.4

Thus for 10 g of $WO_3$, the mass of $HAuCl_4.3H_2O$ salt required is 0.02 g

## BIOGRAPHY OF THE AUTHOR

Aravind Reghu was born in Trivandrum, Kerala, India on December 14th, 1981. He graduated from Loyola school in 2000. He attended University of Calicut and graduated in 2004 with a Bachelor's degree in Electronics and Communications Engineering. From 2005-2007, he attended University of Maine and graduated with a Master's degree in Electrical Engineering.

He is a candidate for the Doctor of Philosophy degree Intersciplinary in Sensor Science and Engineering from the University of Maine in May, 2018.